EUROPEAN ORGANIZATION FOR NUCLEAR RESEARCH (CERN)

Comprehensive analysis of local and nonlocal amplitudes in the $B^0 \to K^{*0}\mu^+\mu^-$ decay

LHCb collaboration[†]

Abstract

A comprehensive study of the local and nonlocal amplitudes contributing to the decay $B^0 \to K^{*0}(\to K^+\pi^-)\mu^+\mu^-$ is performed by analysing the phase-space distribution of the decay products. The analysis is based on pp collision data corresponding to an integrated luminosity of $8.4\,\text{fb}^{-1}$ collected by the LHCb experiment. This measurement employs for the first time a model of both one-particle and two-particle nonlocal amplitudes, and utilises the complete dimuon mass spectrum without any veto regions around the narrow charmonium resonances. In this way it is possible to explicitly isolate the local and nonlocal contributions and capture the interference between them. The results show that interference with nonlocal contributions, although larger than predicted, only has a minor impact on the Wilson Coefficients determined from the fit to the data. For the local contributions, the Wilson Coefficient $\mathcal{C}_9$, responsible for vector dimuon currents, exhibits a 2.1σ deviation from the Standard Model expectation. The Wilson Coefficients $\mathcal{C}_{10}$, $\mathcal{C}'_9$ and $\mathcal{C}'_{10}$ are all in better agreement than $\mathcal{C}_9$ with the Standard Model and the global significance is at the level of 1.5σ. The model used also accounts for nonlocal contributions from $B^0 \to K^{*0}[\tau^+\tau^- \to \mu^+\mu^-]$ rescattering, resulting in the first direct measurement of the $bs\tau\tau$ vector effective-coupling $\mathcal{C}_{9\tau}$.

Submitted to JHEP

[†]Authors are listed at the end of this paper.

1 Introduction

The decay $B^0 \to K^{*0}\mu^+\mu^-$ has attracted significant attention in recent years, both theoretically and experimentally.[1] From the theoretical side, the combination of the loop suppressed flavour-changing neutral current $b \to s\ell^+\ell^-$ Standard Model (SM) amplitudes and the rich information arising from the multitude of K^{*0} polarisation amplitudes makes the decay an ideal channel to search for New Physics (NP) contributions [1]. From the experimental side, the $B^0 \to K^{*0}\mu^+\mu^-$ mode stands out as the corresponding $B^0 \to K^{*0}e^+e^-$ mode is harder to reconstruct at a hadron collider and the $B^0 \to K^{*0}\tau^+\tau^-$ mode is so difficult to reconstruct at any experiment that it has not been observed yet. Previous LHCb results of angular analyses of the $B^0 \to K^{*0}\mu^+\mu^-$ decay have consistently deviated from SM predictions at the level of three standard deviations (3σ) [2–6]. The decay has also been studied by ATLAS [7], BaBar [8,9], Belle [10,11], CDF [12], and CMS [13,14].

The matrix element for the $B^0 \to K^{*0}\mu^+\mu^-$ decay has components related to both local and nonlocal contributions. The local contributions correspond to an energy scale well above the beauty hadron masses and are where NP might manifest itself. The leading nonlocal contributions are due to narrow charmonium resonances in the dimuon mass spectrum of the $B^0 \to K^{*0}\mu^+\mu^-$ decay but influence all parts of the phase space. The subleading contributions come from two-particle amplitudes at dimuon masses above the open charm threshold. By explicitly excluding the charmonium resonance regions, previous analyses relied on theoretical estimates of the remaining nonlocal contributions. A novel feature of the analysis presented in this paper is to include the full phase space, including the narrow charmonium resonances, and determine the local and nonlocal contributions simultaneously. In this way the theoretical model dependence related to the nonlocal contributions is reduced as they are determined directly from the data.

Theoretically, the decay $B^0 \to K^{*0}\mu^+\mu^-$ is described in the Weak Effective Theory (WET) framework (see *e.g.* Ref. [15]), which is encapsulated by the Hamiltonian

$$\mathcal{H}_{\text{WET}} = \frac{-4G_F}{\sqrt{2}}V_{ts}^*V_{tb}\sum_i \mathcal{C}_i^{(')}(\mu)\mathcal{O}_i^{(')}(\mu), \tag{1}$$

where G_F is the Fermi constant and $V_{q_k q_j}$ are elements of the Cabibbo-Kobayashi-Maskawa (CKM) matrix corresponding to the $q_j \to q_k$ quark transition. The effective operators $\mathcal{O}_i^{(')}$ describe all possible interactions between ingoing and outgoing particles, while the Wilson Coefficients $\mathcal{C}_i^{(')}$ are the corresponding effective coupling constants. Lastly, μ defines the energy scale.

In the WET framework, the $\mathcal{O}_i^{(')}$ operators arise from integrating out all heavy particles at and above the electroweak mass scale $M_W \sim 80\,\text{GeV}/c^2$, and the Wilson Coefficients are calculated by matching results for physical observables calculated in the full and effective theories. The values of the Wilson Coefficients can then via renormalisation be evolved to the relevant energy scale for b-hadron decays, given by the mass of the b quark m_b [16]. The dominant effective local operators for $b \to s\ell^+\ell^-$ decays are defined using

---

[1]The inclusion of charge-conjugate processes is implied throughout, unless otherwise specified.

the standard notation as

$$\mathcal{O}_7 = \frac{e}{16\pi^2} m_b \left(\bar{s}_L \sigma^{\mu\nu} b_R\right) F_{\mu\nu}, \qquad \mathcal{O}'_7 = \frac{e}{16\pi^2} m_b \left(\bar{s}_R \sigma^{\mu\nu} b_L\right) F_{\mu\nu},$$

$$\mathcal{O}_{9\ell} = \frac{e^2}{16\pi^2} \left(\bar{s}_L \gamma_\mu b_L\right) \bar{\ell} \gamma^\mu \ell, \qquad \mathcal{O}'_{9\ell} = \frac{e^2}{16\pi^2} \left(\bar{s}_R \gamma_\mu b_R\right) \bar{\ell} \gamma^\mu \ell, \qquad (2)$$

$$\mathcal{O}_{10\ell} = \frac{e^2}{16\pi^2} \left(\bar{s}_L \gamma_\mu b_L\right) \bar{\ell} \gamma^\mu \gamma_5 \ell, \qquad \mathcal{O}'_{10\ell} = \frac{e^2}{16\pi^2} \left(\bar{s}_R \gamma_\mu b_R\right) \bar{\ell} \gamma^\mu \gamma_5 \ell,$$

and in this analysis, the SM values for the Wilson Coefficients are obtained from Ref. [16, 17]. The operators $\mathcal{O}_{1-6,8}$ mix through renormalisation with operators $\mathcal{O}_{7,9}$ resulting in observables sensitive to effective operators $\mathcal{O}_{7,9}^{\mathrm{eff}}$. Further discussion on these effective operators and their corresponding Wilson Coefficients can be found in Sec. 2.5. The Wilson Coefficients for the primed operators, which correspond to the opposite chirality processes, are predicted to be highly suppressed in the SM or to be zero, but are considered here as potential sources of NP.

The dilepton operators and the corresponding Wilson Coefficients carry a lepton flavour index (e.g. $\mathcal{C}_{9\ell}$) implying that NP might not be lepton flavour universal. Wilson Coefficients related to muons are implied in this paper if no explicit lepton index is given. Possible NP contributions from (pseudo)scalar or tensor operators are not taken into account in this analysis since they are strongly constrained through measurements of other $b \to s\ell^+\ell^-$ processes [15, 18]. The level of CP violation in the $B^0 \to K^{*0}\mu^+\mu^-$ decay is insignificant in the SM and, in this analysis, any NP contribution is assumed to be CP conserving. In this case all the Wilson Coefficients are real and unless otherwise noted, the short hand notation $\mathcal{C}_i$ will be used to denote the real part of the Wilson Coefficient.

Global analyses of the $B^0 \to K^{*0}\mu^+\mu^-$ decay and others involving $b \to s\ell^+\ell^-$ transitions indicate that the data are better described by models with one or more Wilson Coefficients differing from the SM predictions [19–24]. Interestingly, the introduction of a NP contribution to the single parameter $\mathcal{C}_9$, describing the effective $b \to s\ell^+\ell^-$ vector coupling, is sufficient to explain the tension observed with the data. Even better descriptions of the data can be achieved by modifying the axial-vector coupling $\mathcal{C}_{10}$ as well. Such contributions arise naturally in scenarios involving Z' bosons or leptoquarks, as discussed in e.g. Ref. [25].

Unfortunately, no robust conclusion regarding NP can be drawn at this point since both experimental measurements and theoretical predictions of decays involving the $b \to s\ell^+\ell^-$ transition remain limited in precision. For the $B^0 \to K^{*0}\mu^+\mu^-$ decay, the phase-space distribution depends on calculations of various nonperturbative hadronic matrix elements. The dominant contributions are proportional to matrix elements of the $b \to s$ quark current entering the local operators of Eq. 2. The corresponding local form factors are calculable with good precision in lattice QCD (LQCD) [26, 27] and light-cone sum rules (LCSR) [28, 29]. However, additional contributions arise from the four-quark operators $\mathcal{O}_{1,2}$, which produce a dimuon pair through a subsequent coupling to the electromagnetic current [30]. These contributions are dominated by the so-called charm-loop operator describing a $b \to sc\bar{c}(c\bar{c} \to \gamma^* \to \mu^+\mu^-)$ process. Such processes are at an energy scale below the cutoff in the WET framework and lead to so-called nonlocal form factors. These objects are less well understood and reliable methods for their calculation with controlled uncertainties are not yet well-developed. The size of the nonlocal contributions has been the source of some debate in recent years [22, 30–34] and no consensus has yet been reached regarding their influence.

The nonlocal contributions manifest as resonances in the $q^2 \equiv m^2_{\mu\mu}$ spectrum. The most strongly affected regions are those in the vicinity of the narrow quarkonia resonances, *i.e.* the $\phi(1020)$, J/ψ, and $\psi(2S)$. The method traditionally employed to avoid these nonlocal contributions is to omit regions in q^2 around the resonances from the experimental analyses. However, the nonlocal contributions can have significant effects far away from the resonances through interference, both between the various nonlocal components and with the local component [30]. Crucially, such effects lead to a shift in $\mathcal{C}_9$ that can potentially be large enough to resolve the observed tensions in the angular observables without requiring any NP affecting the local contributions [31, 32, 35].

Recently, an analysis was carried out that combined information from the low-q^2 ($1.1 \leq q^2 \leq 8.0 \, \text{GeV}^2/c^4$) and inter-resonance ($11.0 \leq q^2 \leq 12.5 \, \text{GeV}^2/c^4$) regions with the independently obtained measurements of the polarisation amplitudes and strong-phase differences at the J/ψ pole [6]. Based on the same dataset (2011–2012 and 2016) as prior LHCb analyses it obtained a result indicating that the nonlocal contributions did not affect prior measurements in a significant way.

In this paper, LHCb data are fitted with a model that combines the local and nonlocal amplitudes across the q^2 spectrum in the range $0.1 \leq q^2 \leq 18.0 \, \text{GeV}^2/c^4$. The model includes all known vector resonances coupling to muons, as well as two particle contributions from $D^{(*)}\overline{D}^{(*)}$ and $\tau^+\tau^-$ loops. It thereby simultaneously determines the nonlocal contributions and the Wilson Coefficients, $\mathcal{C}_9$, $\mathcal{C}_{10}$, $\mathcal{C}'_9$, $\mathcal{C}'_{10}$ and $\mathcal{C}_{9\tau}$ that describe the local contributions. The analysis is performed using proton-proton (pp) collision data corresponding to an integrated luminosity of $8.4 \, \text{fb}^{-1}$ collected during the years 2011–2012 (Run 1) and 2016–2018 (Run 2).

The paper is organised as follows: in Sec. 2, the decay amplitude model is described, followed by a description of the experimental considerations in Sec. 3. The strategy for performing the measurement is detailed in Sec. 4 and the main contributions to systematic uncertainties are described in Sec. 5. The results of the fit to data are then presented in Sec. 6, which is followed by a discussion and concluding remarks in Secs. 7 and 8, respectively.

2 Theoretical signal model

2.1 Angular definitions

In a four-body final state, the $B^0 \to K^+\pi^-\mu^+\mu^-$ differential decay rate can be fully described by a five-dimensional phase space. It is parameterised in terms of three helicity angles $\cos\theta_\ell$, $\cos\theta_K$ and ϕ, along with q^2 and $m^2_{K\pi}$, which denote the mass squared of the dimuon and $K^+\pi^-$ systems, respectively. The angle θ_ℓ is defined as the angle between the direction of the μ^+ (μ^-) in the dimuon rest frame and the direction of the dimuon in the B^0 ($\overline{B}^0$) rest frame. The angle θ_K is defined as the angle between the direction of the kaon in the K^{*0} ($\overline{K}^{*0}$) rest frame and the direction of the K^{*0} ($\overline{K}^{*0}$) in the B^0 ($\overline{B}^0$) rest frame. The angle ϕ is the angle between the plane containing the dimuon pair and the plane containing the kaon and pion from the K^{*0} meson. The angular basis used in this paper is identical to that defined in Ref. [2], and is defined such that the B^0 and $\overline{B}^0$ angular distributions are described by the same set of angular functions.

Within the range $0.796 < m_{K\pi} < 0.996 \, \text{GeV}/c^2$ considered in this analysis, the decay

$B^0 \to K^+\pi^-\mu^+\mu^-$ receives amplitude contributions from P-wave $K^{*0}(892)$ transitions, henceforth referred to simply as $B^0 \to K^{*0}\mu^+\mu^-$, and S-wave $B^0 \to K_0^{*0}(700)\mu^+\mu^-$ transitions. Contributions from higher partial wave $K^+\pi^-$ states in this mass range are considered to be negligible.

2.2 Decay rate and angular observables

The five-dimensional differential decay rate of the $B^0 \to K^+\pi^-\mu^+\mu^-$ process is expressed in terms of spherical harmonic angular coefficients $f_i(\cos\theta_\ell, \cos\theta_K, \phi)$ multiplied by the corresponding set of q^2-dependent functions $\overset{(-)}{J_i}(q^2)$ and $m_{K\pi}^2$-dependent functions $g_i(m_{K\pi}^2)$. This is written compactly as

$$\frac{\mathrm{d}^5 \overset{(-)}{\Gamma}(B^0 \to K^+\pi^-\mu^+\mu^-)}{\mathrm{d}q^2\, \mathrm{d}\vec{\Omega}\, \mathrm{d}m_{K\pi}^2} = \frac{9}{32\pi} \sum_i \overset{(-)}{J_i}(q^2) f_i(\cos\theta_\ell, \cos\theta_K, \phi) g_i(m_{K\pi}^2), \tag{3}$$

where Γ and $\overline{\Gamma}$ indicate the $\overline{B}^0 \to \overline{K}^{*0}\mu^+\mu^-$ and $B^0 \to K^{*0}\mu^+\mu^-$ decay rates, respectively, and likewise for the J_i and $\bar{J}_i$ functions. The $\overset{(-)}{J_i}(q^2)$ functions are built up from bilinear combinations of the transversity amplitudes, described in Sec. 2.3. Their explicit forms are given in Appendix A, along with the definitions of $f_i(\cos\theta_\ell, \cos\theta_K, \phi)$. The functions $g_i(m_{K\pi}^2)$ in Eq. 3 represent bilinear products of the line shape models for the $K^+\pi^-$ system. The P-wave line shape is modelled using a relativistic Breit–Wigner function and the S-wave line shape is modelled using the LASS parameterisation, both given in Ref. [36]. The systematic uncertainty on the parameters reported in this paper due to the choice of the $K^+\pi^-$ line shape is found to be negligible. Note that the q^2 dependence of the $g_i(m_{K\pi}^2)$ factors is suppressed. This is a good approximation given the q^2 and $m_{K\pi}^2$ ranges in which the analysis is performed. For this analysis, the differential decay rate of Eq. 3 is integrated over the selected region in $m_{K\pi}^2$ leading to

$$\frac{\mathrm{d}^4 \overset{(-)}{\Gamma}(B^0 \to K^+\pi^-\mu^+\mu^-)}{\mathrm{d}q^2\, \mathrm{d}\vec{\Omega}} = \frac{9}{32\pi} \sum_i \overset{(-)}{J_i}(q^2) f_i(\cos\theta_\ell, \cos\theta_K, \phi) G_i, \tag{4}$$

where G_i are given by

$$G_i = \int_{m_{K\pi}^2=0.796^2 \text{ GeV}^2/c^4}^{m_{K\pi}^2=0.996^2 \text{ GeV}^2/c^4} g_i(m_{K\pi}^2)\mathrm{d}m_{K\pi}^2 \ . \tag{5}$$

4

2.3 Transversity amplitudes

Following the convention described in Ref. [15], the seven transversity amplitudes for a P-wave K^{*0} state are given by

$$\mathcal{A}_0^{L,R}(q^2) = N_0 \Bigg\{ \left[\left(\mathcal{C}_9^{(\text{eff}),0}(q^2) - \mathcal{C}_9' \right) \mp \left(\mathcal{C}_{10} - \mathcal{C}_{10}' \right) \right] A_{12}(q^2)$$
$$+ \frac{m_b}{m_B + m_{K^*}} \left(\mathcal{C}_7^{(\text{eff}),0} - \mathcal{C}_7' \right) T_{23}(q^2) \Bigg\}, \tag{6}$$

$$\mathcal{A}_\parallel^{L,R}(q^2) = N_\parallel \Bigg\{ \left[\left(\mathcal{C}_9^{(\text{eff}),\parallel}(q^2) - \mathcal{C}_9' \right) \mp \left(\mathcal{C}_{10} - \mathcal{C}_{10}' \right) \right] \frac{A_1(q^2)}{m_B - m_{K^*}}$$
$$+ \frac{2m_b}{q^2} \left(\mathcal{C}_7^{(\text{eff}),\parallel} - \mathcal{C}_7' \right) T_2(q^2) \Bigg\}, \tag{7}$$

$$\mathcal{A}_\perp^{L,R}(q^2) = N_\perp \Bigg\{ \left[\left(\mathcal{C}_9^{(\text{eff}),\perp}(q^2) + \mathcal{C}_9' \right) \mp \left(\mathcal{C}_{10} + \mathcal{C}_{10}' \right) \right] \frac{V(q^2)}{m_B + m_{K^*}}$$
$$+ \frac{2m_b}{q^2} \left(\mathcal{C}_7^{(\text{eff}),\perp} - \mathcal{C}_7' \right) T_1(q^2) \Bigg\}, \tag{8}$$

$$\mathcal{A}_t(q^2) = N_t \left\{ 2 \left[\mathcal{C}_{10} - \mathcal{C}_{10}' \right] A_0(q^2) \right\}, \tag{9}$$

where the functions V, A_0, A_1, A_{12}, T_1, T_2, and T_{23} are the local hadronic form factors, while the nonlocal matrix elements are absorbed in the q^2 and polarisation-dependent effective Wilson Coefficients $\mathcal{C}_9^{(\text{eff}),\lambda}(q^2)$. For the $\mp$ symbol, the minus and plus signs correspond to the L and R superscripts, respectively. Further discussion of the effective Wilson coefficients is provided in Sec. 2.5. The symbols m_B and m_{K^*} denote the known masses of the B^0 and K^{*0} mesons [37]. Equations 6–9 are referred to as the longitudinal, parallel, perpendicular, and timelike transversity amplitudes, respectively.

The S-wave K_0^{*0} state leads to two additional transversity amplitudes, given by [38]

$$\mathcal{A}_{00}^{L,R}(q^2) = N_{00} \left((\mathcal{C}_9^{(\text{eff}),00} \mp \mathcal{C}_{10}) F_1(q^2) + \frac{2m_b}{m_B + m_{K_0^{*0}(700)}} \mathcal{C}_7^{(\text{eff}),00} F_T(q^2) \right), \tag{10}$$

where F_i are the corresponding local S-wave form factors as defined in Ref. [39]. The symbol $m_{K_0^{*0}}(700)$ denotes the mass of the K_0^{*0} state [37]. The choice of the $K_0^{*0}(700)$ mass leads to a systematic uncertainty discussed later in this paper. The timelike amplitude contribution for the S-wave K_0^{*0} is ignored in this analysis owing to the smallness of the S-wave contribution as a whole in the $m_{K\pi}^2$ range considered and the lepton-mass suppression of the timelike amplitudes. The various normalisation factors appearing in

the transversity amplitudes are given by

$$N_0 = \frac{-8Nm_Bm_{K^*}}{\sqrt{q^2}},$$

$$N_\| = -N\sqrt{2}(m_B^2 - m_{K^*}^2),$$

$$N_\perp = N\sqrt{2\lambda}, \tag{11}$$

$$N_t = \frac{N\sqrt{\lambda}}{\sqrt{q^2}},$$

$$N_{00} = -N\frac{\lambda_{K_0^{*0}}}{\sqrt{q^2}},$$

where the triangle (Källén) function λ is given by

$$\lambda = m_B^4 + m_{K^*}^4 + q^4 - 2(m_B^2 m_{K^*}^2 + m_{K^*}^2 q^2 + m_B^2 q^2), \tag{12}$$

and the constant N is

$$N = V_{tb}V_{ts}^* \sqrt{\frac{G_F^2 \alpha_{\text{em}}^2 q^2 \lambda^{1/2} \beta_\mu}{3 \times 2^{10} \pi^5 m_B^3}}, \tag{13}$$

with $\beta_\mu = \sqrt{1 - 4m_\mu^2/q^2}$. The K_0^{*0} subscript appearing in the expression of N_{00} in Eq. 11 indicates the $m_{K^*} \to m_{K_0^{*0}(700)}$ replacement. The angular coefficients of Eq. 4 can be fully constructed from combinations of the transversity amplitudes, as shown in Appendix A. Consequently, the parameters of the signal model for the fit to the $B^0 \to K^{*0}\mu^+\mu^-$ differential decay rate are those that feature in Eqs. 6–10. These include the Wilson Coefficients $\mathcal{C}_{7,9,10}^{(\prime)}$, and the parameters that describe the local and nonlocal hadronic contributions. The CKM elements, particle masses, and coupling constants are all taken to be known and are fixed in the fit. In the following subsections, specific parameterisations of the local and nonlocal amplitudes are presented, which allow both the hadronic parameters and the Wilson Coefficients to be determined from a fit to data.

2.4   Local form factors

The local $B^0 \to K^{*0}$ form factors $F_i \in \{V, A_0, A_1, A_{12}, T_1, T_2, T_{23}\}$ are parameterised using a series expansion [28],

$$F_i(q^2) = \frac{1}{1 - q^2/m_{R,i}^2} \sum_{k=0}^{2} \alpha_{i,k}[z(q^2) - z(0)]^k, \tag{14}$$

where the $\alpha_{i,k}$ coefficients are parameters to be determined, and $m_{R,i}$ is the mass of the lowest lying $\bar{b}s$ resonance with J^P quantum numbers matching those of the form factor F_i for $b \to s\ell^+\ell^-$ transitions. The values of $m_{R,i}$ used in this analysis are the same as those in Table 3 of Ref. [28]. The z function in Eq. 14 is defined as,

$$z(t) = \frac{\sqrt{t_+ - t} - \sqrt{t_+ - t_0}}{\sqrt{t_+ - t} + \sqrt{t_+ - t_0}}, \tag{15}$$

with $t_\pm = (m_B \pm m_{K^*})^2$ and $t_0 = t_+(1 - \sqrt{1 - t_-/t_+})$. This analysis uses the results from Ref. [34] that rely on a combination of LCSR [29] and LQCD [26, 27] computations to

constrain the coefficients $\alpha_{i,k}$. This constraint is propagated to the fit of the $B^0 \to K^{*0}\mu^+\mu^-$ differential decay rate through a multivariate Gaussian likelihood factor. The behaviour of the fit under alternative LCSR and LQCD local form-factor calculations presented in Ref. [28] is also investigated.

Recent LCSR computations of $B^0 \to K^{*0}$ form factors that account for the finite K^{*0} width have shown that narrow width $B^0 \to K^{*0}$ form factors can be scaled by a global factor of 1.1 to account for the finite K^{*0} width [34, 40]. This correction factor has only been demonstrated to work in the large recoil (low q^2) region and further theoretical work is required in order to establish a finite width effect to $B^0 \to K^{*0}$ form factors across the entire q^2 range. Therefore, the form-factor parameters used in this analysis, provided in Ref. [34], implicitly account for this factor in the region $q^2 < 8\,\mathrm{GeV}^2/c^4$ but not elsewhere.

2.4.1 S-wave local form factors

As no reliable S-wave local form-factor predictions exist as yet, in this analysis the S-wave amplitudes are treated as nuisance parameters. This means decoupling the local parameters appearing in $\mathcal{A}_{00}^{L,R}$ from those in the P-wave transversity amplitudes. Moreover, an estimation of the $B^0 \to K_0^{*0}$ contribution using data is employed by adopting an effective form factor in the S-wave amplitude given by

$$\mathcal{A}_{00}^{L,R} = -N\frac{\lambda_{K_0^{*0}}}{\sqrt{q^2}}\left[F_{\mathrm{eff}}(q^2)\left(\mathcal{C}_9^{(\mathrm{eff})S} \mp \mathcal{C}_{10}^S + \frac{2m_b}{m_B + m_{K_0^{*0}(700)}}C_7^S\right)\right], \qquad (16)$$

where the q^2-independent parameters $\mathcal{C}_9^{(\mathrm{eff})S}$, $\mathcal{C}_{10}^S$ and $\mathcal{C}_7^S$ are independent of the Wilson Coefficients $\mathcal{C}_9$, $\mathcal{C}_{10}$ and $\mathcal{C}_7$. The effective S-wave form factor F_{eff} is in turn given by

$$F_{\mathrm{eff}}(q^2) = \frac{F(0)}{1 + 2.15(\alpha_F - 1)\left(\frac{q^2}{m_B^2}\right) + 1.055(1 - 2\alpha_F + \beta_F)\left(\frac{q^2}{m_{B^0}^2}\right)^2}, \qquad (17)$$

with the parameters α_F and β_F both positive. This form-factor parameterisation describes a very similar shape in q^2 to that used in Ref. [39] but instead incorporates a polynomial with restricted parameters in the denominator. In this way, the fit can accommodate the wide range of $B^0 \to K_0^{*0}$ form factors in the literature while at the same time staying well behaved.

2.5 Nonlocal form factors

In Eqs. 6–10, the nonlocal form factors are absorbed into the Wilson Coefficients, which highlights the fact that the dominant effect of these contributions is a q^2- and helicity-dependent shift in the effective $\mathcal{C}_9$ value, given by

$$\mathcal{C}_9^{(\mathrm{eff}),\lambda} = \mathcal{C}_9 + Y_{q\bar{q},\lambda}(q^2), \qquad \text{with} \qquad Y_{q\bar{q},\lambda}(q^2) = \frac{\mathcal{G}_\lambda(q^2)}{\mathcal{F}_\lambda(q^2)}, \qquad (18)$$

where $\mathcal{G}_\lambda(q^2)$ are the nonlocal form factors and $\mathcal{F}_\lambda(q^2)$ are the corresponding local vector form factors. It should be noted that even if $\mathcal{C}_9$ is real, $\mathcal{C}_9^{(\mathrm{eff}),\lambda}$ will take on complex values.

The approach followed in this analysis begins with expressing the nonlocal term $Y_{q\bar{q},\lambda}(q^2)$ as a subtracted hadronic dispersion relation [41]

$$Y_{q\bar{q},\lambda}(q^2) = Y_{q\bar{q},\lambda}(q_0^2) + \frac{(q^2 - q_0^2)}{\pi} \int_{4m_\mu^2}^\infty \frac{\rho_{q\bar{q},\lambda}(s)}{(s - q_0^2)(s - q^2 - i\epsilon)} \mathrm{d}s, \tag{19}$$

where q_0^2 is the subtraction point discussed below and the spectral density function $\rho_{q\bar{q},\lambda}$ contains the complete information on hadronic real intermediate states that contribute to the $B^0 \to K^{*0}\mu^+\mu^-$ decay.

The expression for the nonlocal contributions given by Eq. 19 exploits the fact that $Y_{q\bar{q},\lambda}(q^2)$ is perturbatively calculable via an operator product expansion in the (unphysical) region of $q^2 \lesssim 0$ [30]. If one performs such a calculation, thereby fixing the subtraction term $Y_{q\bar{q},\lambda}(q_0^2)$, the second term in Eq. 19 then provides a means of extrapolating the result to physical q^2 values by integrating the spectral density function $\rho_{q\bar{q},\lambda}(s)$. The analytic structure of $Y_{q\bar{q},\lambda}(q^2)$, and therefore $\rho_{q\bar{q},\lambda}(s)$, is determined by the set of possible on-shell intermediate states [42]; therefore, as described in the next subsection, the spectral density function can be decomposed into a sum over contributions from known intermediate states in the $B^0 \to K^{*0}\mu^+\mu^-$ decay.

2.5.1   Parameterisation of specific nonlocal contributions

In this analysis, a parameterisation of the spectral density function $\rho_{q\bar{q},\lambda}(s)$ in Eq. 19 is adopted based on that of Ref. [43]. In particular, $\rho_{q\bar{q},\lambda}(s)$ is decomposed into a sum of parametric contributions from all relevant one-particle (1P) and two-particle (2P) intermediate states

$$\rho_{q\bar{q},\lambda}(q^2) = \rho_{q\bar{q},\lambda}^{1P}(q^2) + \rho_{q\bar{q},\lambda}^{2P}(q^2), \tag{20}$$

and correspondingly, the nonlocal terms are modified as

$$Y_{q\bar{q},\lambda}(q^2) = Y_{q\bar{q},\lambda}(q_0^2) + \Delta Y_{q\bar{q},\lambda}^{1P}(q^2) + \Delta Y_{q\bar{q},\lambda}^{2P}(q^2) + Y_{\tau\tau,\lambda}. \tag{21}$$

The vector resonances $j = \{\rho(770), \omega(782), \phi(1020), J/\psi, \psi(2S), \psi(3770), \psi(4040), \psi(4160)\}$ are considered for the 1P states, while for the 2P states the various open-charm meson pairs $k = \{D\bar{D}, D^*\bar{D}, D^*\bar{D}^*\}$ are considered. The spectral density function therefore formally becomes,

$$\rho_{q\bar{q},\lambda}^{1P}(q^2) \propto \sum_j \mathcal{M}_j^\lambda(B \to K^{*0}V_j)\delta(q^2 - m_j^2), \tag{22}$$

$$\rho_{q\bar{q},\lambda}^{2P}(q^2) \propto \sum_k \int \frac{\mathrm{d}p_k^2}{16\pi^2}\delta(q^2 - p_k^2) \int \frac{\mathrm{d}^3\vec{p}_{k_1}}{E_{k_1}} \frac{\mathrm{d}^3\vec{p}_{k_2}}{E_{k_2}} \mathcal{M}_k^\lambda(B \to K^{*0}M_{k_1}M_{k_2})\delta^4(p_k - p_{k_1} - p_{k_2}), \tag{23}$$

where the j index represents the different 1P states and k represents the 2P states.

In Eq. 22, the 1P states are treated as stable particles. In order to account for the one-particle resonance widths, the dispersive integral of $\rho_{q\bar{q},\lambda}^{1P}(q^2)$ is modelled using the expression

$$\Delta Y_{q\bar{q},\lambda}^{1P}(q^2) = \sum_j A_j^\lambda \frac{(q^2 - q_0^2)}{m_j^2 - q_0^2} BW_j(q^2) \equiv \sum_j |A_j^\lambda|e^{i\delta_j^\lambda} \frac{(q^2 - q_0^2)}{m_j^2 - q_0^2} BW_j(q^2), \tag{24}$$

8

with each

$$BW_j(q^2) = \frac{m_j\Gamma_j}{\left(m_j^2 - q^2\right) - i\,m_j\Gamma_j}, \tag{25}$$

describing a relativistic Breit–Wigner distribution. The pole masses m_j and natural widths Γ_j are set to their world-average values [37]. The widths are fixed in the fit for all resonances, while the pole masses are fixed for all except for the J/ψ and $\psi(2S)$ resonances. The $|A_j^\lambda|$ and δ_j^λ parameters, to be determined from data, are the relative magnitude and phase of each resonance. The phase convention used here defines the longitudinal phases, δ_j^0, relative to $\mathcal{C}_9$, while the phases for the other polarisation components $\delta_j^{\|}$ and $\delta_j^\perp$ are defined relative to the longitudinal component.

This analysis constitutes the first measurement of the phase differences between the local and nonlocal amplitudes in the $B^0 \to K^{*0}\mu^+\mu^-$ decay in the range $0.1 < q^2 < 18$ GeV$^2/c^4$. Existing measurements [44–46] of the relative phase differences between the helicity components of $B^0 \to J/\psi K^{*0}$ and $B^0 \to \psi(2S)K^{*0}$ provide a cross-check of the parameterisation. Previous measurements of the polarisation amplitudes for the decays $B^0 \to \rho^0 K^{*0}$ and $B^0 \to \omega K^{*0}$ from Ref. [47], and $B^0 \to \phi K^{*0}$ [48] are used in combination with the measured branching fractions [37] to fix the magnitudes and relative phases for these contributions such that only the overall phase relative to $\mathcal{C}_9$ is measured for each. A different phase convention is used in this analysis, which amounts to shifting the previously measured phases by $+\pi$.

The relativistic Breit–Wigner approximation is a good description of well-separated narrow states. For the broad overlapping resonances above the open-charm region and below the $\phi(1020)$ meson, the modelling of the one-particle amplitudes constitutes an approximation that has been shown to be valid given the relatively small amount of signal in the open-charm region of this rare decay [49].

The parameters $|A_j^\lambda|$ appearing in Eq. 24 are normalised according to the branching fraction of the processes $B^0 \to V_i K^{*0}$, where V_i denotes a $J^{PC} = 1^{--}$ one-particle state, such that

$$|A_j^\lambda|^2 = \frac{\hbar \mathcal{B}(B^0 \to V_i K^{*0})\mathcal{B}(V_i \to \mu^+\mu^-)(m_j^2 - q_0^2)f_j^\lambda}{\tau_B \int \left|\mathcal{N}^\lambda(q^2 - q_0^2)BW_j(q^2)F_{\text{vec}}^\lambda(q^2)\right|^2 \mathrm{d}q^2}, \tag{26}$$

where the $B^0 \to K^{*0}$ vector form factors are denoted as $F_{\text{vec}}^\lambda \in (V, A_1, A_{12})$, $\mathcal{N}_\lambda \in (N_0, N_\perp, N_\|)$ as defined in Sec 2.3 and f_j^λ denote the polarisation fractions of the particular final state.

Following the recipe of Ref. [43], the two-particle amplitudes $\mathcal{M}_k^\lambda(B \to K^{*0}M_{k_1}M_{k_2})$, appearing in Eq. 23, are described using the two-body phase-space function for a state with centre-of-mass energy $\sqrt{s} = \sqrt{q^2}$ decaying into the state $M_{k_1}M_{k_2}$, characterised by masses m_{k_1} and m_{k_2} with relative orbital angular momentum L set to the lowest partial wave allowed by angular momentum conservation. For the set of two-particle states $k = \{D\overline{D}, D^*\overline{D}, D^*\overline{D}^*\}$, the spectral density therefore has the form

$$\rho_{q\bar{q}}^{2P}(q^2) = \sum_k \left[\frac{\lambda(q^2, m_{k_1}^2, m_{k_2}^2)}{q^2}\right]^{\frac{2L+1}{2}}, \tag{27}$$

with $L = 0$ for $D^*\overline{D}$, and $L = 1$ for $D\overline{D}$ and $D^*\overline{D}^*$, resulting in two-particle terms given by

$$\Delta Y_{q\bar{q},\lambda}^{2\mathrm{P}}(q^2) = A_{D^*\bar{D}}^{\lambda} h_S(m_{D^*\bar{D}}, q^2) + \sum_{n=D\bar{D},D^*\bar{D}^*} A_n^{\lambda} h_P(m_n, q^2),$$

$$\equiv |A_{D^*\bar{D}}^{\lambda}| e^{i\delta_{D^*\bar{D}}^{\lambda}} h_S(m_{D^*\bar{D}}, q^2) + \sum_{n=D\bar{D},D^*\bar{D}^*} |A_n^{\lambda}| e^{i\delta_n^{\lambda}} h_P(m_n, q^2), \qquad (28)$$

where the functions h_S and h_P are defined in Ref. [43] and describe the amplitude as a function of q^2. The quantity $m_{j_1 j_2} = (m_{j_1} + m_{j_2})/2$ is an effective mass for the two-body state state, while $|A_{j_1 j_2}^{\lambda}|$ and $\delta_{j_1 j_2}^{\lambda}$ are its magnitude and phase. A Gaussian constraint is placed on the open-charm components relating the size of the real and imaginary parts for each polarisation of the three open-charm contributions. A systematic uncertainty is assigned for potential biases in the parameters due to this constraint, described in Sec. 5.4.

Lepton flavour universality violating $b \rightarrow s\tau^+\tau^-$ transitions, with subsequent $\tau^+\tau^- \rightarrow \gamma^* \rightarrow \mu^+\mu^-$ rescattering, introduces $\mathcal{C}_{9\tau}$ contributions to $B^0 \rightarrow K^{*0}\mu^+\mu^-$ decays via a nonlocal two-particle amplitude. Therefore, following Ref. [43],

$$Y_{\tau\bar{\tau}}(q^2) = -\frac{\alpha_{\mathrm{em}}}{2\pi}\mathcal{C}_{9\tau}\left[h_S(m_\tau, q^2) - \frac{1}{3}h_P(m_\tau, q^2)\right]. \qquad (29)$$

Finally, for the S-wave, the nonlocal amplitudes give rise to an effective $\mathcal{C}_9$ coefficient as in Eq. 18. The only considered S-wave nonlocal contributions are those arising from $B^0 \rightarrow J/\psi K_0^{*0}$ and $B^0 \rightarrow \psi(2S)K_0^{*0}$ amplitudes, contributing to the $\mathcal{C}_9^{(\mathrm{eff}),00}$ coefficient. The S-wave amplitude of other nonlocal contributions is expected to be subdominant compared to their already relatively suppressed P-wave counterpart and is ignored. With this parameterisation, there exists a complete degeneracy between the form factor normalisation parameter $F(0)$ and the $\mathcal{C}_9^S$ parameters. For this reason, the parameters $\mathcal{C}_{7,9}^S$ are kept fixed in the fit to data.

2.5.2 Subtraction constant

The dispersion relation shown in Eq. 19 requires knowledge of the subtraction constant $Y_{q\bar{q}}(q_0^2)$, which is in principle different for charmed and light-quark hadronic states. In this analysis, a subtraction point of $q_0^2 = -4.6\,\mathrm{GeV}^2/c^4$ is chosen for the subtraction constant $Y_{c\bar{c}}(q_0^2)$ whose value is taken from the two-loop calculation in an operator product expansion of the dominant nonlocal contributions presented in Ref. [50].

As the light-quark contributions are CKM suppressed, the same subtraction constant is used for both the charm- and light-quark hadronic dispersion relation by default. A systematic uncertainty for this approach is assessed by studying the behaviour of the fit under an unsubtracted dispersion relation for light-quarks and is found to make a negligible difference to the fit results.

2.5.3 Further empirical components

Global fits to $B^0 \rightarrow K^{*0}\gamma$, $B^0 \rightarrow K^{*0}e^+e^-$ and $B_s^0 \rightarrow \phi\gamma$ measurements have placed stringent constraints on NP contributions to the Wilson Coefficients $\mathcal{C}_7$ and $\mathcal{C}_7'$ [51,52]. As such, in this analysis, the $\mathcal{C}_7$ and $\mathcal{C}_7'$ values are fixed to their SM predictions [16]. Instead, a helicity-dependent shift to the $\mathcal{C}_7$ Wilson Coefficient is introduced, encoded

10

as $\mathcal{C}_7^{(\mathrm{eff}),\lambda} = \mathcal{C}_7 + \Delta\mathcal{C}_7^\lambda$, where $\Delta\mathcal{C}_7^\lambda$ are three complex parameters to be determined from data. Such a parameterisation allows for the presence of an additional helicity-dependent complex phase that is constant across q^2 [35].

In the amplitude fits, the parameters $\Delta\mathcal{C}_7^{\parallel,0}$ are degenerate with the tensor form-factor coefficients $\alpha_{T_2,0}$, $\alpha_{T_{23},0}$. Therefore, the choice is made to fix the parameters $\alpha_{T_2,0}$ and $\alpha_{T_{23},0}$ to their values provided in Ref. [34]. In order to assess the level of compatibility between the entire set of baseline and postfit form-factor coefficients, a separate fit is performed where the parameters $\mathcal{C}_7^{\parallel,0}$ are instead fixed and the coefficients $\alpha_{T_2,0}$, $\alpha_{T_{23},0}$ are allowed to vary in the fit.

3 Experimental model of the signal

In order to accurately describe the data, the theoretical $B^0 \to K^{*0}\mu^+\mu^-$ decay rate must be augmented with a model for the detector response. A description of the LHCb detector and simulation framework is provided in this section, along with an explanation of the event selection requirements. Using simulation, a model for the total efficiency of the event reconstruction and selection is developed, along with a model for the q^2 resolution of the detector. The final form and implementation of the signal model is described in Sec. 3.4.

3.1 Detector and simulation

The LHCb detector [53, 54] is a single-arm forward spectrometer covering the pseudorapidity range $2 < \eta < 5$, designed for the study of particles containing b or c quarks. The detector includes a high-precision tracking system consisting of a silicon-strip vertex detector surrounding the pp interaction region, a large-area silicon-strip detector located upstream of a dipole magnet with a bending power of about $4\,\mathrm{Tm}$, and three stations of silicon-strip detectors and straw drift tubes placed downstream of the magnet. The tracking system provides a measurement of the momentum, p, of charged particles with a relative uncertainty that varies from 0.5% at low momentum to 1.0% at $200\,\mathrm{GeV}/c$. The minimum distance of a track to a primary pp collision vertex (PV), the impact parameter (IP), is measured with a resolution of $(15 + 29/p_\mathrm{T})\,\mu\mathrm{m}$, where p_T is the component of the momentum transverse to the beam, in GeV/c. Different types of charged hadrons are distinguished using information from two ring-imaging Cherenkov detectors. Photons, electrons and hadrons are identified by a calorimeter system consisting of scintillating-pad and preshower detectors, an electromagnetic and a hadronic calorimeter. Muons are identified by a system composed of alternating layers of iron and multiwire proportional chambers. The information from each of the particle identification (PID) detectors is used as input to several multivariate classifiers, each trained to identify a certain species of particle.

The reconstruction and selection of events is performed by a trigger [55, 56], which consists of a hardware stage based on information from the calorimeter and muon systems, followed by a software stage, which applies a full event reconstruction. In the software stage, trigger signals are associated with reconstructed particles and can be queried offline.

Simulation is required to develop and model the effects of the selection requirements on the signal angular distribution and to assess the impact of certain sources of background

and potential systematic uncertainty. In the simulation, pp collisions are generated using PYTHIA [57] with a specific LHCb configuration [58]. Decays of unstable particles are described by EVTGEN [59], in which final-state radiation is generated using PHOTOS [60]. The interaction of the generated particles with the detector and its response are implemented using the GEANT4 toolkit [61] as described in Ref. [62]. In a subset of the simulated datasets, the underlying pp interaction is reused multiple times, with an independently generated signal decay for each [63]. In order to ensure agreement between the simulation and real LHCb data, independent samples are used to calibrate the simulation and correct for potential discrepancies.

3.2   Signal candidate selection

The $B^0 \to K^{*0}\mu^+\mu^-$ signal candidates are first required to pass the hardware trigger, which selects events containing at least one muon with high transverse momentum p_T. The minimum p_T threshold varies between $1.36\,\text{GeV}/c$ and $1.8\,\text{GeV}/c$ for single muons, depending on the year of data taking. For pairs of muons, a threshold is placed on the product of their p_T, which varies between $1.68\,\text{GeV}^2/c^2$ and $3.24\,\text{GeV}^2/c^2$, depending on the year of data taking. In the subsequent software trigger, at least one of the final-state particles is required to have $p_T > 1.7\,\text{GeV}/c$, unless the particle is identified as a muon in which case $p_T > 1.0\,\text{GeV}/c$ is required. The final-state particles that satisfy these transverse momentum criteria are also required to have an IP larger than $100\,\mu\text{m}$ with respect to all candidate PVs in the event to reject prompt particles produced directly in pp collisions. Finally, a dedicated trigger line is employed to select multibody B meson candidates based on the topology of the decay products. This trigger requires that the tracks of two or more of the final-state particles form a vertex that is significantly displaced from any PV. At all stages of the trigger, it is required that the particles composing the signal candidate are directly responsible for the trigger decision, as opposed to other particles in the event.

In the offline selection, signal candidates are formed from a pair of oppositely charged tracks that are identified as muons, combined with a K^{*0} meson candidate. The K^{*0} candidate is formed from two oppositely charged tracks that are identified as a kaon and a pion. The four tracks of the final-state particles are required to have a significant IP with respect to all PVs in the event and form a good-quality common vertex. The impact parameter of the B^0 candidate with respect to one of the PVs is required to be small and the decay vertex of the B^0 candidate is required to be significantly displaced from the same PV. The angle between the reconstructed B^0 momentum and the vector connecting the PV to the reconstructed B^0 decay vertex is required to be small. Candidates are required to have reconstructed B^0 mass, denoted as $m(K^+\pi^-\mu^+\mu^-)$, in the range $4800 < m(K^+\pi^-\mu^+\mu^-) < 6500\,\text{MeV}/c^2$. Finally, the reconstructed mass of the $K^+\pi^-$ system, denoted as $m(K^+\pi^-)$, is required to be in the range $796 < m(K^+\pi^-) < 996\,\text{MeV}/c^2$.

A significant background contribution arises from candidates formed by the random combination of kaons, pions, and muons originating from different parent particles or from the pp collision itself (referred to as combinatorial background). To reduce the level of combinatorial background, a Boosted Decision Tree (BDT) [64, 65] classifier is trained to discriminate between signal and background based on a set of input variables corresponding to reconstructed particle information. The BDT algorithm is trained entirely using data, with background subtracted $B^0 \to J/\psi(\to \mu^+\mu^-)K^{*0}$ events used as a

signal proxy, and $B^0 \to K^{*0}\mu^+\mu^-$ candidates with a mass above $5500\,\mathrm{MeV}/c^2$ used as a background proxy. For the background proxy, events with dimuon masses close to the $\phi(1020)$, J/ψ, and $\psi(2S)$ resonance masses are excluded to avoid biasing the training with many events that contain real resonant dimuons. The background subtraction is achieved using the *sPlot* technique [66] where the weights are obtained from a fit to the $m(K^+\pi^-\mu^+\mu^-)$ distribution. A total of thirteen training variables are used, and the ones found to provide the most discriminating power include various kinematic properties of the B meson, along with PID and isolation variables of the daughter particles. The requirement on the BDT output is chosen to optimise the signal significance $S/\sqrt{S+B}$, where S and B and the expected signal and background yields, respectively. The BDT classifier achieves a signal efficiency of approximately 87% and 90% in Run 1 and Run 2, respectively, whilst maintaining a consistent background rejection rate of greater than 98%.

3.3 Modelling of the detector efficiency and response

The reconstruction and selection of signal candidates sculpt the phase space of the signal decay. This effect can be accounted for in the fit to the data via an acceptance function $\epsilon(\cos\theta_\ell, \cos\theta_K, \phi, q^2)$, which includes the effects of the detector geometry, triggering, reconstruction, and selection of events.

The acceptance function is determined in the four-dimensional phase space described by $\cos\theta_\ell$, $\cos\theta_K$, ϕ, and q^2, using simulation generated with a uniform distribution in each dimension. The simulated events are run through the complete reconstruction and selection chain, and the resulting deviation from uniformity is taken to quantify the acceptance. The acceptance function is modelled using Legendre polynomials, *i.e.*

$$\epsilon(\cos\theta_\ell, \cos\theta_K, \phi, q^2) = \sum_{ijkl} c_{ijkl} P_i(\cos\theta_K) P_j(\cos\theta_\ell) P_k(\phi) P_l(q^2), \tag{30}$$

where P_m refers to the Legendre polynomial of order m. The maximum polynomial order for each dimension is chosen empirically to give the set of lowest orders which are sufficient to model the acceptance well, leading to the choice of a ninth order polynomial for the q^2 dimension, seventh order for the $\cos\theta_K$ dimension, fourth order for the $\cos\theta_\ell$ dimension, and sixth order for the ϕ dimension. The resulting acceptances are shown in Fig. 1 and a systematic uncertainty is assigned to choice of Legendre polynomial orders as described in Sec. 5.3.

In addition to the acceptance, a resolution model, given by $R(q^2 - q^2_{\mathrm{true}})$, is implemented to account for the smearing of reconstructed dimuon masses relative to their true values. This effect is the combined result of the finite resolution in each subdetector involved in the reconstruction of muons. The q^2 resolution model is built up from the sum of a Gaussian function $G(\Delta q^2; \mu, \sigma)$, and two Crystal Ball (CB) functions [67] $C_{l,u}(\Delta q^2; \mu, \sigma, \alpha_{l,u}, n_{l,u})$, with power law tails on opposite sides,

$$\begin{aligned} R(\Delta q^2) = {} & f_G G(\Delta q^2; \mu, \sigma_G) \\ & + (1 - f_G) \frac{1}{N_C} \left[C_u(\Delta q^2; \mu, \sigma_C, \alpha_u, n_u) + C_l(\Delta q^2; \mu, \sigma_C, \alpha_l, n_l) \right], \end{aligned} \tag{31}$$

where $\Delta q^2 \equiv q^2 - q^2_{\mathrm{true}}$, f_G is the Gaussian fraction, and N_C is a normalisation factor for the CB sum component. The optimal parameters of the resolution model are determined
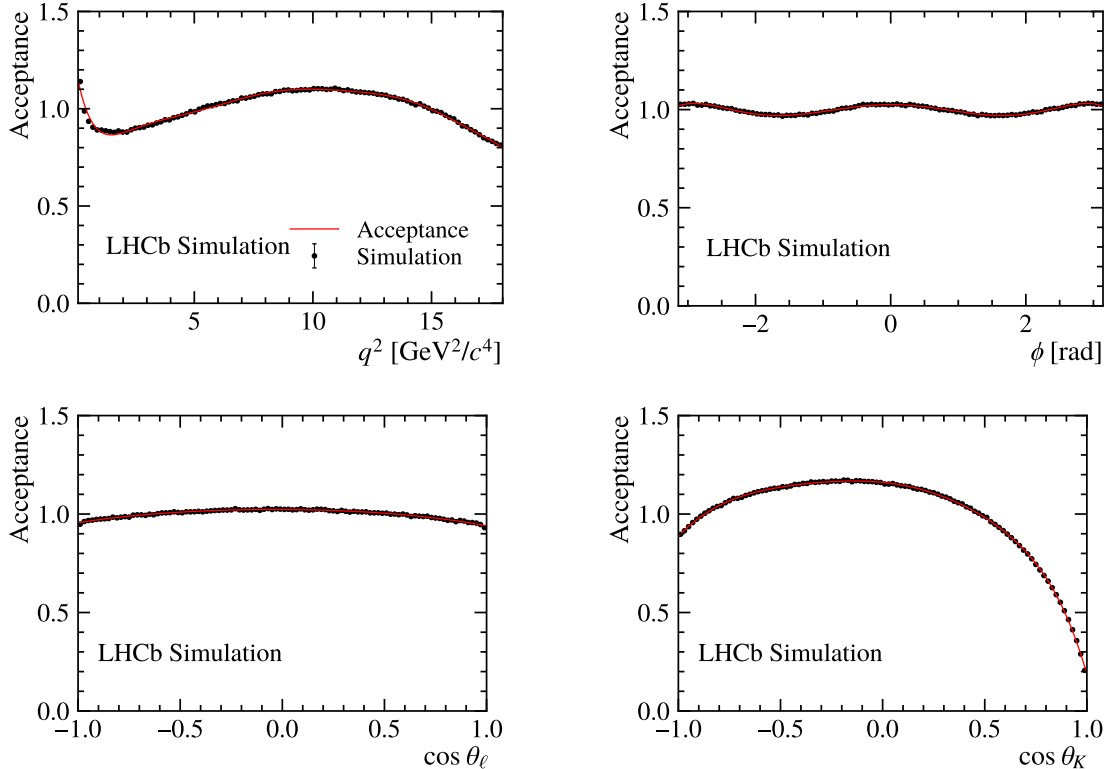
Figure 1: One-dimensional projections of the acceptance function determined from simulation.

Table 1: Three q^2 regions defining the simultaneous fit categories when determining the Wilson Coefficients.

Category	Region
Low-q^2	$0.10 \leq q^2 < 3.24 \, \text{GeV}^2/c^4$
Mid-q^2	$3.24 \leq q^2 < 11.56 \, \text{GeV}^2/c^4$
High-q^2	$11.56 \leq q^2 \leq 18.00 \, \text{GeV}^2/c^4$

using either simulation or data, depending on the q^2 region. The resolution varies depending on the value of q^2 itself in a nonlinear fashion, and ranges from approximately $0.01 \, \text{GeV}^2/c^4$ at $q^2 = 1 \, \text{GeV}^2/c^4$ to $0.04 \, \text{GeV}^2/c^4$ at $q^2 = 13.6 \, \text{GeV}^2/c^4$. The final fit to data is performed simultaneously in three q^2 regions, allowing variations in the resolution model and background composition to be accurately modelled. These three regions, referred to as low-, mid-, and high-q^2, are chosen to have the three narrow $q\bar{q}$ resonances, the $\phi(1020)$, J/ψ, and $\psi(2S)$ in separate regions and are defined according to Table 1.

In the low-q^2 region, the resolution parameters are obtained through an unbinned maximum likelihood fit to the distribution of q^2 reconstruction errors in simulated $B^0 \to K^{*0}\mu^+\mu^-$ decays. The $\alpha_{l,u}$ parameters of the CB tails are symmetrised in the low-q^2 region to improve stability, while the remaining parameters of the resolution model are allowed to vary freely in this fit. The model provides an excellent description of the resolution in simulation, and the results of this fit are shown in Fig. 2a. The low-q^2

14

(a)

(b)

(c)
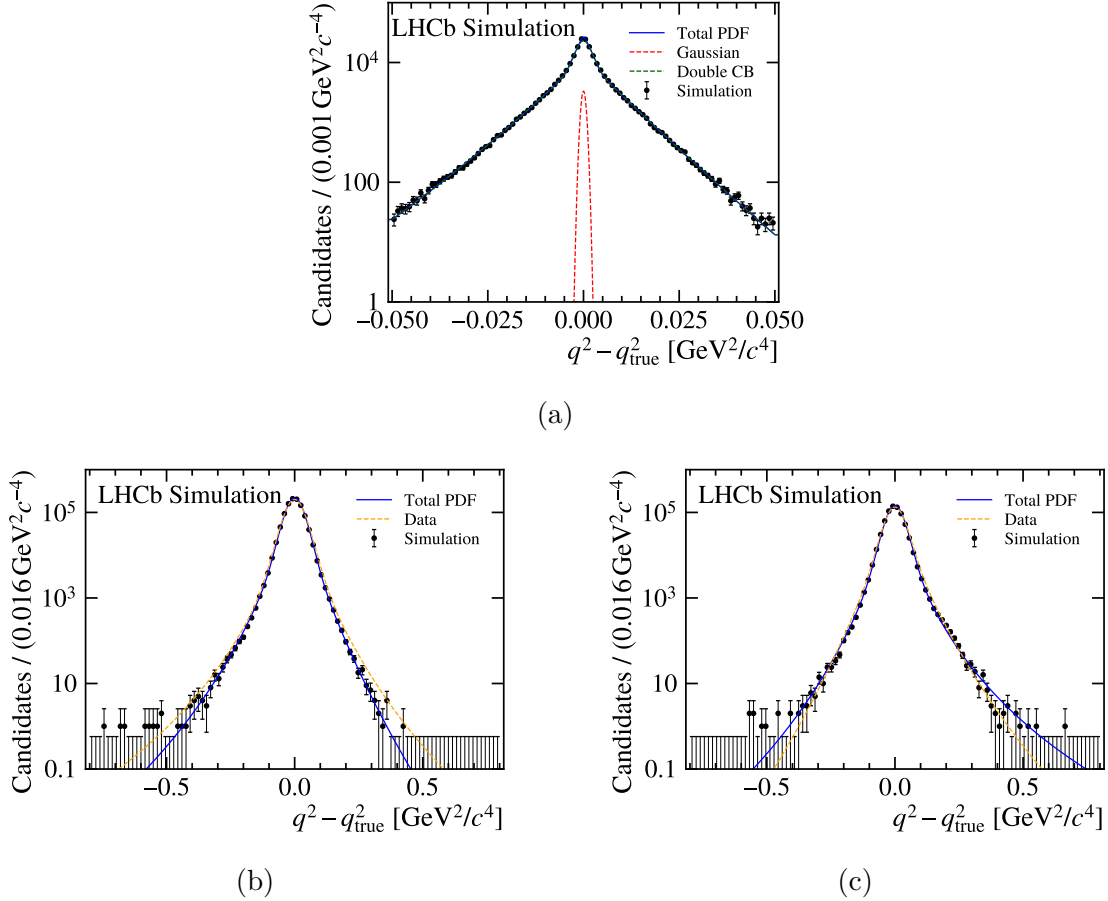
Figure 2: Distributions of reconstructed q^2 resolution in LHCb simulation, overlaid with the results of fitting the resolution function of Eq. 31. (a) shows the fit to the low-q^2 region $0.1 < q^2 < 3.24\,\text{GeV}^2/c^4$ for simulated $B^0 \to K^{*0}\mu^+\mu^-$ events (blue), along with the Gaussian core (red) and double CB (green) contributions separately. (b) shows the fit to the mid-q^2 region (blue) $3.24 < q^2 < 11.56\,\text{GeV}^2/c^4$ for simulated $B^0 \to J/\psi K^{*0}$ events and (c) shows the fit to the high-q^2 region (blue) $11.56 < q^2 < 18.0\,\text{GeV}^2/c^4$ for simulated $B^0 \to \psi(2S)K^{*0}$ events. In the latter two plots, the dashed orange curves show the final resolution shape after the fit to data, which agrees well with the results from simulation.

resolution parameters are fixed in the fit to data since the number of signal candidates in this region is insufficient to allow them to vary.

In the mid-q^2 and high-q^2 regions, all of the resolution parameters are allowed to vary freely in the fit to data. Fits to the J/ψ and $\psi(2S)$ peaks in simulated $B^0 \to J/\psi K^{*0}$ and $B^0 \to \psi(2S)K^{*0}$ decays are shown in Figs. 2b, and 2c, respectively, along with a comparison to the final resolution shape obtained from the fit to data. Excellent agreement between the resolution models obtained from data (orange) and simulation (blue) is observed in all areas except for the far tails of the resonance peaks, giving additional confidence in the accuracy of the simulations and therefore also in the low-q^2 resolution model.

3.4 Full signal probability density function

The full signal Probability Density Function (PDF) has the form,

$$\mathcal{P}_{\text{Sig},i}(\cos\theta_\ell, \cos\theta_K, \phi, q^2) = \frac{1}{\mathcal{N}}\left[\frac{\mathrm{d}^4\left(\Gamma + \bar{\Gamma}\right)\left(B^0 \to K^{*0}\mu^+\mu^-\right)}{\mathrm{d}q^2_{\text{true}}\mathrm{d}\vec{\Omega}} \otimes R_i(q^2 - q^2_{\text{true}})\right]$$

$$\times \epsilon(\cos\theta_\ell, \cos\theta_K, \phi, q^2), \tag{32}$$

where the $\otimes$ symbol indicates a convolution, and the index i labels the q^2 region. The angular resolution of the detector is not accounted for in the signal model. Based on simulation, the angular resolution is around $40\,\text{mrad}$ for θ_l and θ_K, and around $100\,\text{mrad}$ for ϕ, with little dependence on q^2. The angles and q^2 used in the determination of the acceptance in Eq. 30 refer to the true values in the simulation and not the reconstructed ones. However, here in Eq. 32 it is used for the reconstructed ones. As the variation in efficiency is very slow compared to the resolution in all dimensions, this difference only leads to a negligible systematic uncertainty on the results. The CP-averaged $B^0 \to K^{*0}\mu^+\mu^-$ theoretical decay rate contains all parameters of interest, including the Wilson Coefficients and all parameters describing both the local and nonlocal hadronic form factors. The expression is built up by constructing the angular coefficients of Eq. 4 from the transversity amplitudes given in Eqs. 6–10 (see Appendix A for details). The acceptance function is fixed from simulation, whilst the q^2 resolution adds a small number of nuisance parameters to the signal model which are either allowed to vary in the fit to data or are fixed from simulation, as already described in Sec. 3.3.

To improve the q^2 resolution, a constraint is applied when determining the value of q^2. The constraint involves performing a kinematic refit of the decay chain using a Kalman filter [68] to vary the four-momenta of the final-state particles within their uncertainties such that the reconstructed mass is constrained to the known B^0 mass [37]. Unless otherwise stated, the use of q^2 throughout this paper always refers to the constrained value.

3.5 Background composition

The model requires to describe the contribution from processes other than the signal decay which contaminate the final sample. The combinatorial background, discussed already in Sec. 3.2, is the only contribution which remains significant after the full selection and is modelled as described in Sec. 4.2. Beyond this, several physical background sources are identified, referred to as peaking backgrounds, which are suppressed using a combination of dedicated vetoes and machine-learning techniques.

The $B^+ \to K^+\mu^+\mu^-$ mode mimics the signal decay when a random π^- is combined with the daughters of the true decay. This background is vetoed by removing all candidates with $m(K^+\pi^-\mu^+\mu^-) > 5380\,\text{MeV}/c^2$ in which the mass of the $K^+\mu^+\mu^-$ combination is also compatible with the known B^+ mass. The $B^0_s \to K^+K^-\mu^+\mu^-$ decay forms a peaking background when one of the kaons is misidentified as a pion. The dominant contribution arises from $B^0_s \to \phi(1020)\mu^+\mu^-$ decays followed by the transition $\phi(1020) \to \mu^+\mu^-$. Several vetoes are applied to remove this contribution, accounting for both the resonant and nonresonant parts of the $m(K^+K^-)$ spectrum. Candidates are first reconstructed, assigning the kaon mass to the pion. For the resonant $\phi(1020)$ channel, strict pion PID requirements are applied to those candidates with reconstructed B and K^+K^- masses

that are compatible with the known B_s^0 and $\phi(1020)$ masses. For the nonresonant mode, the requirement that the reconstructed K^+K^- mass is compatible with the $\phi(1020)$ mass is removed, and slightly modified PID cuts are applied. The decay $B^0 \to \pi^+\pi^-\mu^+\mu^-$ forms a peaking background in a similar way if one of the pions is misidentified as a kaon. In this case, the dominant contribution comes via the $B^0 \to \rho^0(\to \pi^+\pi^-)\mu^+\mu^-$ resonant decay. Analogous PID requirements are applied to remove these decays after assigning a pion mass hypothesis to the reconstructed kaon. Backgrounds stemming from the double misidentification of the final-state particles in signal decays, e.g. when the π^- (K^+) of the K^{*0} meson is misidentified as a K^- (π^+) and vice versa, are highly suppressed due to PID requirements on the final state particles.

Several more peaking background sources arise from the $\Lambda_b^0 \to pK^-\mu^+\mu^-$ and $\Lambda_b^0 \to p\pi^-\mu^+\mu^-$ decays, which mimic the signal if one or both hadrons are misidentified and are reconstructed as a K^{*0} decay. These backgrounds are removed by reconstructing decays under the alternative mass hypotheses, and requiring that the final-state hadrons satisfy strict PID criteria if the mass is close to the known Λ_b^0 mass.

Double hadron misidentification leads to peaking backgrounds that originate from true resonant signal decays, $B^0 \to J/\psi K^{*0}$ and $B^0 \to \psi(2S)K^{*0}$, with two of the final-state particles swapped, i.e. the π^- (K^+) is misidentified as a μ^- (μ^+) and vice versa. These decays are vetoed by assigning the muon mass to the pion (kaon), and removing events for which the $\pi^-\mu^+$ ($K^+\mu^-$) combination has a mass close to either the known J/ψ or $\psi(2S)$ mass, and the π^- (K^+) also fails to satisfy stringent PID criteria.

An additional peaking background can be formed from $B^+ \to K^{*+}\mu^+\mu^-$ decays with either $K^{*+} \to K_S^0\pi^+$ or $K^{*+} \to K^+\pi^0$ states and the charged hadron from these decays is combined with a random charged pion or kaon from elsewhere in the event to create the K^{*0} candidate. These events are less trivial to separate from the signal; hence, two BDTs classifiers are trained using simulation for the purpose of discriminating between $B^0 \to K^{*0}\mu^+\mu^-$ decays and $B^+ \to K^{*+}\mu^+\mu^-$ decays in each of the two K^{*+} decay modes. A total of fourteen variables are used to train the BDT algorithm including various kinematic and isolation variables, with the highest discriminating power provided by the significance of the impact parameter with respect to the PV of the randomly charged hadron used to create the K^{*0} candidate, i.e. the K^- in the BDT classifier trained to reject $B^+ \to K^{*+}(\to K_S^0\pi^+)\mu^+\mu^-$ decays, and the π^- in the BDT algorithm trained to reject $B^+ \to K^{*+}(\to K^+\pi^0)\mu^+\mu^-$ decays.

4   Data analysis

The primary aim of the analysis is to determine the Wilson Coefficients of the $b \to s\ell^+\ell^-$ WET Hamiltonian as well as to obtain a full description of the nonlocal amplitudes. The measurement is performed by fitting the $B^0 \to K^{*0}\mu^+\mu^-$ angular distribution of Eq. 4, which provides sensitivity to the WET parameters through the q^2 dependent angular observables. The latter are parameterised in terms of a set of theoretical amplitudes, which depend directly on the $b \to s\ell^+\ell^-$ Wilson Coefficients and various parameters describing the nonlocal contributions. This approach of explicitly modelling the signal in the q^2 dimension including the charmonium resonance regions is the main new feature with repect to previous angular analyses of the $B^0 \to K^{*0}\mu^+\mu^-$ decay mode.

A full description of the signal model is provided in Sec. 2. The signal decay rate

Table 2: The signal fraction in the full mass range $5220 \leq m(K^+\pi^-\mu^+\mu^-) \leq 5840\,\mathrm{MeV}/c^2$ determined in five q^2 regions chosen to isolate different combinatorial background contributions.

Category	q^2 region [GeV^2/c^4]	Signal fraction ($f_{\mathrm{Sig},i}^{\mathrm{full}}$)
Low-q^2	$[0.10, 3.24]$	0.9196 ± 0.0088
Fully combinatorial mid-q^2	$[3.24, 8.20] \cup [10.6, 11.56]$	0.8045 ± 0.0093
Resonant mid-q^2	$[8.20, 10.6]$	0.9934 ± 0.0002
Fully combinatorial high-q^2	$[11.56, 12.40] \cup [14.40, 18.00]$	0.8656 ± 0.0088
Resonant high-q^2	$[12.40, 14.40]$	0.9862 ± 0.0010

is modelled in five dimensions, *i.e.* the three helicity angles $\cos\theta_\ell$, $\cos\theta_K$, and ϕ, along with q^2, and m_B masses. The signal shape in the mass of the $K\pi$ system is integrated out as mentioned in Sec. 2.2. This is done in order to simplify the already very complex model. The model is ultimately used to perform an unbinned maximum-likelihood fit to the data, simultaneously in the $\cos\theta_\ell$, $\cos\theta_K$, ϕ, and q^2 dimensions, within the range $0.1 < q^2 < 18.0\,\mathrm{GeV}^2/c^4$. In order to constrain the background, two separate fits are performed in different ranges of the B^0 mass as described in Sec. 4.1 and 4.2.

4.1 Determination of the signal fraction

One-dimensional fits to the $m(K^+\pi^-\mu^+\mu^-)$ distribution are performed in the range $5220 \leq m(K^+\pi^-\mu^+\mu^-) \leq 5840\,\mathrm{MeV}/c^2$, to determine the fraction of signal events $f_{\mathrm{Sig}}^{\mathrm{full}}$ relative to the background in the full mass range. The signal fraction is determined simultaneously in the five separate q^2 regions given in Table 2. These regions correspond to the same three regions as those in Table 1, but with the mid- and high-q^2 regions further subdivided. This is done in order to capture the fact that the combinatorial background composition differs depending on whether the q^2 value is close to one of the J/ψ or $\psi(2S)$ resonances, or away of them. In particular, within the resonance regions (labelled resonant mid- and high-q^2 in Table 2), the dominant contribution comes from true resonant dimuon candidates combined with a random $K^+\pi^-$ combination, resulting in a strongly peaking q^2 distribution. Outside the resonance regions, fully random combinations of $K^+\pi^-\mu^+\mu^-$ are the dominant contribution with no peaking structure, henceforth referred to as fully combinatorial.

Similar to previous LHCb analyses of $B^0 \to K^{*0}\mu^+\mu^-$ decays [4,5], the shape of the signal mass is modelled using the sum of two single-sided CB functions,

$$\mathcal{P}_{B^0} = \frac{1}{N}\left[f_1 C(m; \mu, \sigma_1, \alpha, n) + (1-f_1)C(m; \mu, \sigma_2, -\alpha, n)\right], \qquad (33)$$

where f_1 represents the fraction of the first CB component, N is normalisation constant, and m represents the reconstructed B^0 mass $m(K^+\pi^-\mu^+\mu^-)$. The best description of the data is obtained with symmetric CB tails on opposite sides of the Gaussian core. Due to large correlations between the CB tail parameters, only the α parameter is allowed to vary in the fit, whilst the n parameter is fixed to the value obtained in Ref. [4]. For the signal, both a B^0 and a B_s^0 component with the same shape are included with a fixed peak offset given by the known difference in the B_s^0 and B^0 masses $\Delta m \equiv m(B_s^0) - m(B^0) = 87.19\,\mathrm{MeV}/c^2$ [37]. The fraction $f_{B_s^0}$ of the B_s^0 component relative to the B^0 component is allowed to vary.

The combinatorial background is modelled with an exponential function, leading to a total PDF of the form

$$\mathcal{P}_{\text{Total},i}(m) = f_{\text{Sig},i}^{\text{full}} \left[(1 - f_{B_s^0})\mathcal{P}_{B^0}(m) + f_{B_s^0}\mathcal{P}_{B_s^0}(m) \right] + (1 - f_{\text{Sig},i}^{\text{full}})\mathcal{P}_{\text{Bkg},i}(m), \qquad (34)$$

where the index i labels the q^2 region. The fits to the different q^2 regions can be seen in Fig. 3, and the values of $f_{\text{Sig},i}^{\text{full}}$ obtained for each region are listed in Table 2. The signal fractions of Eq. 34 are used to calculate the number of background events per q^2 region contained in the signal region, which is defined as a $40\,\text{MeV}/c^2$ region around the B^0 mass peak, $5259.58 \leq m(K^+\pi^-\mu^+\mu^-) \leq 5299.58\,\text{MeV}/c^2$.

4.2 Background fit in the upper B^0 mass sideband

Following the determination of the signal fractions, a fit to the upper B^0 mass sideband $(5440 \leq m(K^+\pi^-\mu^+\mu^-) \leq 5840\,\text{MeV}/c^2)$ is performed simultaneously in the three q^2 regions defined in Table 1. Special care is taken in the sideband fit to account for the use of a B^0 mass constraint in the fit to the signal region (see Sec. 4.3 below). The combinatorial background events are not the decay products of a real B^0 meson; hence, the mass constraint causes a distortion of the background q^2 distribution which is correlated with the reconstructed B^0 mass. This effect can be observed by contrasting Fig. 4a, which shows the reconstructed B mass as a function of q^2 without the mass constraint, and 4b showing the same with the mass constraint. The q^2 positions of the J/ψ- and $\psi(2S)$-dominated combinatorial peaks are observed to vary as a function of m_B in a way that is impractical to model. To remedy this, the upper B^0 mass sideband is divided into 10 windows, each of width $40\,\text{MeV}/c^2$. In each window, the $K\pi\mu\mu$ mass is constrained to the centre of the region, so as to mimic the distortion of the background q^2 distribution that occurs in the signal region that also is $40\,\text{MeV}/c^2$ wide. As a result of this, the J/ψ and $\psi(2S)$ peaks are aligned between the subregions and the signal region, as shown in Fig. 4c.

In each of the ten m_B background windows, the background shape is modelled in the $\cos\theta_\ell$, $\cos\theta_K$, ϕ, and q^2 dimensions, separately for the five q^2 regions defined in Table 2. Those five q^2 regions are then reduced to the three regions of Table 1 by adding the PDFs for the relevant contributions in each region. The PDF for the sideband fit is defined as

$$\mathcal{P}(q^2, \vec{\Omega}) = \begin{cases} \mathcal{P}_{\text{comb}}(q^2, \vec{\Omega}) & \text{low-}q^2 \\ (1 - f_{J/\psi})\mathcal{P}_{\text{comb}}(q^2, \vec{\Omega}) + f_{J/\psi}\mathcal{P}_{J/\psi}(q^2, \vec{\Omega}) & \text{mid-}q^2 \\ (1 - f_{\psi(2S)})\mathcal{P}_{\text{comb}}(q^2, \vec{\Omega}) + f_{\psi(2S)}\mathcal{P}_{\psi(2S)}(q^2, \vec{\Omega}) & \text{high-}q^2 \end{cases}, \qquad (35)$$

where $f_{J/\psi}$ and $f_{\psi(2S)}$ represent the resonant background fractions relative to the fully combinatorial components in the mid- and high-q^2 regions, respectively.

Each of the PDFs in Eq. 35 is assumed to factorise completely such that each dimension can be modelled independently. For the q^2 dimension, the fully combinatorial contribution is modelled using the Weibull function [69]; while the J/ψ- and $\psi(2S)$-dominated contributions are modelled using CB functions. The $\cos\theta_\ell$ and ϕ dimensions are modelled using second order Chebyshev polynomials; whilst the $\cos\theta_K$ dimension is modelled with second order Bernstein polynomials.

A complication arises due to the $B^+ \to K^+\mu^+\mu^-$ veto described in Sec. 3.5. While the veto has no effect in the signal region, it causes a drop in the number of combinatorial

19
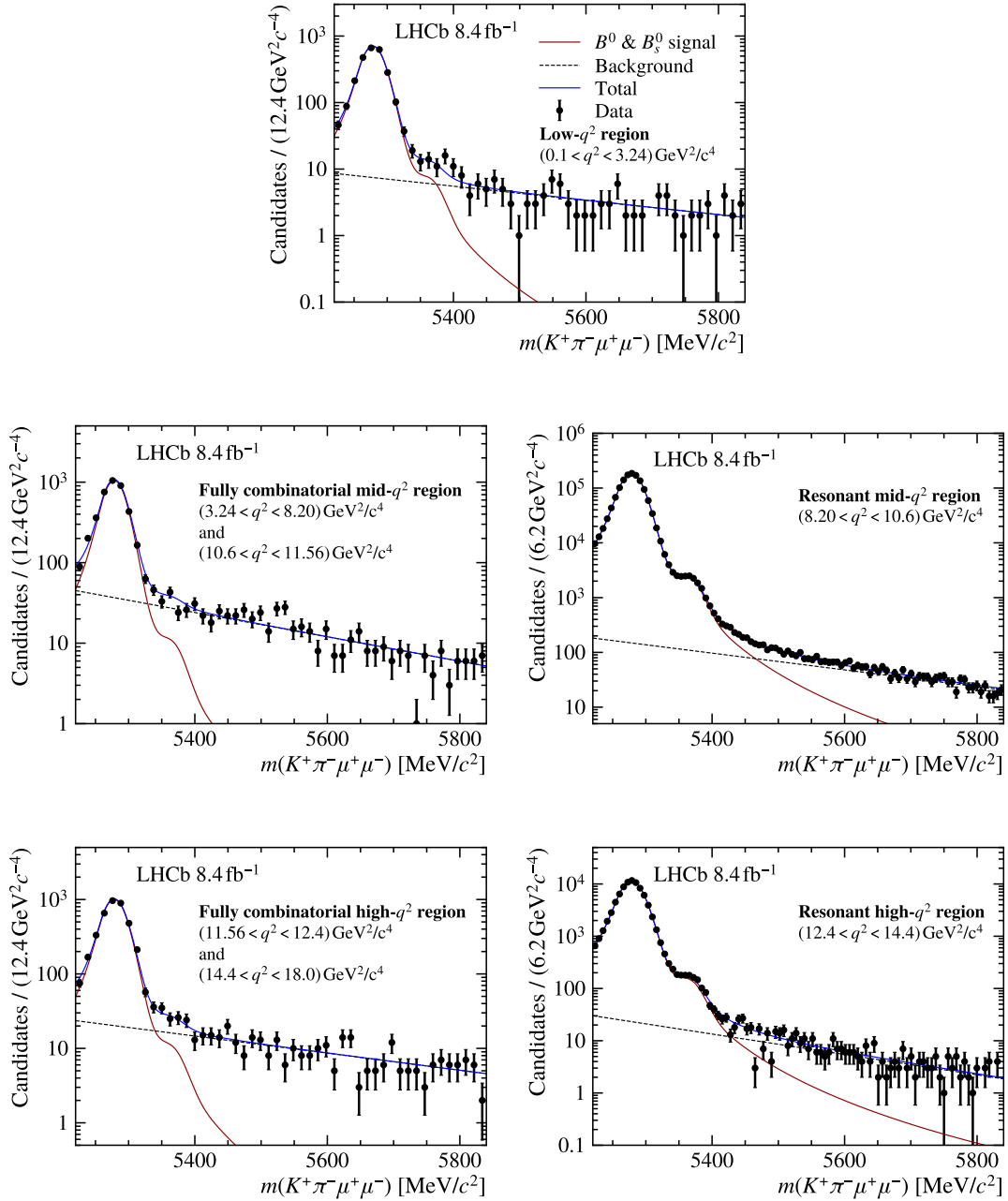
Figure 3: The mass distribution $m(K^+\pi^-\mu^+\mu^-)$ of candidates in the data in five separate q^2 regions. The data is overlaid with the results of a simultaneous fit to determine the signal fractions.
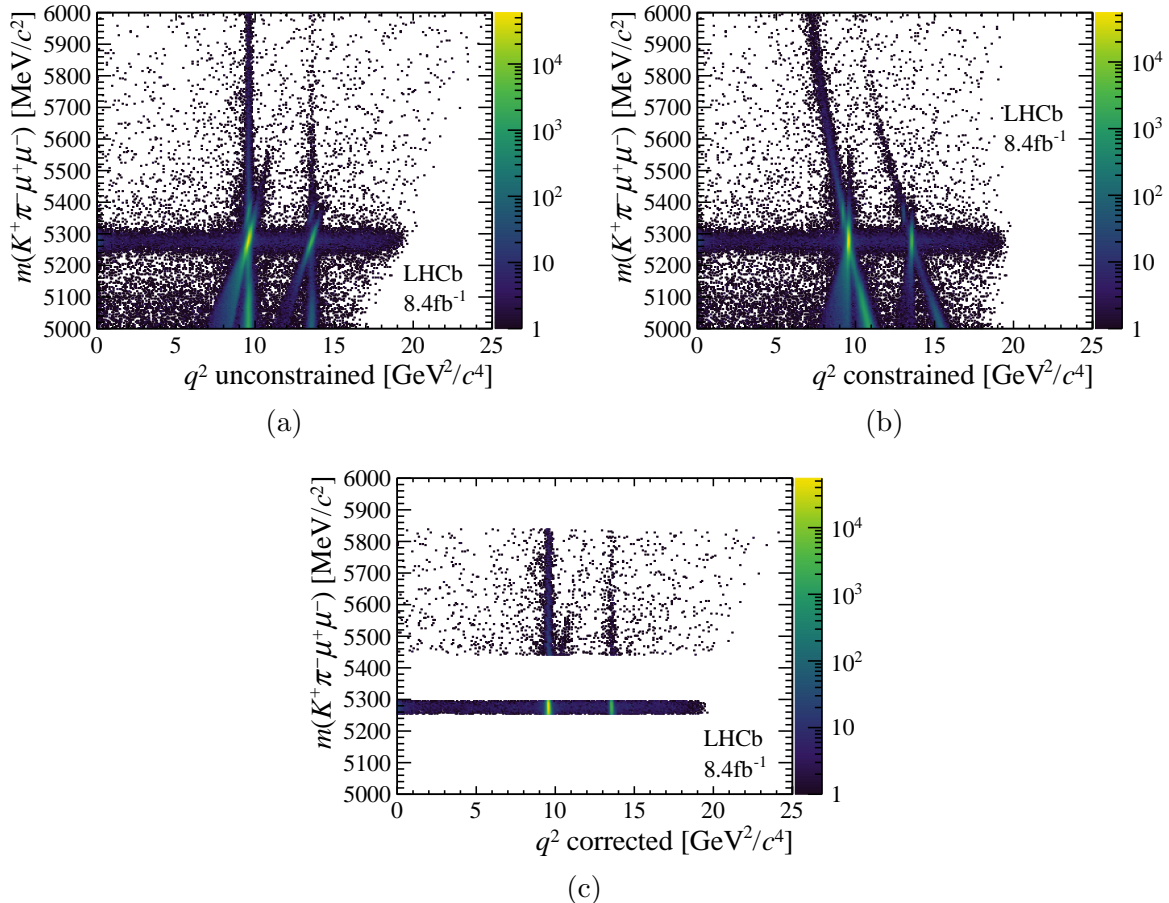
Figure 4: Distributions of candidates in data with different treatments of the B^0 mass constraint when determining q^2. In (a) no constraint is applied, in (b) the final state is constrained to the B^0 mass, while in (c) the final-state mass is constrained to the centre of each of the $40\,\mathrm{MeV}/c^2$ wide signal and upper mass background windows. In all the plots, the signal regions correspond to the horizontal band. The diagonal lines in (a) that become vertical lines in (b) are the tails of poorly reconstructed $B^0 \to J/\psi K^{*0}$ and $B^0 \to \psi(2S)K^{*0}$ decays.

background events in a $\cos\theta_K$ region of the phase space that depends on the reconstructed B^0 mass. If ignored, it leads to the wrong background shape extrapolated into the signal region. The solution employed is to exclude the affected $m(K^+\pi^-\mu^+\mu^-)$ dependent $\cos\theta_K$ interval in each of the ten sideband regions. This reduces the amount of events in the sideband fit by approximately 15% but prevents any bias in the extrapolation.

To model the shape of the combinatorial background in the signal region, an extrapolation is made of the parameters describing the angular and q^2 distributions in each of the ten sideband bins. In this way, the angular distribution in the signal region is described by Eq. 35 as well. The parameters obtained from the extrapolation and their corresponding correlation matrix are used in the signal fit described below.

4.3   Fit in the signal region

The final step consists of an unbinned maximum likelihood fit to the four-dimensional ($\cos\theta_\ell$, $\cos\theta_K$, ϕ, and q^2) distribution in the signal region. The fit is performed simultane-

21

ously in the three q^2 regions shown in Table 1, with the total PDF in each region given by

$$\mathcal{P}_{\text{Total},i}(\vec{\Omega}, q^2) = f_{\text{Sig},i}\mathcal{P}_{\text{Sig},i}(\vec{\Omega}, q^2) + (1 - f_{\text{Sig},i})\,\mathcal{P}_{\text{Bkg},i}(\vec{\Omega}, q^2), \qquad (36)$$

where $\mathcal{P}_{\text{Sig},i}(\vec{\Omega}, q^2)$ is the full experimental signal PDF described in Eq. 32, and $\mathcal{P}_{\text{Bkg},i}(\vec{\Omega}, q^2)$ is the corresponding background PDF from Eq. 35. The fractions $f_{\text{Sig},i}$ correspond to the fractions of signal events within each of the signal regions. They are not independent free parameters, rather, they are derived from the fitted signal fractions in Eq. 34, which correspond to the full mass range and the five q^2 regions of Table 2. In the fit, the background shape is constrained using the results of the extrapolation from sideband fits and the background yield is constrained using signal fractions from the m_B mass fit as given in Table 2. The signal angular distribution is modelled according to Sec. 3.3. The baseline fit configuration consists of 150 free parameters.

The complex amplitudes for each polarisation state of the nonlocal components A_j^λ appearing in Eqs. 24 and 28 are determined from the fit to the data. For amplitudes that are expected to be significantly different from zero, the fit is performed in terms of the magnitude $|A_j^\lambda|$ and phase δ_j^λ. In contrast, for components with a small expected amplitude the fit is performed in terms of the real $\Re(A_j^\lambda)$ and imaginary $\Im(A_j^\lambda)$ components. This ensures better stability of the fit.

The scale of both the $B^0 \to K^{*0}\mu^+\mu^-$ local and nonlocal amplitudes are determined through the known value of the compound branching fraction $\mathcal{B}(B^0 \to J/\psi K^{*0})\mathcal{B}(J/\psi \to \mu^+\mu^-)$ and by scaling the three polarisation amplitudes $A_{J/\psi}^{0,\|,\perp}$ such that

$$\mathcal{B}(B^0 \to J/\psi K^{*0})\mathcal{B}(J/\psi \to \mu^+\mu^-) = |A_{J/\psi}^0|^2 + |A_{J/\psi}^\||^2 + |A_{J/\psi}^\perp|^2. \qquad (37)$$

The branching fraction $\mathcal{B}(B^0 \to J/\psi K^{*0})$ is taken from Ref. [46] and the branching fraction $\mathcal{B}(J/\psi \to \mu^+\mu^-)$ is taken from Ref. [37]. In the fit this is implemented by calculating $|A_{J/\psi}^0|$ from Eq. 37 rather than having it as a free parameter. The uncertainty of the branching fraction $\mathcal{B}(B^0 \to J/\psi K^{*0})$ is a limiting source of uncertainty on numerous nonlocal parameters and is the largest systematic uncertainty on the Wilson Coefficients, as discussed in Sec. 5.

The kinematically allowed q^2 region of $B^0 \to K^{*0}\mu^+\mu^-$ decays ranges from $4m_\mu^2$ to $(m_B - m_{K\pi}^{\max})^2$, where $m_{K\pi}^{\max}$ denotes the maximum mass of the $K^{*0} \to K^+\pi^-$ system. In this analysis $m_{K\pi}^{\max}$ is set to $0.996\,\text{GeV}/c^2$ as discussed in Sec. 2.2. This results in a q^2 phase-space range of $0.044 < q^2 < 18.34$ GeV$^2/c^4$. In order to reduce the model dependence of the q^2 resolution in regions where the decay rate varies rapidly with q^2, the measurement is performed in the reconstructed q^2 range of $0.1 < q^2 < 18.0$ GeV$^2/c^4$.

The analysis was performed in a blind fashion until finalised, by implementing an unknown offset to the values of the Wilson Coefficients $\mathcal{C}_{9,10}^{(\prime)}$ and $\mathcal{C}_{9\tau}$. Additionally, the signs of the differences between the Wilson Coefficients and their Standard Model values are switched randomly. Pseudoexperiments are performed following an identical procedure to that used for the data fit to validate the full analysis. The bias and error coverage obtained from the pull distributions for the Wilson Coefficients are listed in Table 3. The observed biases are $\lesssim 30\%$ compared to the statistical uncertainty for all parameters, and are accounted for as corrections to the final results.

Table 3: The means and widths of the pull distributions in pseudoexperiments for the Wilson Coefficients. The bias is quoted as a fraction of the statistical uncertainty on the parameter.

Variable	Mean (bias)	Width (coverage)
$\mathcal{C}_9$	-0.27 ± 0.06	1.00 ± 0.04
$\mathcal{C}_{10}$	-0.13 ± 0.06	0.94 ± 0.04
$\mathcal{C}_9'$	-0.09 ± 0.06	1.05 ± 0.04
$\mathcal{C}_{10}'$	-0.34 ± 0.06	0.99 ± 0.04
$\mathcal{C}_{9\tau}$	-0.20 ± 0.06	1.03 ± 0.04

5 Systematic uncertainties

Several sources of systematic uncertainty are considered for this analysis, including those related to the modelling of the signal, backgrounds, detector effects, and the analysis method and implementation. The most significant effects are described in detail, followed by a brief overview of some additional effects which are considered but found to be subdominant or negligible. The final parameter uncertainties are obtained by combining the statistical covariance matrix from the likelihood fit with the total combined systematic covariance matrix accounting for all non-negligible effects. The systematic covariance matrices are obtained by performing fits to pseudoexperiments using alternative fit configurations and/or modifying the pseudoexperiments in a manner representative of the effect in question.

5.1 Normalisation to the $B^0 \to J/\psi K^{*0}$ branching fraction

The dominant source of systematic uncertainty on the parameters of interest is found to arise from the normalisation to the $B^0 \to J/\psi K^{*0}$ branching fraction, which is only known with a relative uncertainty of 6.8% [46]. Varying the known $B^0 \to J/\psi K^{*0}$ branching fraction within its uncertainties translates to an effect of the order 50% of the statistical uncertainty for the $\mathcal{C}_9$, and 100% for the $\mathcal{C}_{10}$ parameters. It should be noted that the reason this effect is so significant is due to the dramatically improved statistical precision in this analysis relative to the Belle measurement of $\mathcal{B}(B^0 \to J/\psi K^{*0})$ [46]. This is currently an irreducible systematic uncertainty, but can be directly improved in the future with a new precise measurement of the $B^0 \to J/\psi K^{*0}$ branching fraction, *e.g.* from the Belle II experiment.

5.2 Exotic charmonium-like states

The presence of charmonium-like resonances in the $J/\psi\pi$ and $\psi(2S)\pi$ spectra, so-called exotic $T_{c\bar{c}1}$ states[2], leads to the interference of the decay amplitudes $B \to T_{c\bar{c}1}(\to \psi\pi)K$ with both the rare decay and $B \to \psi K^{*0}$ final states. This analysis performs a fit across the full q^2 spectrum, including the J/ψ and $\psi(2S)$ regions, without accounting for these exotica contributions. The reason for not including these amplitude components in the fit is mainly due to computational efficiency; the $B \to T_{c\bar{c}1}(\to \psi\pi)K$ decays contribute with different functional angular dependencies, thus the decay rate no longer factorises into a

---

[2]Previously known as Z_c states

simple sum of products of $J_i(q^2)$ and $f(\Omega)$ terms as given in Eq. 4. To assess the impact of neglecting the exotica contributions, a correction is derived by generating pseudodata that contain all of the baseline local and nonlocal amplitudes added coherently to the exotica ones, following the procedure of Refs. [46, 70, 71]. The pseudoexperiments are fit back using the baseline model that neglects the exotic states. The exotic amplitudes are fixed in the generation of the pseudodata to the central values from measurements made by the Belle collaboration [46, 71]. The resulting average shift of the parameters from their generated values is taken as the correction. With the exception of the J/ψ and $\psi(2S)$ magnitudes and phases, the exotica correction to the parameters of interest is small ($\lesssim 20\%$) relative to the statistical uncertainty.

A systematic uncertainty is derived for the correction by varying the exotic amplitudes within their measured 1σ uncertainties and recalculating the correction. Again, with the exception of the J/ψ and $\psi(2S)$ magnitudes and phases, the systematic uncertainty on the exotica correction is $\lesssim 20\%$ relative to the statistical uncertainty.

For the J/ψ and $\psi(2S)$ parameters, the exotica correction and associated systematic uncertainty are large relative to the statistical uncertainty (from 100% to 250%); however, the absolute effect remains small given the excellent statistical precision achieved on the resonance magnitudes and phases.

5.3 Acceptance

The acceptance function described in Sec. 3.3 is determined from simulated samples that are reweighted to agree with data. Corrections are applied specifically to ensure agreement in the hardware trigger and tracking efficiencies, the multiplicity of tracks in an event, and the distributions of PID and B^0 meson kinematic variables. The weights applied to the simulated samples have associated statistical and systematic uncertainties that propagate through to the eventual determination of the signal parameters. To assess the impact of these uncertainties, ensembles of pseudoexperiments are used in which alternative weights are derived and subsequently used to produce modified PDFs with alternative acceptance coefficients. Pseudoexperiments are generated from the alternative PDFs and then fitted back using both the baseline and alternative (true) PDFs.

The largest effect is found to come from the corrections to the B^0 meson kinematics. Relative to the respective statistical uncertainties, the effect is approximately 10% for the Wilson Coefficients and 200% for the magnitudes of the parallel and transverse J/ψ amplitudes.

The baseline weights for these kinematic corrections are derived by comparing the distributions of the B^0 meson transverse momentum, pseudorapidity, vertex quality, and impact parameter quality between $B^0 \to J/\psi K^{*0}$ decays in simulation and data. The alternative weights are derived by performing the same comparisons for $B^0 \to \psi(2S)K^{*0}$ decays in simulation and data.

5.4 Two-particle open-charm constraint

As described in Sec. 2.5.1, a Gaussian constraint is placed on the coefficients in Eq. 28 describing the size of the open-charm contributions to maintain the stability of the fit. The constraint restricts the real and imaginary parts, separately, of each two-particle open-charm state ($D\overline{D}$, $D^*\overline{D}$ and $D^*\overline{D}^*$) to be of a similar size to one another. A separate

constraint is used for each polarisation amplitude. The constraint is given a conservative width of 1.0,[3] but could nonetheless cause biases in the open-charm contributions, as well as other parameters, if the components that are constrained have differences larger than this in data. To asses this bias, pseudoexperiments are generated with the difference between the open-charm components set to 1.5. These pseudoexperiments are then fitted twice, once with the baseline constraint-width, and once with an unbiased constraint-width of 1.5. The difference in the fit results is assigned as a systematic uncertainty, and besides the open-charm parameters, the main affected parameters are C_9 and $C_{9\tau}$, with systematic uncertainties of 24% and 29% of the statistical uncertainty, respectively.

5.5 Subdominant effects

The experimental resolution in the angles $\cos\theta_\ell$, $\cos\theta_K$, and ϕ is not explicitly accounted for in the signal model. Unlike the q^2 spectrum, however, the angular distributions contain no sharp peaks and are thus not greatly affected by the detector resolution. Ensembles of pseudoexperiments emulating the effects of the angular resolution are used to confirm that this has no significant effects on the signal parameters of interest.

The q^2 resolution is accounted for in the baseline model as described in Sec. 3.3. As an approximation, the parameters of the resolution model are assumed to remain constant within each q^2 region. Pseudoexperiments investigating the effects of mismodelling the q^2 resolution are performed and no significant effects are observed to result from this assumption.

The mass of the $K_0^{*0}(700)$ scalar state has a large uncertainty. Varying the mass in the interval $0.680 < m_{K_0^{*0}(700)} < 0.900\,\mathrm{GeV}^2/c^4$ results in no significant change apart from the value of the effective form factor for the S-wave which is a nuisance parameter in the fit.

After the full selection has been applied, the fraction of events that contain more than one candidate is approximately 0.18%. These events are unlikely to correspond to multiple true candidates and are not distributed evenly throughout the phase space. However, the distribution of events with multiple candidates is found to be well modelled in simulation, hence all candidates are retained in the subsequent analysis and a small systematic uncertainty related to their inclusion is determined from simulation.

6 Results

The full q^2 spectrum resulting from the simultaneous fit is shown overlaid on the data in Fig. 5. The total PDF is decomposed into signal and background components, and the signal component is further decomposed into the contributions from local amplitudes, one- and two-particle nonlocal amplitudes, and the interference between them. The same results are shown with alternative signal decompositions in Figs. 16 and 17 in Appendix C.1.

The optimal values of the Wilson Coefficients $\mathcal{C}_{9,10}^{(\prime)}$ and $\mathcal{C}_{9\tau}$ are listed in Table 4. The corresponding one-dimensional likelihood profiles are shown in Fig. 6, wherein the 1σ, 2σ, and 3σ confidence intervals are indicated considering both statistical and systematic uncertainties. The SM values for the Wilson Coefficients obtained from Ref. [16, 17] are also indicated in Fig. 6, revealing a 2.1σ deviation in the $\mathcal{C}_9$ fit result, and otherwise

---

[3]For context, the coherent sum of all the $D^{(*)}\overline{D}^{(*)}$ states would saturate the decay rate at around 0.22 [43].

Table 4: Results for the Wilson Coefficients. The first uncertainty is statistical, while the second is systematic.

Wilson Coefficient results	
$\mathcal{C}_9$	$3.56 \pm 0.28 \pm 0.18$
$\mathcal{C}_{10}$	$-4.02 \pm 0.18 \pm 0.16$
$\mathcal{C}'_9$	$0.28 \pm 0.41 \pm 0.12$
$\mathcal{C}'_{10}$	$-0.09 \pm 0.21 \pm 0.06$
$\mathcal{C}_{9\tau}$	$(-1.0 \pm 2.6 \pm 1.0) \times 10^2$
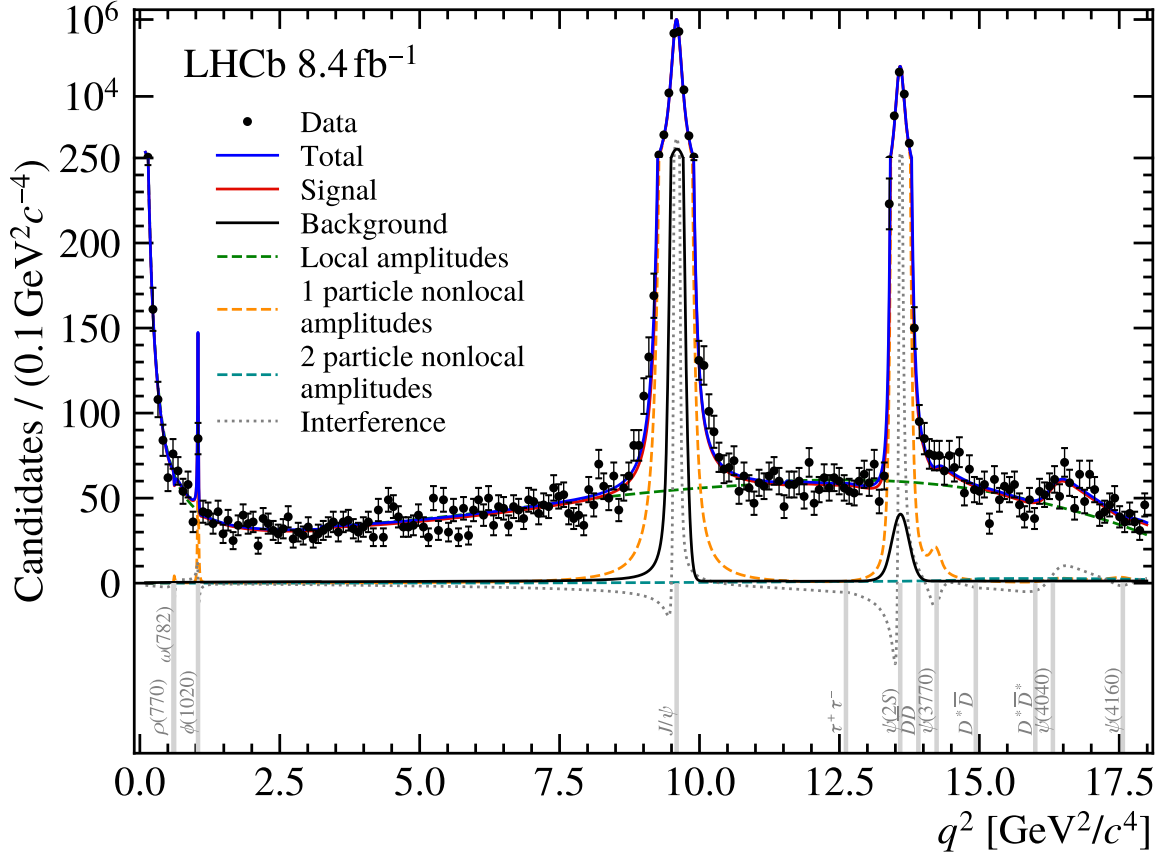
Figure 5: The q^2 distribution in the data, overlaid with the PDF projection from the baseline data fit. The total PDF is decomposed into signal and background components, with the signal contributions further decomposed into local and nonlocal contributions as described in Sec. 2.5.1. Note the hybrid linear/log scale to incorporate the very tall peaks from the charmonium states.

good agreement with SM. Two-dimensional likelihood profiles for $\mathcal{C}^{(')}_{9,10}$ are also obtained, as shown in Fig. 7. The parameters of the dominant nonlocal contributions, *i.e.* the one-particle resonance amplitudes, are listed in Tables 5 and 6, and the two-particle and nonresonant contributions to the $\mathcal{C}_7$ parameters are given in Table 7.

The prior and posterior values for the local form factor parameters are given in Table 8. Projections of the fit on the angles as well as q^2 in the individual subregions can be found in Fig. 15 in Appendix C.
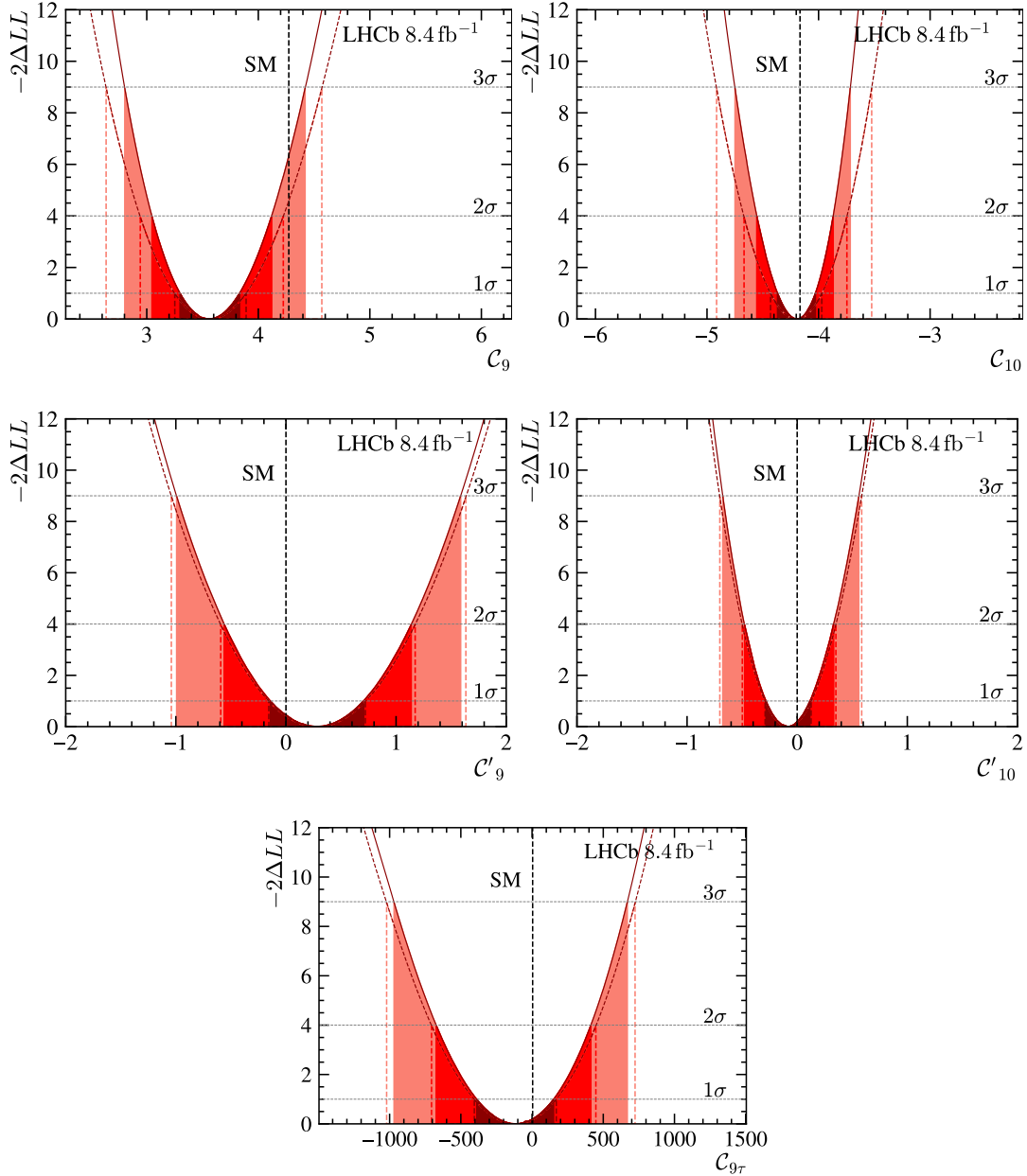
Figure 6: One-dimensional confidence intervals for the Wilson Coefficients, obtained using a likelihood profile method. The shaded regions consider only statistical uncertainties, while the dashed vertical lines indicate the same regions with systematic uncertainties included. The vertical black dashed lines show the Standard Model values.

7 Discussion

The primary observation to be made based on the results of Sec. 6 is that while the nonlocal model used in this analysis shows that there is some contribution of nonlocal amplitudes in the q^2 regions used by previous binned analyses [5], it still prefers a value of $\mathcal{C}_9$ that is shifted from the SM expectation. Based on a one-dimensional profile likelihood scan, shown in Fig. 6, a shift of $\Delta\mathcal{C}_9^{\mathrm{NP}} = -0.71 \pm 0.33$ is observed that corresponds to a 2.1σ deviation from the SM prediction of $\mathcal{C}_9^{\mathrm{SM}} = 4.27$ [16, 17], with both statistical and
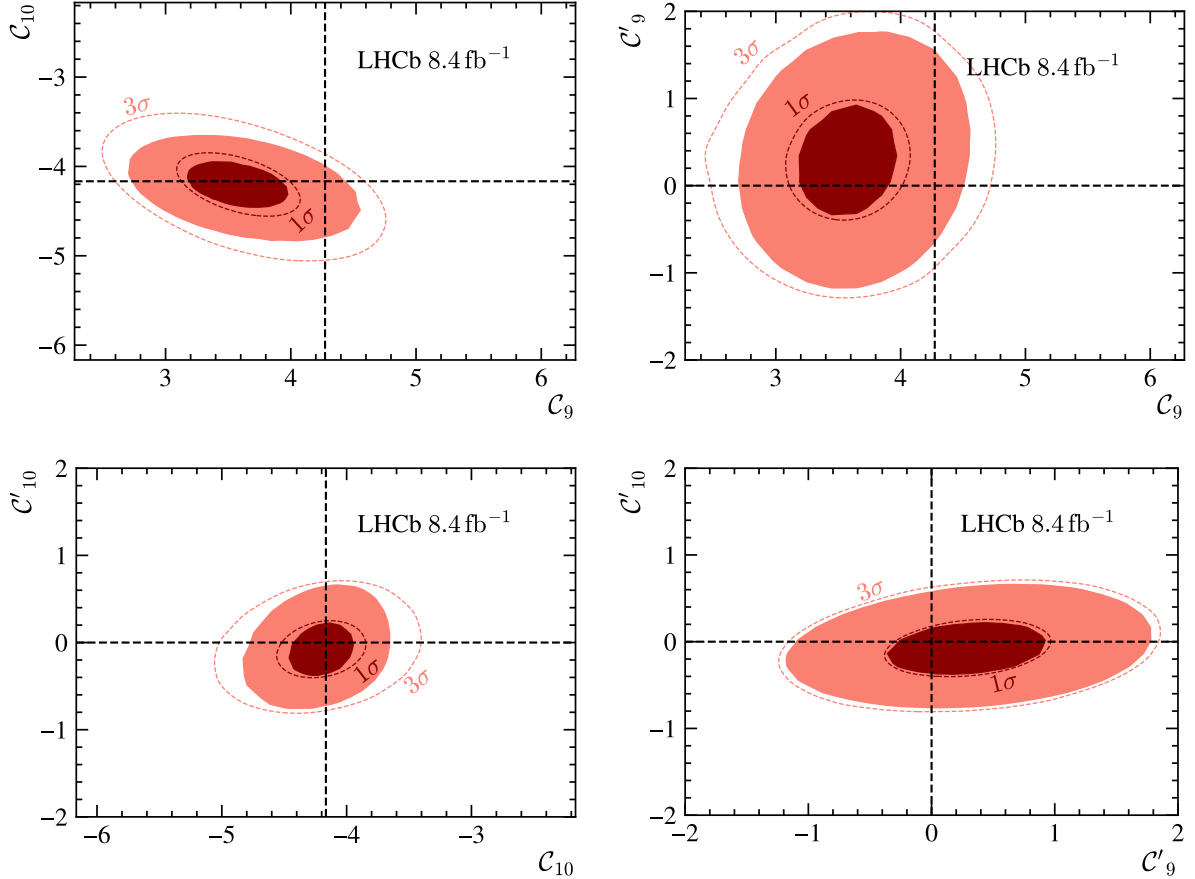
Figure 7: Two-dimensional confidence regions for selected combinations of the Wilson Coefficients, obtained using a likelihood profile method. The shaded regions indicate the 1σ and 3σ confidence regions considering only statistical uncertainties, while the dashed contours indicate the same regions with systematic uncertainties included. The horizontal and vertical dashed lines show the Standard Model values.

systematic uncertainties accounted for. The global significance of the deviation from the SM considering all of the Wilson Coefficients in Table 4 is reduced to 1.5σ. This dilution of the statistical significance is due to the lack of a significant fit quality improvement when introducing the possibility of NP in Wilson Coefficients $\mathcal{C}_{10}$, $\mathcal{C}'_{10}$, $\mathcal{C}'_9$ and $\mathcal{C}_{9\tau}$, compared to only allowing for NP in the Wilson Coefficient $\mathcal{C}_9$. No significant deviation in the Wilson Coefficient $\mathcal{C}_{10}$ is observed, nor any evidence for the presence of right-handed currents.

This is the first direct measurement of the Wilson Coefficient $\mathcal{C}_{9\tau}$, and the value of $\mathcal{C}_{9\tau} = (-1.0 \pm 2.6 \pm 1.0) \times 10^2$ is consistent with both zero and the SM expectation of lepton flavour universality $\mathcal{C}_{9\tau}^{\mathrm{SM}} = 4.27$ [16, 17]. The uncertainty of the $\mathcal{C}_{9\tau}$ parameter is dominated by statistical effects. The largest systematic uncertainty, accounting for $\sim 30\%$ of the total uncertainty, arises from the constraint on the relative size of the $B^0 \to D^{(*)}\overline{D}^{(*)}K^{*0}$ contributions, as detailed in Sec. 2.5.1. The development of theory calculations that can be used to constrain the $B^0 \to D^{(*)}\overline{D}^{(*)}(\to \mu^+\mu^-)K^{*0}$ amplitudes would help improve sensitivity to the Wilson Coefficient $\mathcal{C}_{9\tau}$ in future measurements.

The current best upper limit on the $\mathcal{B}(B^0 \to K^{*0}\tau^+\tau^-)$ branching fraction is 3.1×10^{-3} at 90% Confidence Level [72] (CL), corresponding to an upper limit of $|\mathcal{C}_{9\tau}| < 680$ at

28

Table 5: Results for the (left column) magnitudes and (right column) phases of the dominant one-particle nonlocal contributions. The first uncertainty is statistical, while the second is systematic. The magnitudes, $|A_j^\lambda|$, and phases, δ_j^λ, are defined in Eq. 24. The values of amplitude parameters that are fixed in the fit to the data appear with a dash.

Nonlocal parameter results			
$|A_{J/\psi}^{\parallel}|$	$(3.98 \pm 0.01 \pm 0.15) \times 10^{-3}$	$\delta_{J/\psi}^{\parallel}$	$0.23 \pm 0.01 \pm 0.01$
$|A_{J/\psi}^{\perp}|$	$(3.85 \pm 0.01 \pm 0.14) \times 10^{-3}$	$\delta_{J/\psi}^{\perp}$	$-0.21 \pm 0.00 \pm 0.01$
$|A_{J/\psi}^{0}|$	$-$	$\delta_{J/\psi}^{0}$	$-1.92 \pm 0.05 \pm 0.02$
$|A_{\psi(2S)}^{\parallel}|$	$(9.59 \pm 0.28 \pm 0.82) \times 10^{-4}$	$\delta_{\psi(2S)}^{\parallel}$	$0.84 \pm 0.02 \pm 0.19$
$|A_{\psi(2S)}^{\perp}|$	$(8.38 \pm 0.27 \pm 0.62) \times 10^{-4}$	$\delta_{\psi(2S)}^{\perp}$	$-0.44 \pm 0.02 \pm 0.11$
$|A_{\psi(2S)}^{0}|$	$(13.4 \pm 0.4 \ \pm 1.1 \ ) \times 10^{-4}$	$\delta_{\psi(2S)}^{0}$	$-2.54 \pm 0.13 \pm 0.12$
$|A_{\rho(770)}^{0}|$	$-$	$\delta_{\rho(770)}^{0}$	$1.38 \pm 0.53 \pm 0.65$
$|A_{\omega(782)}^{0}|$	$-$	$\delta_{\omega(782)}^{0}$	$-0.49 \pm 0.92 \pm 0.53$
$|A_{\phi(1020)}^{0}|$	$-$	$\delta_{\phi(1020)}^{0}$	$0.10 \pm 0.82 \pm 0.78$

Table 6: Results for the (left column) real and (right column) imaginary parts of the higher charmonium resonance nonlocal amplitudes as defined in Eq. 24. The first uncertainty is statistical, while the second is systematic.

Nonlocal parameter results ($\times 10^{-5}$)			
$\Re(A_{\psi(3770)}^{\parallel})$	$3.68 \pm 1.34 \pm 0.73$	$\Im(A_{\psi(3770)}^{\parallel})$	$2.87 \pm 1.88 \pm 0.49$
$\Re(A_{\psi(3770)}^{\perp})$	$-3.53 \pm 1.45 \pm 0.47$	$\Im(A_{\psi(3770)}^{\perp})$	$-0.86 \pm 1.56 \pm 0.53$
$\Re(A_{\psi(3770)}^{0})$	$-3.14 \pm 1.39 \pm 0.60$	$\Im(A_{\psi(3770)}^{0})$	$1.67 \pm 1.54 \pm 0.62$
$\Re(A_{\psi(4040)}^{\parallel})$	$-2.39 \pm 1.53 \pm 0.96$	$\Im(A_{\psi(4040)}^{\parallel})$	$-0.71 \pm 1.80 \pm 1.11$
$\Re(A_{\psi(4040)}^{\perp})$	$-2.01 \pm 1.47 \pm 0.59$	$\Im(A_{\psi(4040)}^{\perp})$	$0.35 \pm 1.49 \pm 0.82$
$\Re(A_{\psi(4040)}^{0})$	$-5.62 \pm 1.71 \pm 1.07$	$\Im(A_{\psi(4040)}^{0})$	$1.32 \pm 1.87 \pm 0.99$
$\Re(A_{\psi(4160)}^{\parallel})$	$0.04 \pm 1.72 \pm 0.56$	$\Im(A_{\psi(4160)}^{\parallel})$	$1.91 \pm 1.98 \pm 1.45$
$\Re(A_{\psi(4160)}^{\perp})$	$-2.81 \pm 1.75 \pm 0.61$	$\Im(A_{\psi(4160)}^{\perp})$	$0.32 \pm 0.15 \pm 0.09$
$\Re(A_{\psi(4160)}^{0})$	$1.03 \pm 1.77 \pm 0.39$	$\Im(A_{\psi(4160)}^{0})$	$-1.66 \pm 1.67 \pm 1.04$

90% CL (assuming no NP contribution in the $\mathcal{C}_{10\tau}$ coefficient) or $|\mathcal{C}_{9\tau}| < 600$ (assuming the relation $\mathcal{C}_{10\tau} = -\mathcal{C}_{9\tau}$). The 90% CL upper limit on the $|\mathcal{C}_{9\tau}|$ parameter from this work is $|\mathcal{C}_{9\tau}| < 500$ ($|\mathcal{C}_{9\tau}| < 600$ at 95% CL). To convert the upper limits on the $B^0 \to K^{*0}\tau^+\tau^-$ branching fraction in Ref. [72] to upper limits on the parameter $|\mathcal{C}_{9\tau}|$, the flavio package [73] is used, with local $B^0 \to K^{*0}$ form factors from Ref. [34] and subleading effects parameterised as in Ref. [19].

A number of cross-checks are performed to validate the results of this analysis. The description of the dominant nonlocal amplitudes, *i.e.* those of the J/ψ and $\psi(2S)$ resonances, is validated by comparing the fitted amplitude parameters and resulting angular observables to those measured in previous analyses. To this end, the angular observables F_L, S_3, S_4, S_8, and S_9 are calculated at the J/ψ pole mass, and compared along with the magnitudes and phases $|A_{\parallel,\perp}^{J/\psi}|$ and $\delta_{\parallel,\perp}^{J/\psi}$, to the results reported by LHCb [44]. Agreement within 1.5σ is observed between the two measurements for all observables, magnitudes, and phases.

Table 7: Results for the parameters of the two-particle and nonresonant nonlocal contributions for the (left) real and (right) imaginary components as defined in Eqs. 28 and Sec. 2.5.3. The first uncertainty is statistical, while the second is systematic.

Nonlocal parameter results			
$\Re(A^{\parallel}_{D^0\bar{D}^0})$	$-0.07 \pm 0.93 \pm 0.69$	$\Im(A^{\parallel}_{D^0\bar{D}^0})$	$-0.44 \pm 0.71 \pm 0.73$
$\Re(A^{\perp}_{D^0\bar{D}^0})$	$-0.12 \pm 0.83 \pm 0.71$	$\Im(A^{\perp}_{D^0\bar{D}^0})$	$0.02 \pm 0.80 \pm 0.74$
$\Re(A^{0}_{D^0\bar{D}^0})$	$-0.33 \pm 0.91 \pm 0.70$	$\Im(A^{0}_{D^0\bar{D}^0})$	$-0.27 \pm 0.77 \pm 0.81$
$\Re(A^{\parallel}_{D^{*0}\bar{D}^{*0}})$	$-0.06 \pm 0.96 \pm 0.63$	$\Im(A^{\parallel}_{D^{*0}\bar{D}^{*0}})$	$-0.25 \pm 0.79 \pm 0.67$
$\Re(A^{\perp}_{D^{*0}\bar{D}^{*0}})$	$-0.16 \pm 0.91 \pm 0.66$	$\Im(A^{\perp}_{D^{*0}\bar{D}^{*0}})$	$-0.03 \pm 0.85 \pm 0.70$
$\Re(A^{0}_{D^{*0}\bar{D}^{*0}})$	$-0.17 \pm 0.95 \pm 0.66$	$\Im(A^{0}_{D^{*0}\bar{D}^{*0}})$	$-0.28 \pm 0.85 \pm 0.78$
$\Re(A^{\parallel}_{D^{*0}\bar{D}^{0}})$	$0.02 \pm 0.42 \pm 0.66$	$\Im(A^{\parallel}_{D^{*0}\bar{D}^{0}})$	$-0.46 \pm 0.32 \pm 0.58$
$\Re(A^{\perp}_{D^{*0}\bar{D}^{0}})$	$-0.24 \pm 0.42 \pm 0.70$	$\Im(A^{\perp}_{D^{*0}\bar{D}^{0}})$	$-0.11 \pm 0.39 \pm 0.61$
$\Re(A^{0}_{D^{*0}\bar{D}^{0}})$	$-0.51 \pm 0.41 \pm 0.68$	$\Im(A^{0}_{D^{*0}\bar{D}^{0}})$	$0.12 \pm 0.35 \pm 0.58$
$\Re(\Delta\mathcal{C}_7^{\parallel})$	$0.00 \pm 0.03 \pm 0.02$	$\Im(\Delta\mathcal{C}_7^{\parallel})$	$-0.10 \pm 0.03 \pm 0.01$
$\Re(\Delta\mathcal{C}_7^{\perp})$	$-0.05 \pm 0.03 \pm 0.02$	$\Im(\Delta\mathcal{C}_7^{\perp})$	$-0.04 \pm 0.04 \pm 0.01$
$\Re(\Delta\mathcal{C}_7^{0})$	$0.33 \pm 0.33 \pm 0.09$	$\Im(\Delta\mathcal{C}_7^{0})$	$-0.19 \pm 0.20 \pm 0.09$

The measured magnitudes and phases of $B^0 \to J/\psi K^{*0}$ and $B^0 \to \psi(2S)K^{*0}$ transitions are also in good agreement with previous amplitude analyses performed by Belle [46, 71], once the systematic uncertainties due to the presence of $Z(4430)$ and $Z(4200)$ states are accounted for.

In order to check that the model used in this analysis is complete regarding its description of the nonlocal contributions, an alternative fit is performed in which the values of coefficients $\mathcal{C}_9$ and $\mathcal{C}_{10}$ are allowed to carry a linear dependence on q^2. Specifically, the following replacements are made,

$$\mathcal{C}_9^{q^2} = \mathcal{C}_9 + \alpha(q^2 - q^2_{\mathrm{mid}}), \qquad\qquad \mathcal{C}_{10}^{q^2} = \mathcal{C}_{10} + \beta(q^2 - q^2_{\mathrm{mid}}), \qquad (38)$$

where $q^2_{\mathrm{mid}} = 8.95$ GeV$^2/c^4$ and denotes the middle of the fitted q^2 range. Statistically significant nonzero values of α and/or β would imply an incorrect description of the nonlocal contributions since a q^2 dependent shift is not consistent with being of local origin. Allowing for this linear dependence in the fit does not significantly alter the values for $\mathcal{C}_9$ and $\mathcal{C}_{10}$, and results in $\alpha = 0.029 \pm 0.082$, $\beta = -0.058 \pm 0.026$, where the uncertainties are statistical only. No evidence for an incorrect description of the nonlocal contributions to the $\mathcal{C}_9$ parameter is observed, while for the parameter $\mathcal{C}_{10}$, which receives only local contributions in the model, a 2.2σ deviation from zero is observed in the β slope parameter. This could point to an inconsistency in form factors between the low and high q^2 regions but this is not explored and no systematic uncertainty is assigned due to this effect.

The results of the fit are also cross-checked for different choices of the dispersion relation subtraction point q^2_0 which serves as additional validation of the nonlocal model. The subtraction constant $Y_{c\bar{c}}(q^2_0)$ enters Eq. 19 as a constant offset to $\mathcal{C}_9$ and is degenerate with a NP contribution. In principle, the dispersion relation of Eq. 19 is exact and should be independent of the number and location of subtractions, provided the subtraction point is within the region in which $Y_{c\bar{c}}(q^2_0)$ can be calculated reliably, *i.e.* $q^2_0 < 0$. A deviation from this behaviour would reveal itself as a change in the $\mathcal{C}_9$ fit results dependent upon

Table 8: Results for the local form factors. The first uncertainty is statistical, while the second is systematic. The dashed entries represent the parameters being fixed in the fit due to their degeneracy with the nonlocal $\Delta C_7^{\perp,0}$ parameters.

Local form-factor results		
Parameter	Prior [34]	Posterior
$\alpha_1^{A_0}$	-1.12 ± 0.20	$-1.21 \pm 0.19 \pm 0.02$
$\alpha_2^{A_0}$	2.18 ± 1.76	$3.23 \pm 1.69 \pm 0.18$
$\alpha_0^{A_1}$	0.29 ± 0.02	$0.29 \pm 0.01 \pm 0.00$
$\alpha_1^{A_1}$	0.46 ± 0.13	$0.40 \pm 0.10 \pm 0.01$
$\alpha_2^{A_1}$	1.22 ± 0.73	$1.21 \pm 0.69 \pm 0.10$
$\alpha_0^{A_{12}}$	0.28 ± 0.02	$0.26 \pm 0.02 \pm 0.00$
$\alpha_1^{A_{12}}$	0.55 ± 0.34	$0.47 \pm 0.22 \pm 0.04$
$\alpha_2^{A_{12}}$	0.58 ± 2.08	$0.53 \pm 1.26 \pm 0.17$
α_0^{V}	0.36 ± 0.03	$0.36 \pm 0.02 \pm 0.00$
α_1^{V}	-1.09 ± 0.17	$-1.09 \pm 0.17 \pm 0.01$
α_2^{V}	2.73 ± 1.99	$3.93 \pm 1.74 \pm 0.25$
$\alpha_1^{T_1}$	-0.95 ± 0.14	$-0.94 \pm 0.14 \pm 0.01$
$\alpha_2^{T_1}$	2.11 ± 1.28	$2.07 \pm 1.16 \pm 0.05$
$\alpha_0^{T_2}$	0.32 ± 0.02	$-$
$\alpha_1^{T_2}$	0.60 ± 0.18	$0.61 \pm 0.16 \pm 0.01$
$\alpha_2^{T_2}$	1.70 ± 0.99	$1.78 \pm 0.98 \pm 0.03$
$\alpha_0^{T_{23}}$	0.62 ± 0.03	$-$
$\alpha_1^{T_{23}}$	0.97 ± 0.32	$0.95 \pm 0.30 \pm 0.01$
$\alpha_2^{T_{23}}$	1.81 ± 2.45	$1.68 \pm 2.15 \pm 0.04$

the chosen subtraction point. This would indicate a problem in either the calculation of $Y_{c\bar{c}}(q_0^2)$ or in the extrapolation to physical q^2 values via the dispersive integral — that is, a problem with the parameterisation of the spectral densities used in this analysis. To check this, the fit is run twice with subtractions at $q_0^2 = -1\,\text{GeV}^2/c^4$ and $q_0^2 = -10\,\text{GeV}^2/c^4$ and the results are compared to the baseline fit with the subtraction at $q_0^2 = -4.6\,\text{GeV}^2/c^4$. The change in the $\mathcal{C}_9$ parameter is found to be ~ 0.1 in both cases which is approximately 35% of the statistical uncertainty. Therefore, within the precision of this measurement, the choice of subtraction point is found to have a negligible impact on the results.

To investigate the sensitivity of the fit to the local form factor constraints, an alternative set of SM predictions from Ref. [28] is used to constrain the form factors. The main difference between the two sets of form-factor predictions are the LCSR inputs, leading to slight differences in the central values and widths of the constraints in this alternative fit. Modifying the constraint results in a non-negligible shift in the Wilson Coefficients. The effect is approximately 35% of the statistical uncertainty for $\mathcal{C}_9$ and 90% for $\mathcal{C}_{10}$. This difference is visible due to the improved precision of the measurement presented here. Further advances in the calculation of the local form factors are necessary to resolve these differences. Plots of the baseline local form factors as a function of q^2 are shown in Fig. 8, where only the statistical uncertainty is shown. The statistical precision of the data provides some mild overconstraining power and in some cases prefers slightly modified central values; however the global difference between the prefit and postfit form
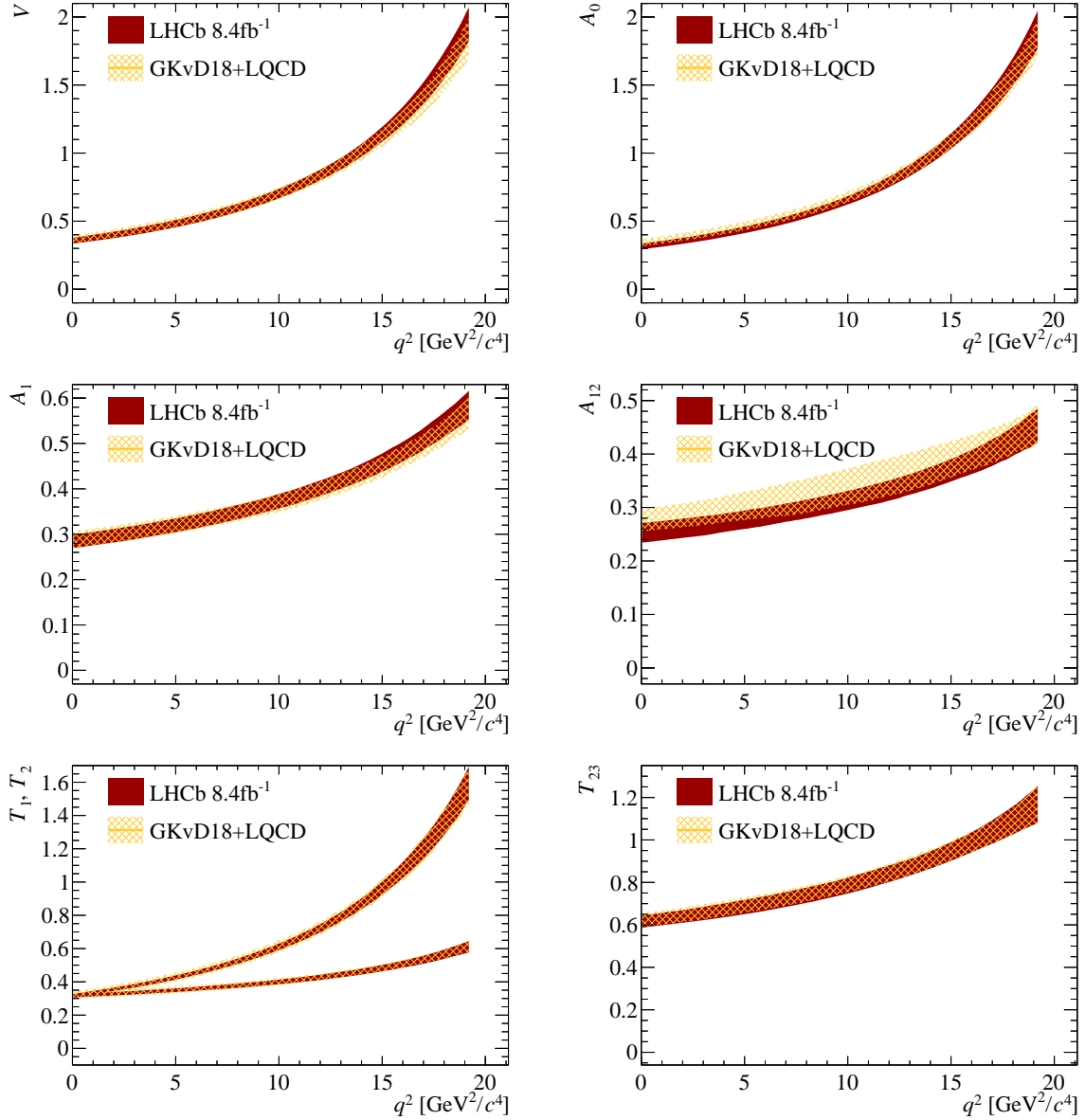
Figure 8: Comparison of form factors (orange) prefit and (maroon) postfit. The bands denote the 68% intervals from varying the postfit and prefit covariance matrices respectively. Only the statistical uncertainty is accounted for in the postfit intervals.

factors, evaluated using the change in χ^2 of the Gaussian constraint, is negligible.

The results of the nonlocal hadronic amplitudes, expressed as polarisation-dependent shifts to the $\mathcal{C}_9$ parameter are shown in Fig. 9. A comparison is made to the nonlocal amplitudes measured using $4.7\,\text{fb}^{-1}$ of LHCb data [36] that employed a polynomial expansion in the z parameter, defined similarly to that shown in Eq. 15 and relies on the analytical properties of these functions in the q^2 range $q^2 \in (1.1, 8.0) \cup (11.0, 12.5)\,\text{GeV}^2/c^4$. In the measurement of Ref. [36] two fits were considered. One fit that relied on a simultaneous fit to both LHCb data in the region and theory calculations at $q^2 < 0$ using an expansion up to fourth order in z, and another fit only toLHCb data using an expansion up to second order in z. In contrast to the study of Ref. [36], the model used
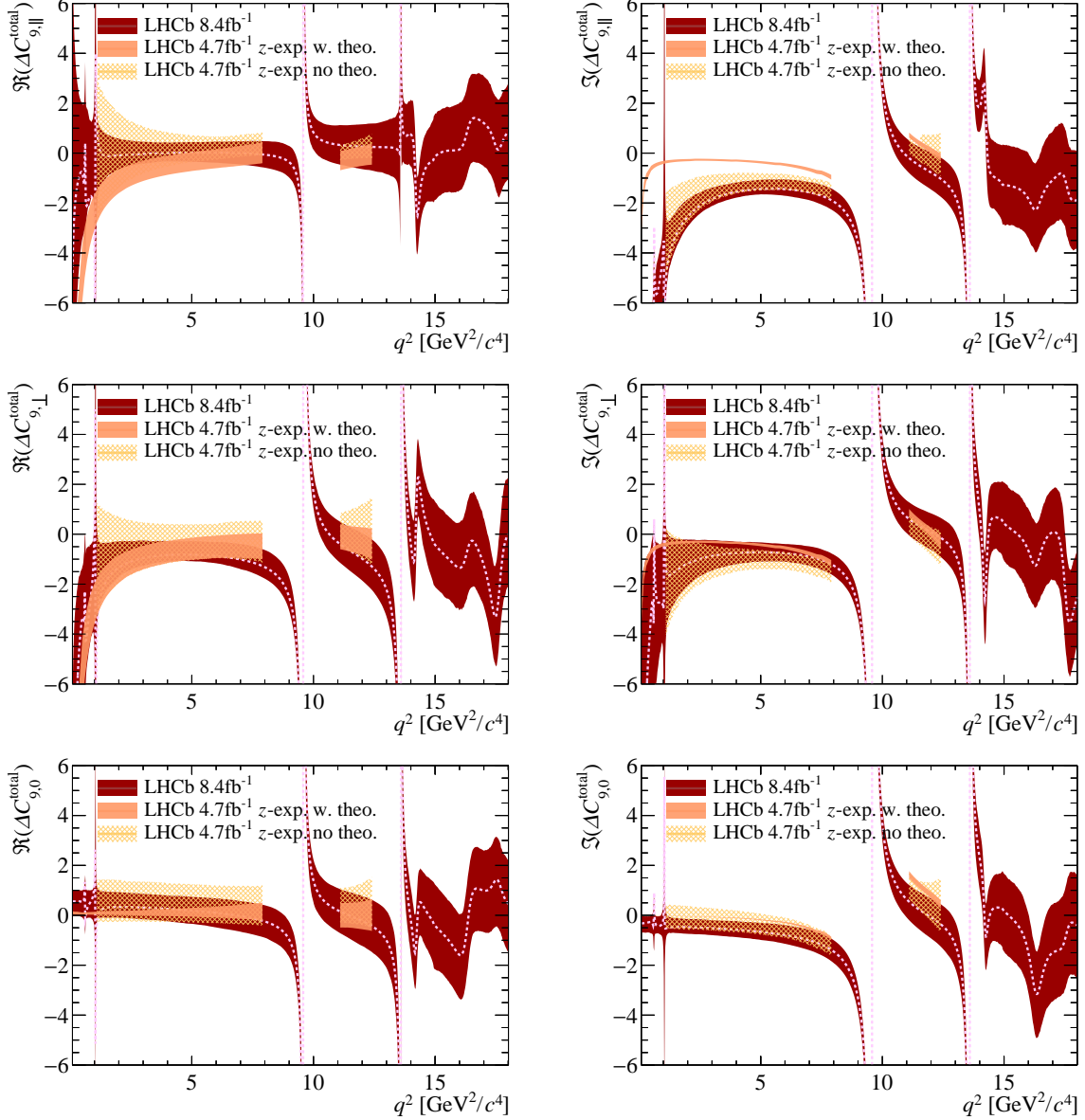
Figure 9: The nonlocal contributions from (maroon) this analysis that includes one- and two-particle hadronic amplitudes expressed as shifts to $\mathcal{C}_9$. The contributions from the ΔC_7^λ terms are also included, but the tau-loop contribution is excluded. The results of z-expansion fits [42] from the 4.7 fb^{-1} LHCb analysis [36] are also shown (pink) with and (yellow) without theory input from $q^2 < 0$. See text for more detail.

in this analysis gives access to the entire q^2 range of $B^0 \to K^{*0}\mu^+\mu^-$ decays. A good agreement is seen in the real part of nonlocal amplitudes between all three fit variations. However, it is clear that the data prefers large $\Im(\Delta C_{9,\parallel}^{\text{total}})$ contributions, that cannot be accommodated by the theory inputs at $q^2 < 0$ for the z-expansion fit.

Figures 10 and 11 show the role of the nonlocal contributions in the observable P_5' and the differential branching fraction, respectively. The nonlocal components are set to zero in the model when constructing the observables in order to plot only the local contributions, as shown in Fig. 10a for P_5' and Fig. 11a for the differential branching

fraction, $d\Gamma/dq^2$. The local-only observables evidently differ from the total across much of the q^2 spectrum, including within the bins used in previous analyses [74]. By setting the Wilson Coefficients to their SM values, SM "postdictions" of the angular observables can be computed from the signal parameters returned by the baseline fit to the data. The resulting observables are constructed using the nonlocal contributions derived from data from this analysis and can be compared to the formal SM predictions from Ref. [34], as shown in Figs. 10b and 11b. The SM observable postdictions of this analysis have central values closer to those of the data fit results for the total observables, indicating that the data prefer larger nonlocal contributions than the formal SM computations. This is in agreement with the distributions of the nonlocal amplitudes shown in Fig. 9. Nevertheless, the SM postdictions also have different central values to the baseline fit that are closer to the SM predictions. The latter observation indicates that the nonlocal contributions, while important, are not sufficient to explain the deviation seen in the measured value of $\mathcal{C}_9$.

Overall, this set of results is consistent with those reported in recent global analyses of $b \to s\ell^+\ell^-$ decays [24], which favour lepton flavour universal NP contributions to Wilson Coefficient $\mathcal{C}_9$. Moreover, they are consistent with the findings of other complementary analyses investigating the effect of the nonlocal contributions in $B^0 \to K^*\ell^+\ell^-$ decays [6,75] which also found them to be of only minor importance.

(a)

(b)
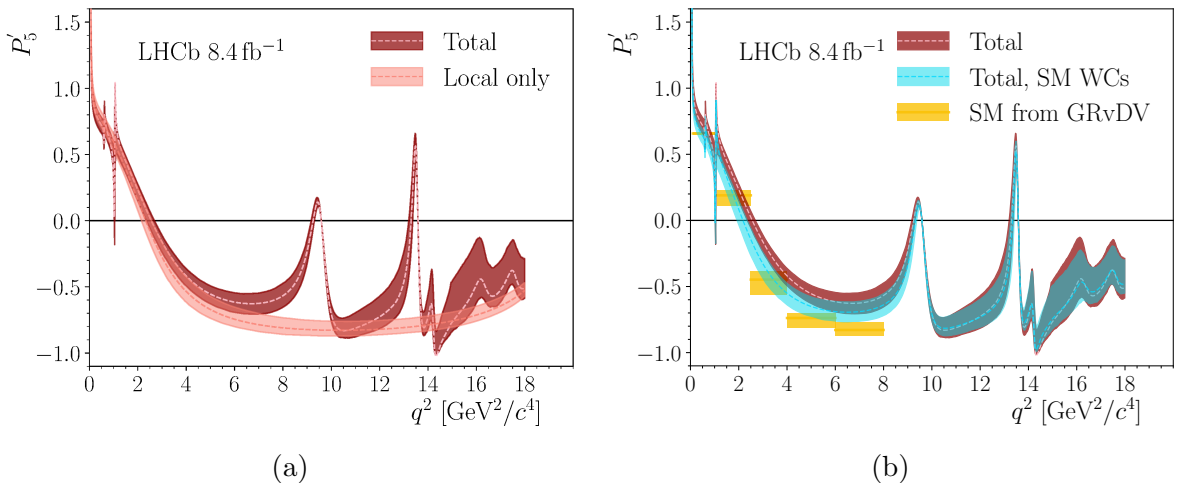
Figure 10: Distributions of the observable P_5' constructed out of the signal parameters from the baseline fit to data. In (a) the distribution is shown both with and without the nonlocal contributions included in the amplitudes. In (b) the distribution is shown for the baseline fit to data, and with the Wilson Coefficients (WCs) set to their SM values. These are compared against SM predictions obtained from Ref. [34].

34
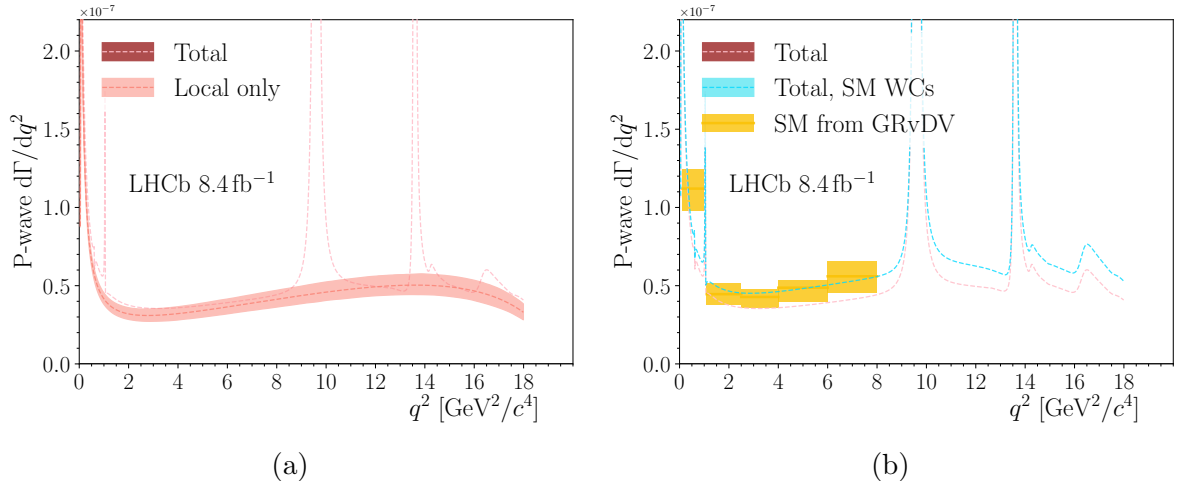
Figure 11: Distributions of the P-wave differential branching fraction $\mathrm{d}\Gamma/\mathrm{d}q^2$ constructed out of the signal parameters from the baseline fit to data. In (a) the distribution is shown both with and without the nonlocal contributions included in the amplitudes. In (b) the distribution is shown for the baseline fit to data, and with the Wilson Coefficients (WCs) set to their SM values. These are compared against SM predictions obtained from Ref. [34].

8 Conclusion

An amplitude analysis of the decay $B^0 \to K^{*0}\mu^+\mu^-$ in the reconstructed q^2 range of $0.1 \leq q^2 \leq 18.0\,\mathrm{GeV}^2/c^4$ is performed for the first time using LHCb data. The analysis employs a model of one- and two-particle nonlocal amplitudes to explicitly isolate the local and nonlocal contributions to the decay and capture the interference between them. In doing so, direct measurements of the $b \to s\mu^+\mu^-$ Wilson Coefficients $\mathcal{C}_{9,10}^{(')}$ are obtained, as well as a first ever direct measurement of the Wilson Coefficient $\mathcal{C}_{9\tau}$. The values of $\mathcal{C}_9'$, $\mathcal{C}_{10}$, $\mathcal{C}_{10}'$, and $\mathcal{C}_{9\tau}$ are all found to be consistent with the SM, while a 2.1σ deviation is observed in the $\mathcal{C}_9$ parameter. The observed shift in the value of $\mathcal{C}_9$ is found to be independent of q^2, but has a slight dependence on the local form factor constraints used. These results agree with the interpretations of previous binned angular analyses. Although the nonlocal contributions play a clear role in the angular distribution of $B^0 \to K^{*0}\mu^+\mu^-$ decays, the tension in the measured value of $\mathcal{C}_9$ persists. There is also agreement with the findings of the prior complementary analysis focusing on the effect of the nonlocal contributions in $B^0 \to K^{*0}\ell^+\ell^-$ decays. The results of this analysis are obtained using all available information in the final state and cannot be combined with any other LHCb measurement of the angular observables or the branching fraction of the same or partially the same dataset.

Acknowledgements

Appendices

A   Angular observables and spherical harmonics

For a P-wave $K^+\pi^-$ system, the explicit forms of the angular terms in Eq.(4) are given by

$$
\begin{aligned}
f_{1s}(\cos\theta_\ell, \cos\theta_K, \phi) &= \sin^2\theta_K, \\
f_{1c}(\cos\theta_\ell, \cos\theta_K, \phi) &= \cos^2\theta_K, \\
f_{2s}(\cos\theta_\ell, \cos\theta_K, \phi) &= \sin^2\theta_K \cos 2\theta_\ell, \\
f_{2c}(\cos\theta_\ell, \cos\theta_K, \phi) &= \cos^2\theta_K \cos 2\theta_\ell, \\
f_3(\cos\theta_\ell, \cos\theta_K, \phi) &= \sin^2\theta_K \sin^2\theta_\ell \cos 2\phi, \\
f_4(\cos\theta_\ell, \cos\theta_K, \phi) &= \sin 2\theta_K \sin 2\theta_\ell \cos\phi, \\
f_5(\cos\theta_\ell, \cos\theta_K, \phi) &= \sin 2\theta_K \sin\theta_\ell \cos\phi, \\
f_{6s}(\cos\theta_\ell, \cos\theta_K, \phi) &= \sin^2\theta_K \cos\theta_\ell, \\
f_7(\cos\theta_\ell, \cos\theta_K, \phi) &= \sin 2\theta_K \sin\theta_\ell \sin\phi, \\
f_8(\cos\theta_\ell, \cos\theta_K, \phi) &= \sin 2\theta_K \sin 2\theta_\ell \sin\phi, \\
f_9(\cos\theta_\ell, \cos\theta_K, \phi) &= \sin^2\theta_K \sin^2\theta_\ell \sin 2\phi.
\end{aligned}
\tag{39}
$$

and for the S-wave, they are given by

$$
\begin{aligned}
f_{1c}^{S'}(\cos\theta_\ell, \cos\theta_K, \phi) &= 1, \\
f_{2c}^{S'}(\cos\theta_\ell, \cos\theta_K, \phi) &= \cos 2\theta_\ell, \\
f_{1c}'(\cos\theta_\ell, \cos\theta_K, \phi) &= \cos\theta_K, \\
f_{2c}'(\cos\theta_\ell, \cos\theta_K, \phi) &= \cos\theta_K \cos 2\theta_\ell, \\
f_4'(\cos\theta_\ell, \cos\theta_K, \phi) &= \sin\theta_K \sin 2\theta_\ell \cos\phi, \\
f_5'(\cos\theta_\ell, \cos\theta_K, \phi) &= \sin\theta_K \sin\theta_\ell \cos\phi, \\
f_7'(\cos\theta_\ell, \cos\theta_K, \phi) &= \sin\theta_K \sin\theta_\ell \sin\phi, \\
f_8'(\cos\theta_\ell, \cos\theta_K, \phi) &= \sin\theta_K \sin 2\theta_\ell \sin\phi.
\end{aligned}
\tag{40}
$$

The corresponding angular coefficients $J_i(q^2)$ can be constructed using the transversity amplitudes $\mathcal{A}_0^{L,R}$, $\mathcal{A}_\parallel^{L,R}$, $\mathcal{A}_\perp^{L,R}$ and $\mathcal{A}_t$ described in Sec. 2.3, where contributions from scalar amplitudes are assumed to be zero. The explicit forms of the P-wave angular coefficients

are given by

$$J_{1s}(q^2) = \frac{2+\beta_\ell^2}{4}\left(|\mathcal{A}_\perp^L|^2 + |\mathcal{A}_\parallel^L|^2 + |\mathcal{A}_\perp^R|^2 + |\mathcal{A}_\parallel^R|^2\right) + \frac{4m_\ell^2}{q^2}\operatorname{Re}\left(\mathcal{A}_\perp^L\mathcal{A}_\perp^{R*} + \mathcal{A}_\parallel^L\mathcal{A}_\parallel^{R*}\right),$$

$$J_{1c}(q^2) = |\mathcal{A}_0^L|^2 + |\mathcal{A}_0^R|^2 + \frac{4m_\ell^2}{q^2}\left(|\mathcal{A}_t|^2 + 2\operatorname{Re}\left(\mathcal{A}_0^L\mathcal{A}_0^{R*}\right)\right),$$

$$J_{2s}(q^2) = \frac{\beta_\ell^2}{4}\left(|\mathcal{A}_\perp^L|^2 + |\mathcal{A}_\parallel^L|^2 + |\mathcal{A}_\perp^R|^2 + |\mathcal{A}_\parallel^R|^2\right),$$

$$J_{2c}(q^2) = -\beta_\ell^2\left(|\mathcal{A}_0^L|^2 + |\mathcal{A}_0^R|^2\right),$$

$$J_3(q^2) = \frac{\beta_\ell^2}{2}\left(|\mathcal{A}_\perp^L|^2 - |\mathcal{A}_\parallel^L|^2 + |\mathcal{A}_\perp^R|^2 - |\mathcal{A}_\parallel^R|^2\right),$$

$$J_4(q^2) = -\frac{\beta_\ell^2}{\sqrt{2}}\operatorname{Re}\left(\mathcal{A}_0^L\mathcal{A}_\parallel^{L*} + \mathcal{A}_0^R\mathcal{A}_\parallel^{R*}\right),$$

$$J_5(q^2) = \sqrt{2}\beta_\ell\operatorname{Re}\left(\mathcal{A}_0^L\mathcal{A}_\perp^{L*} - \mathcal{A}_0^R\mathcal{A}_\perp^{R*}\right),$$

$$J_{6s}(q^2) = -2\beta_\ell\operatorname{Re}\left(\mathcal{A}_\parallel^L\mathcal{A}_\perp^{L*} - \mathcal{A}_\parallel^R\mathcal{A}_\perp^{R*}\right),$$

$$J_7(q^2) = -\sqrt{2}\beta_\ell\operatorname{Im}\left(\mathcal{A}_0^L\mathcal{A}_\parallel^{L*} - \mathcal{A}_0^R\mathcal{A}_\parallel^{R*}\right),$$

$$J_8(q^2) = \frac{\beta_\ell^2}{\sqrt{2}}\operatorname{Im}\left(\mathcal{A}_0^L\mathcal{A}_\perp^{L*} + \mathcal{A}_0^R\mathcal{A}_\perp^{R*}\right),$$

$$J_9(q^2) = -\beta_\ell^2\operatorname{Im}\left(\mathcal{A}_\parallel^{L*}\mathcal{A}_\perp^L + \mathcal{A}_\parallel^{R*}\mathcal{A}_\perp^R\right),$$

$$(41)$$

where the parameter β_ℓ is given by $\beta_\ell = \sqrt{1 - \frac{4m_\ell^2}{q^2}}$. The S-wave angular coefficients also involve the S-wave transversity amplitude $\mathcal{A}_{00}^{L,R}$ in addition to the P-wave amplitudes, and are given by

$$J_{1c}^{S'}(q^2) = \frac{1}{3}\left(\left(|\mathcal{A}_{00}^L|^2 + |\mathcal{A}_{00}^R|^2\right) + \frac{4m_\ell^2}{q^2}2\operatorname{Re}(\mathcal{A}_{00}^L\mathcal{A}_{00}^{R*})\right),$$

$$J_{2c}^{S'}(q^2) = -\frac{1}{3}\beta_\ell^2\left(|\mathcal{A}_{00}^L|^2 + |\mathcal{A}_{00}^R|^2\right),$$

$$J_{1c}'(q^2) = \frac{2}{\sqrt{3}}\operatorname{Re}\left(\mathcal{A}_{00}^L\mathcal{A}_0^{L*} + \mathcal{A}_{00}^R\mathcal{A}_0^{R*} + \frac{4m_\ell^2}{q^2}\left(\mathcal{A}_{00}^L\mathcal{A}_0^{R*} + \mathcal{A}_0^L\mathcal{A}_{00}^{R*}\right)\right),$$

$$J_{2c}'(q^2) = -\frac{2}{\sqrt{3}}\beta_\ell^2\operatorname{Re}\left(\mathcal{A}_{00}^L\mathcal{A}_0^{L*} + \mathcal{A}_{00}^R\mathcal{A}_0^{R*}\right),$$

$$J_4'(q^2) = -\sqrt{\frac{2}{3}}\beta_\ell^2\left(\operatorname{Re}\left(\mathcal{A}_{00}^L\mathcal{A}_\parallel^{L*}\right) + \operatorname{Re}\left(\mathcal{A}_{00}^R\mathcal{A}_\parallel^{R*}\right)\right),$$

$$J_5'(q^2) = 2\sqrt{\frac{2}{3}}\beta_\ell^2\left(\operatorname{Re}\left(\mathcal{A}_{00}^L\mathcal{A}_\perp^{L*}\right) + \operatorname{Re}\left(\mathcal{A}_{00}^R\mathcal{A}_\perp^{R*}\right)\right),$$

$$J_7'(q^2) = -2\sqrt{\frac{2}{3}}\beta_\ell^2\left(\operatorname{Re}\left(\mathcal{A}_{00}^L\mathcal{A}_\parallel^{L*}\right) - \operatorname{Re}\left(\mathcal{A}_{00}^R\mathcal{A}_\parallel^{R*}\right)\right),$$

$$J_8'(q^2) = \sqrt{\frac{2}{3}}\beta_\ell^2\left(\operatorname{Re}\left(\mathcal{A}_{00}^L\mathcal{A}_\perp^{L*}\right) - \operatorname{Re}\left(\mathcal{A}_{00}^R\mathcal{A}_\perp^{R*}\right)\right).$$

$$(42)$$
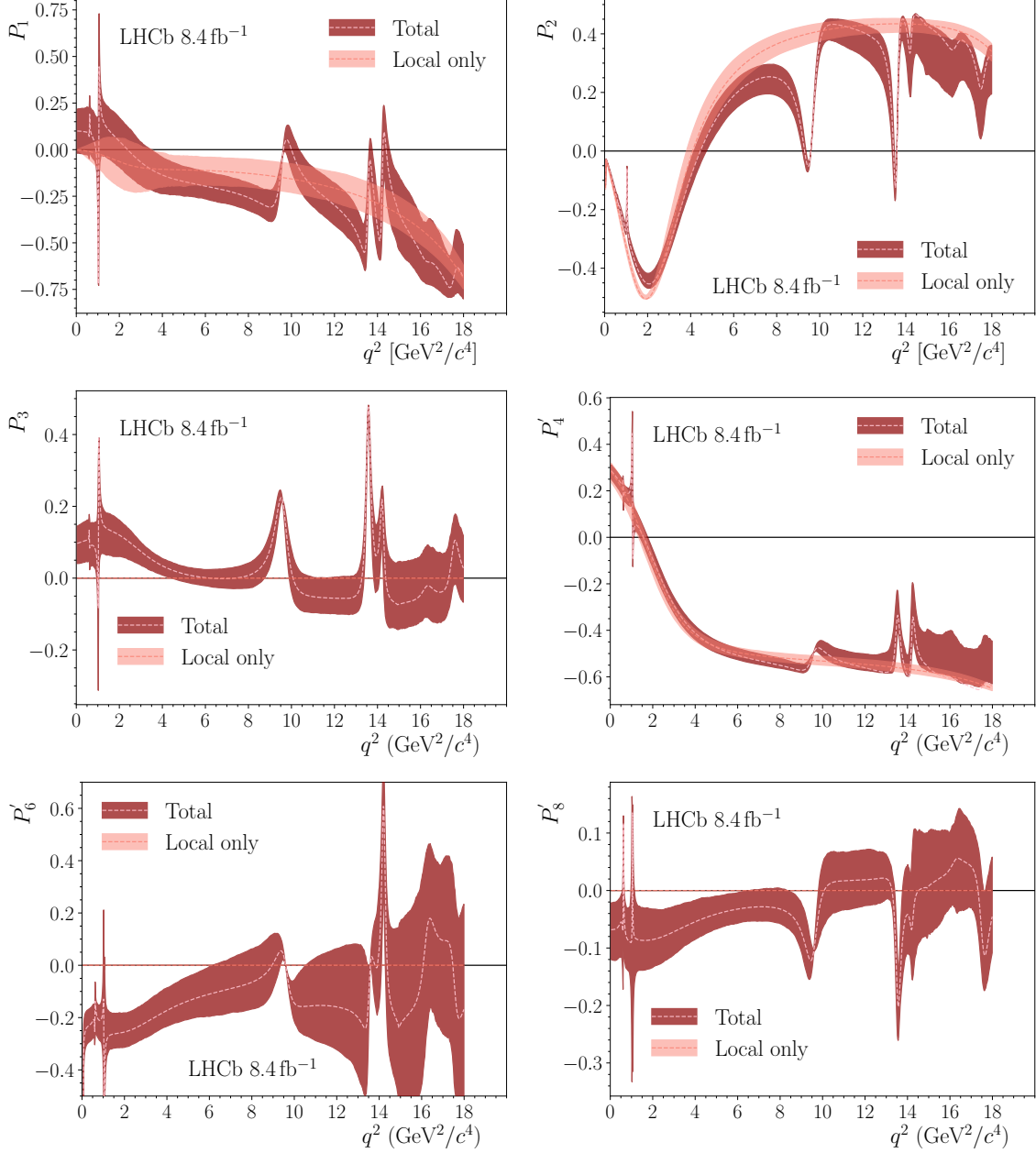
Figure 12: Plots of the angular observables in the optimised basis showing both the total and the contributions from local amplitudes only.

B   Plots of the full set of angular observables

As the overall fit calculates all amplitudes, the observables of previous measurements can be plotted for both the optimised (Fig. 12) and the standard (Fig. 13) basis. In all of the plots, the observables are shown when calculated from both the full amplitudes as well as from the local amplitudes only. In this way the contribution of the nonlocal amplitudes is made clear. Finally, in Fig. 14 there are plots in the standard basis compared against Standard Model predictions from Ref. [34].
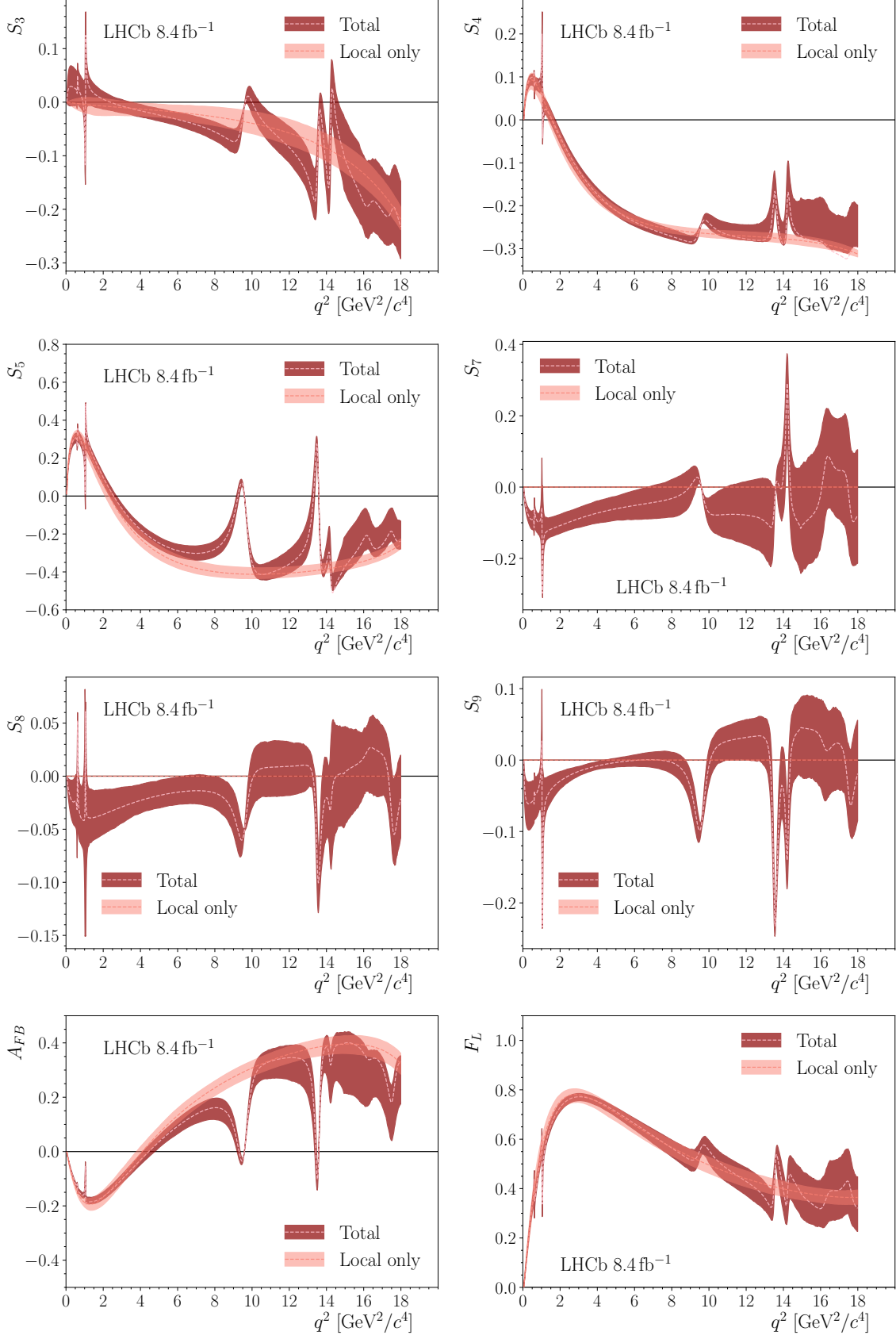
Figure 13: Plots of the angular observables in the standard basis showing both the total and the contributions from local amplitudes only.
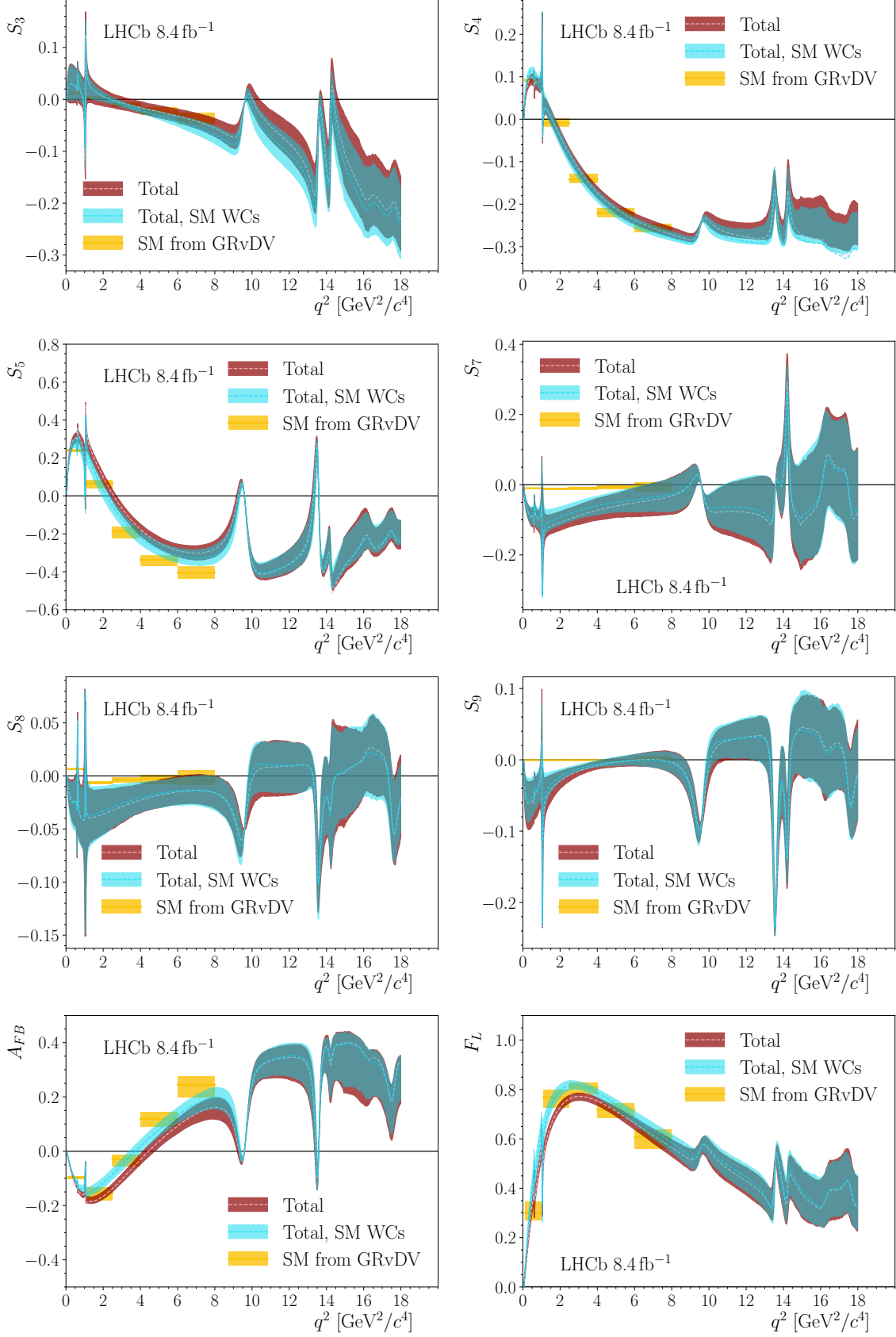
Figure 14: Plots of the unbinned angular observables in the standard basis shown for the both the baseline fit to data, and with the Wilson Coefficients (WCs) set to their Standard Model (SM) values. These are compared against SM predictions from Ref. [34].

C Fit projections in q^2 sub-regions

The four-dimensional maximum-likelihood fit to the signal region is performed simultaneously in three q^2 regions, as described in Sec. 3.3. The results of the fits to the $\cos\theta_K$, $\cos\theta_\ell$, ϕ, and q^2 distributions within each of the three regions are shown in Fig. 15.
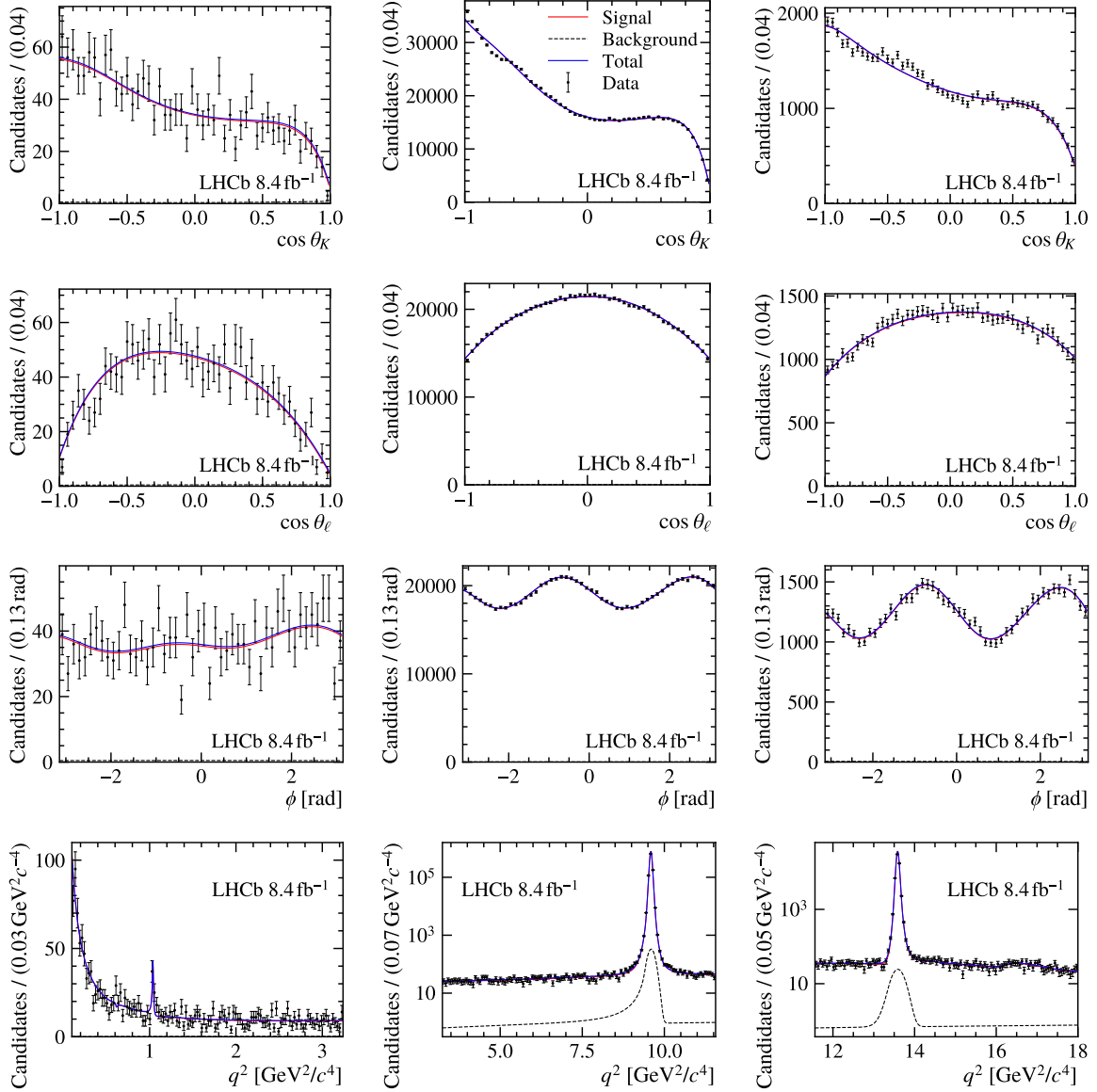
Figure 15: Result of the fit to candidates in the signal mass region. The four rows correspond to the distributions of $\cos\theta_K$, $\cos\theta_\ell$, ϕ and q^2. The three columns correspond to the low-, mid- and high-q^2 regions. The total PDF is shown in blue, the signal PDF in red and the background PDF in dotted black. The impact of the neglected exotic states is visible in the $\cos\theta_K$ distributions.

C.1 Projections of the q^2 spectrum with alternative signal decompositions

The signal contributions can be decomposed in various ways — for example, in terms of the local and nonlocal contributions, as done in Fig. 5 in the main text. Alternatively, they can be decomposed into contributions from different transversity amplitudes (see Sec. 2.3) as shown in Fig. 16, or into contributions from different Lorentz structures as shown in Fig. 17.
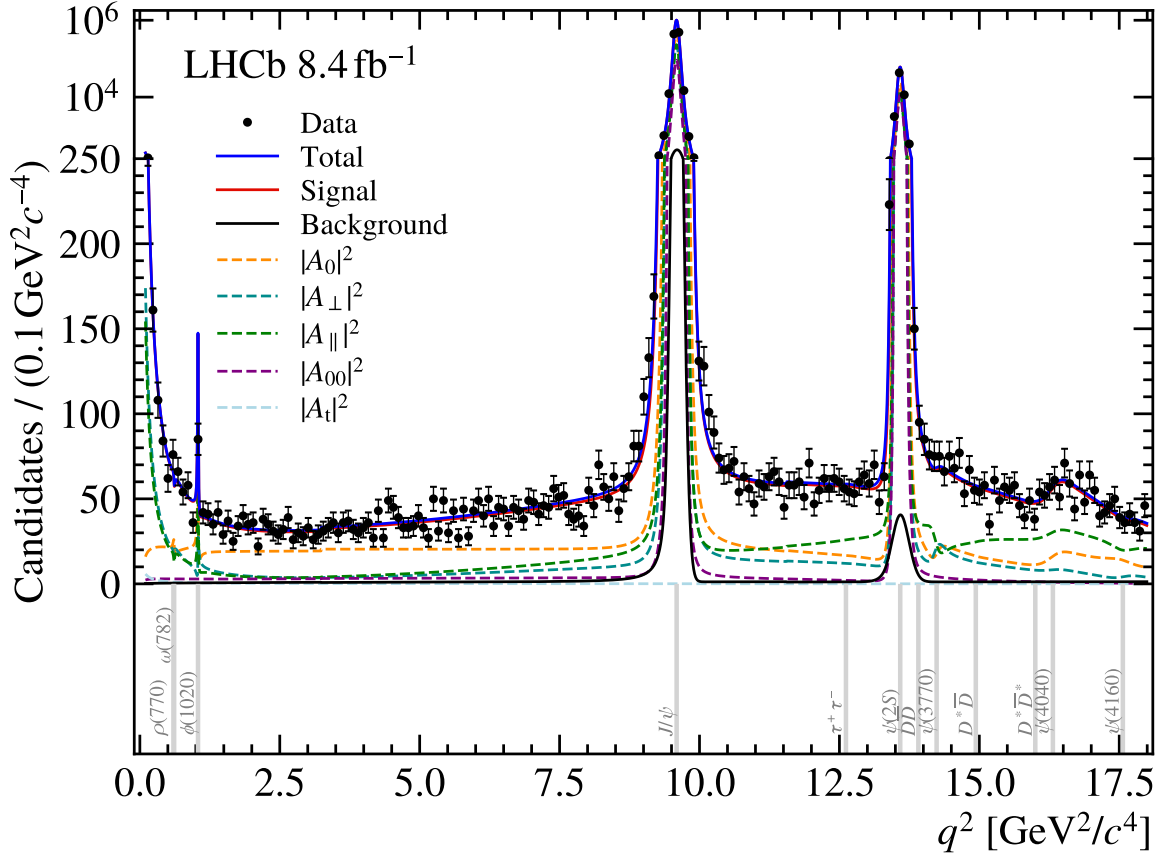
Figure 16: The q^2 distribution in the data, overlaid with the PDF projection from the baseline data fit. The total PDF is decomposed into signal and background components, with the signal contributions further decomposed into contributions from the different transversity amplitudes.

C.2 Comparison of observables to previous analyses

The total angular observables obtained from the signal parameters can be compared to previous LHCb measurements. The binned angular observables were measured in Ref. [5] using the Run 1 and 2016 data samples, corresponding to $4.7\,\text{fb}^{-1}$. The decay rate was measured in Ref. [76] using Run 1 data, corresponding to $3\,\text{fb}^{-1}$. The comparison is shown in Figs. 18 and 19.
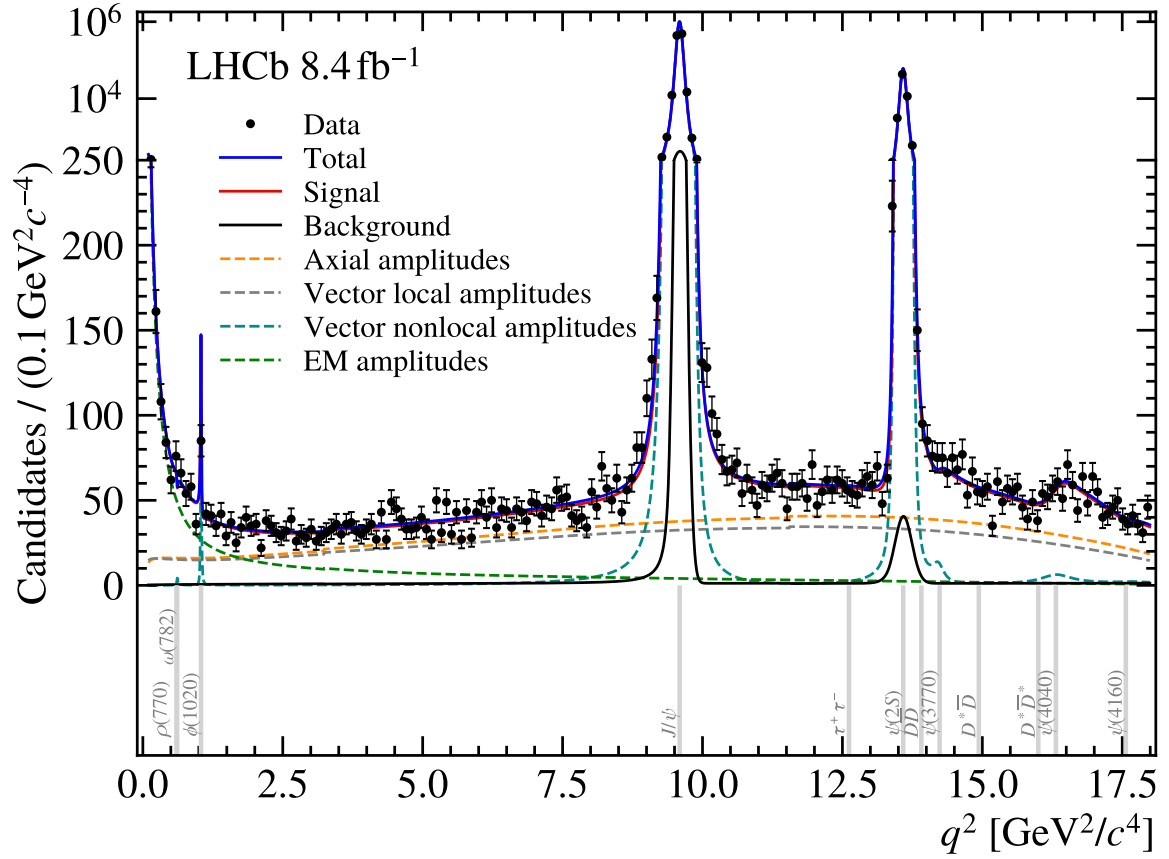
Figure 17: The q^2 distribution in the data, overlaid with the PDF projection from the baseline data fit. The total PDF is decomposed into signal and background components, with the signal contributions further decomposed into contributions from different Lorentz structures.

44
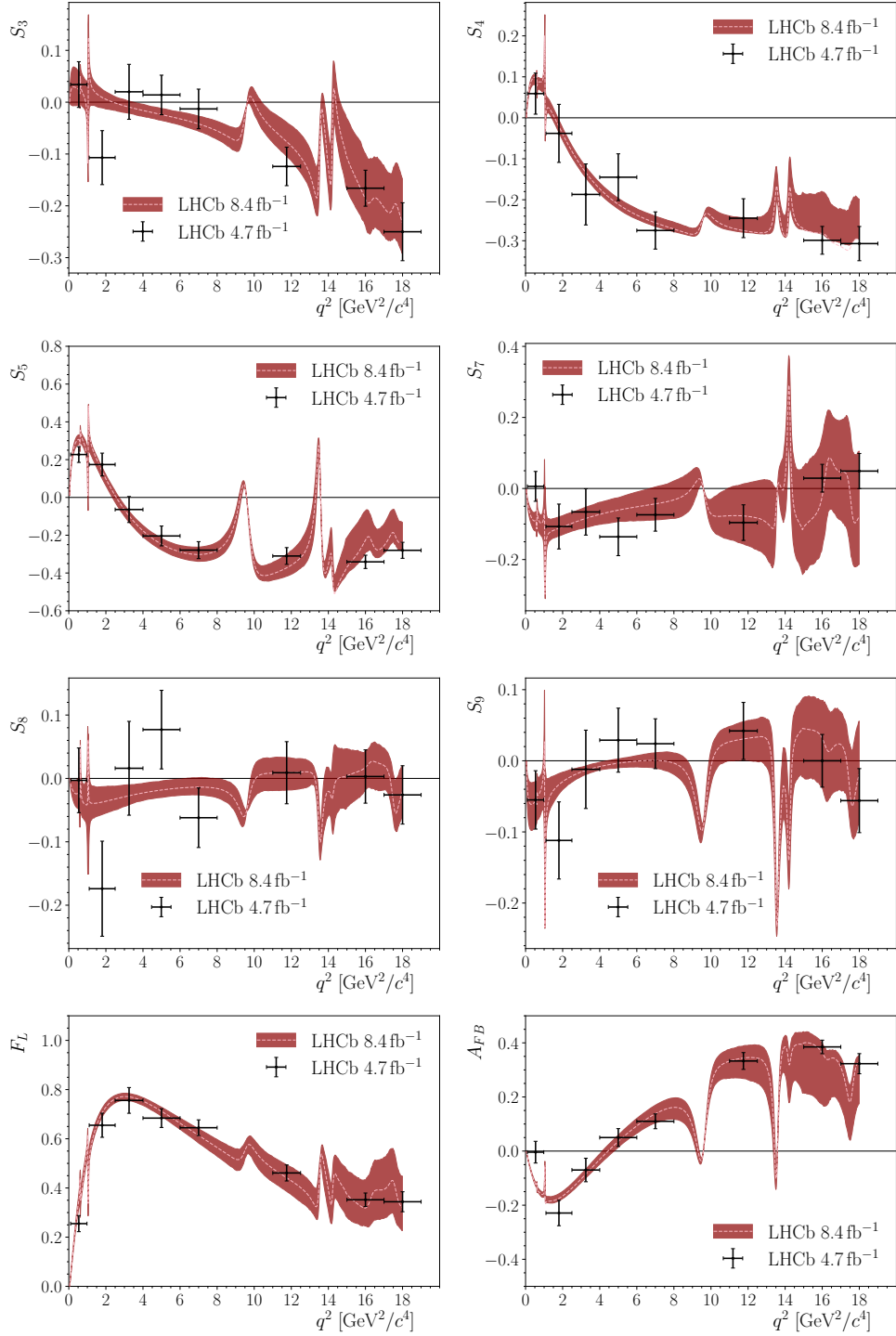
Figure 18: Comparison of unbinned observables constructed out of the signal parameters with the measurements from the dedicated LHCb binned analyses [5, 76] that used $4.7\,\mathrm{fb}^{-1}$ of data for the angular analysis (black).

45
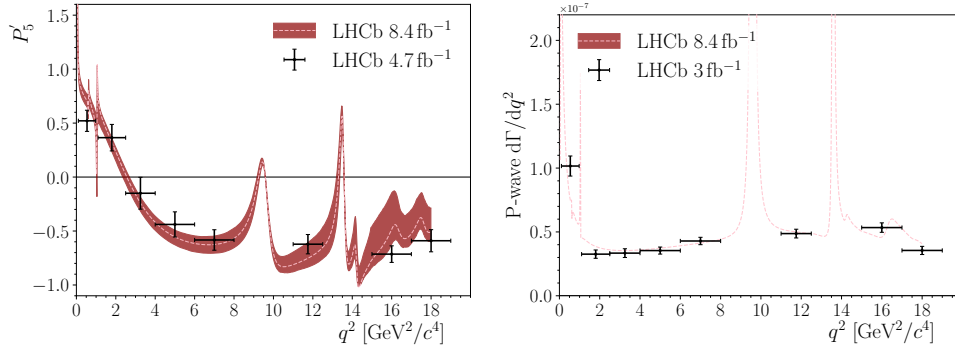
Figure 19: Comparison of unbinned observables constructed out of the signal parameters with the measurements from the dedicated LHCb binned analyses [5, 76] that used $4.7\,\mathrm{fb}^{-1}$ of data for the angular analysis and $3\,\mathrm{fb}^{-1}$ for the branching fraction (black).

References

[1] F. Kruger, L. M. Sehgal, N. Sinha, and R. Sinha, *Angular distribution and CP asymmetries in the decays $\bar{B} \to K^- \pi^+ e^- e^+$ and $\bar{B} \to \pi^- \pi^+ e^- e^+$*, Phys. Rev. D **61** (2000) 114028, arXiv:hep-ph/9907386, [Erratum: Phys. Rev. D 63, 019901 (2001)].

[2] LHCb collaboration, R. Aaij *et al.*, *Differential branching fraction and angular analysis of the decay $B^0 \to K^{*0} \mu^+ \mu^-$*, JHEP **08** (2013) 131, arXiv:1304.6325.

[3] LHCb collaboration, R. Aaij *et al.*, *Measurement of form-factor-independent observables in the decay $B^0 \to K^{*0} \mu^+ \mu^-$*, Phys. Rev. Lett. **111** (2013) 191801, arXiv:1308.1707.

[4] LHCb collaboration, R. Aaij *et al.*, *Angular analysis of the $B^0 \to K^{*0} \mu^+ \mu^-$ decay using $3\,fb^{-1}$ of integrated luminosity*, JHEP **02** (2016) 104, arXiv:1512.04442.

[5] LHCb collaboration, R. Aaij *et al.*, *Measurement of CP-averaged observables in the $B^0 \to K^{*0} \mu^+ \mu^-$ decay*, Phys. Rev. Lett. **125** (2020) 011802, arXiv:2003.04831.

[6] LHCb collaboration, R. Aaij *et al.*, *Amplitude analysis of the $B^0 \to K^{*0} \mu^+ \mu^-$ decay*, Phys. Rev. Lett. **132** (2024) 131801, arXiv:2312.09115.

[7] ATLAS collaboration, M. Aaboud *et al.*, *Angular analysis of $B^0_d \to K^* \mu^+ \mu^-$ decays in pp collisions at $\sqrt{s} = 8\ TeV$ with the ATLAS detector*, JHEP **10** (2018) 047, arXiv:1805.04000.

[8] BaBar collaboration, B. Aubert *et al.*, *Measurements of branching fractions, rate asymmetries, and angular distributions in the rare decays $B \to K \ell^+ \ell^-$ and $B \to K^* \ell^+ \ell^-$*, Phys. Rev. **D73** (2006) 092001, arXiv:hep-ex/0604007.

[9] BaBar collaboration, J. P. Lees *et al.*, *Measurement of angular asymmetries in the decays $B \to K^* \ell^+ \ell^-$*, Phys. Rev. **D93** (2016) 052015, arXiv:1508.07960.

[10] Belle collaboration, J.-T. Wei *et al.*, *Measurement of the differential branching fraction and forward-backward asymmetry for $B \to K^{(*)} \ell^+ \ell^-$*, Phys. Rev. Lett. **103** (2009) 171801, arXiv:0904.0770.

[11] Belle collaboration, S. Wehle *et al.*, *Lepton-flavor-dependent angular analysis of $B \to K^* \ell^+ \ell^-$*, Phys. Rev. Lett. **118** (2017) 111801, arXiv:1612.05014.

[12] CDF collaboration, T. Aaltonen *et al.*, *Measurements of the angular distributions in the decays $B \to K^{(*)} \mu^+ \mu^-$ at CDF*, Phys. Rev. Lett. **108** (2012) 081807, arXiv:1108.0695.

[13] CMS collaboration, V. Khachatryan *et al.*, *Angular analysis of the decay $B^0 \to K^{*0} \mu^+ \mu^-$ from pp collisions at $\sqrt{s} = 8\ TeV$*, Phys. Lett. **B753** (2016) 424, arXiv:1507.08126.

[14] CMS collaboration, A. M. Sirunyan *et al.*, *Measurement of angular parameters from the decay $B^0 \to K^{*0} \mu^+ \mu^-$ in proton-proton collisions at $\sqrt{s} = 8\ TeV$*, Phys. Lett. **B781** (2018) 517, arXiv:1710.02846.

[15] W. Altmannshofer *et al.*, *Symmetries and asymmetries of $B \to K^* \mu^+ \mu^-$ decays in the Standard Model and beyond*, JHEP **01** (2009) 019, `arXiv:0811.1214`.

[16] EOS collaboration, D. van Dyk *et al.*, *EOS: a software for flavor physics phenomenology*, Eur. Phys. J. **C82** (2022) 569, `arXiv:2111.15428`.

[17] D. van Dyk *et al.*, *eos/eos: EOS Version 1.0.11*, 2024. doi: 10.5281/zenodo.10600399.

[18] S. Descotes-Genon, J. Matias, M. Ramon, and J. Virto, *Implications from clean observables for the binned analysis of $B \to K^* \mu^+ \mu^-$ at large recoil*, JHEP **01** (2013) 048, `arXiv:1207.2753`.

[19] W. Altmannshofer and D. M. Straub, *New physics in $b \to s$ transitions after LHC run 1*, Eur. Phys. J. **C75** (2015) 382, `arXiv:1411.3161`.

[20] B. Capdevila *et al.*, *Patterns of New Physics in $b \to s\ell^+\ell^-$ transitions in the light of recent data*, JHEP **01** (2018) 093, `arXiv:1704.05340`.

[21] F. Beaujean, C. Bobeth, and D. van Dyk, *Comprehensive Bayesian analysis of rare (semi)leptonic and radiative B decays*, Eur. Phys. J. **C74** (2014) 2897, `arXiv:1310.2478`, [Erratum: Eur. Phys. J. C74, 3179 (2014)].

[22] S. Descotes-Genon, J. Matias, and J. Virto, *Understanding the $B \to K^* \mu^+ \mu^-$ anomaly*, Phys. Rev. **D88** (2013) 074002, `arXiv:1307.5683`.

[23] M. Algueró *et al.*, *$b \to s\ell^+\ell^-$ global fits after R_{K_S} and $R_{K^{*+}}$*, Eur. Phys. J. **C82** (2022) 326, `arXiv:2104.08921`.

[24] M. Algueró *et al.*, *To (b)e or not to (b)e: no electrons at LHCb*, Eur. Phys. J. **C83** (2023) 648, `arXiv:2304.07330`.

[25] D. London and J. Matias, *B flavour anomalies: 2021 theoretical status report*, Ann. Rev. Nucl. Part. Sci. **72** (2022) 37, `arXiv:2110.13270`.

[26] R. R. Horgan, Z. Liu, S. Meinel, and M. Wingate, *Lattice QCD calculation of form factors describing the rare decays $B \to K^*\ell^+\ell^-$ and $B_s \to \phi\ell^+\ell^-$*, Phys. Rev. **D89** (2014) 094501, `arXiv:1310.3722`.

[27] R. R. Horgan, Z. Liu, S. Meinel, and M. Wingate, *Rare B decays using lattice QCD form factors*, PoS **LATTICE2014** (2015) 372, `arXiv:1501.00367`.

[28] A. Bharucha, D. M. Straub, and R. Zwicky, *$B \to V\ell^+\ell^-$ in the Standard Model from light-cone sum rules*, JHEP **08** (2016) 098, `arXiv:1503.05534`.

[29] N. Gubernari, A. Kokulu, and D. van Dyk, *$B \to P$ and $B \to V$ form factors from B-Meson Light-Cone Sum Rules beyond leading twist*, JHEP **01** (2019) 150, `arXiv:1811.00983`.

[30] A. Khodjamirian, T. Mannel, A. A. Pivovarov, and Y.-M. Wang, *Charm-loop effect in $B \to K^{(*)}\ell^+\ell^-$ and $B \to K^*\gamma$*, JHEP **09** (2010) 089, `arXiv:1006.4945`.

[31] J. Lyon and R. Zwicky, *Resonances gone topsy turvy - the charm of QCD or new physics in $b \to s\ell^+\ell^-$?*, `arXiv:1406.0566`.

[32] M. Ciuchini *et al.*, *B → K*ℓ⁺ℓ⁻ decays at large recoil in the Standard Model: a theoretical reappraisal*, JHEP **06** (2016) 116, `arXiv:1512.07157`.

[33] N. Gubernari, D. van Dyk, and J. Virto, *Non-local matrix elements in $B_{(s)} → \{K^{(*)}, \phi\}\ell^+\ell^-$*, JHEP **02** (2021) 088, `arXiv:2011.09813`.

[34] N. Gubernari, M. Reboud, D. van Dyk, and J. Virto, *Improved theory predictions and global analysis of exclusive $b → s\mu^+\mu^-$ processes*, JHEP **09** (2022) 133, `arXiv:2206.03797`.

[35] T. Blake *et al.*, *An empirical model to determine the hadronic resonance contributions to $\overline{B}^0 → \overline{K}^{*0}\mu^+\mu^-$ transitions*, Eur. Phys. J. **C78** (2018) 453, `arXiv:1709.03921`.

[36] LHCb collaboration, R. Aaij *et al.*, *Determination of short- and long-distance contributions in $B^0 → K^{*0}\mu^+\mu^-$ decays*, Phys. Rev. **D109** (2024) 052009, `arXiv:2312.09102`.

[37] Particle Data Group, R. L. Workman *et al.*, *Review of particle physics*, Prog. Theor. Exp. Phys. **2022** (2022) 083C01.

[38] D. Becirevic and A. Tayduganov, *Impact of $B → K_0^*\ell^+\ell^-$ on the New Physics search in $B → K^*\ell^+\ell^-$ decay*, Nucl. Phys. **B868** (2013) 368, `arXiv:1207.4004`.

[39] M. Döring, U.-G. Meißner, and W. Wang, *Chiral dynamics and S-wave contributions in semileptonic B decays*, JHEP **10** (2013) 011, `arXiv:1307.0947`.

[40] S. Descotes-Genon, A. Khodjamirian, and J. Virto, *Light-cone sum rules for $B → K\pi$ form factors and applications to rare decays*, JHEP **12** (2019) 083, `arXiv:1908.02267`.

[41] A. Khodjamirian, T. Mannel, and Y. M. Wang, *$B → K\ell^+\ell^-$ decay at large hadronic recoil*, JHEP **02** (2013) 010, `arXiv:1211.0234`.

[42] C. Bobeth, M. Chrzaszcz, D. van Dyk, and J. Virto, *Long-distance effects in $B → K^*\ell\ell$ from analyticity*, Eur. Phys. J. **C78** (2018) 451, `arXiv:1707.07305`.

[43] C. Cornella *et al.*, *Hunting for $B^+ → K^+\tau^+\tau^-$ imprints on the $B^+ → K^+\mu^+\mu^-$ dimuon spectrum*, Eur. Phys. J. **C80** (2020) 1095, `arXiv:2001.04470`.

[44] LHCb collaboration, R. Aaij *et al.*, *Measurement of the polarization amplitudes in $B^0 → J/\psi K^*(892)^0$ decays*, Phys. Rev. **D88** (2013) 052002, `arXiv:1307.2782`.

[45] BaBar collaboration, B. Aubert *et al.*, *Measurement of decay amplitudes of $B → J/\psi K^*, \psi(2S)K^*$, and $\chi_{c1}K^*$ with an angular analysis*, Phys. Rev. **D76** (2007) 031102, `arXiv:0704.0522`.

[46] Belle collaboration, K. Chilikin *et al.*, *Observation of a new charged charmoniumlike state in $\bar{B}^0 → J/\psi K^-\pi^+$ decays*, Phys. Rev. **D90** (2014) 112009, `arXiv:1408.6457`.

[47] LHCb collaboration, R. Aaij *et al.*, *Study of the $B^0 → \rho(770)^0 K^*(892)^0$ decay with an amplitude analysis of $B^0 → (\pi^+\pi^-)(K^+\pi^-)$ decays*, JHEP **05** (2019) 026, `arXiv:1812.07008`.

[48] LHCb collaboration, R. Aaij *et al.*, *Measurement of polarization amplitudes and CP asymmetries in $B^0 → \phi K^*(892)^0$*, JHEP **05** (2014) 069, `arXiv:1403.2888`.

[49] LHCb collaboration, R. Aaij *et al.*, *Measurement of the phase difference between the short- and long-distance amplitudes in the* $B^+ \to K^+ \mu^+ \mu^-$ *decay*, Eur. Phys. J. **C77** (2017) 161, arXiv:1612.06764.

[50] H. M. Asatrian, C. Greub, and J. Virto, *Exact NLO matching and analyticity in* $b \to s\ell\ell$, JHEP **04** (2020) 012, arXiv:1912.09099.

[51] A. Paul and D. M. Straub, *Constraints on new physics from radiative B decays*, JHEP **04** (2017) 027, arXiv:1608.02556.

[52] LHCb collaboration, R. Aaij *et al.*, *Strong constraints on the* $b \to s\gamma$ *photon polarisation from* $B^0 \to K^{*0}e^+e^-$ *decays*, JHEP **12** (2020) 081, arXiv:2010.06011.

[53] LHCb collaboration, A. A. Alves Jr. *et al.*, *The LHCb detector at the LHC*, JINST **3** (2008) S08005.

[54] LHCb collaboration, R. Aaij *et al.*, *LHCb detector performance*, Int. J. Mod. Phys. **A30** (2015) 1530022, arXiv:1412.6352.

[55] R. Aaij *et al.*, *The LHCb trigger and its performance in 2011*, JINST **8** (2013) P04022, arXiv:1211.3055.

[56] R. Aaij *et al.*, *Design and performance of the LHCb trigger and full real-time reconstruction in Run 2 of the LHC*, JINST **14** (2019) P04013, arXiv:1812.10790.

[57] T. Sjöstrand, S. Mrenna, and P. Skands, *A brief introduction to PYTHIA 8.1*, Comput. Phys. Commun. **178** (2008) 852, arXiv:0710.3820.

[58] I. Belyaev *et al.*, *Handling of the generation of primary events in Gauss, the LHCb simulation framework*, J. Phys. Conf. Ser. **331** (2011) 032047.

[59] D. J. Lange, *The EvtGen particle decay simulation package*, Nucl. Instrum. Meth. **A462** (2001) 152.

[60] N. Davidson, T. Przedzinski, and Z. Was, *PHOTOS interface in C++: Technical and physics documentation*, Comp. Phys. Comm. **199** (2016) 86, arXiv:1011.0937.

[61] Geant4 collaboration, J. Allison *et al.*, *Geant4 developments and applications*, IEEE Trans. Nucl. Sci. **53** (2006) 270; Geant4 collaboration, S. Agostinelli *et al.*, *Geant4: A simulation toolkit*, Nucl. Instrum. Meth. **A506** (2003) 250.

[62] M. Clemencic *et al.*, *The LHCb simulation application, Gauss: Design, evolution and experience*, J. Phys. Conf. Ser. **331** (2011) 032023.

[63] D. Müller, M. Clemencic, G. Corti, and M. Gersabeck, *ReDecay: A novel approach to speed up the simulation at LHCb*, Eur. Phys. J. **C78** (2018) 1009, arXiv:1810.10362.

[64] L. Breiman, J. H. Friedman, R. A. Olshen, and C. J. Stone, *Classification and regression trees*, Wadsworth international group, Belmont, California, USA, 1984.

[65] Y. Freund and R. E. Schapire, *A decision-theoretic generalization of on-line learning and an application to boosting*, J. Comput. Syst. Sci. **55** (1997) 119.

[66] M. Pivk and F. R. Le Diberder, *sPlot: A statistical tool to unfold data distributions*, Nucl. Instrum. Meth. **A555** (2005) 356, `arXiv:physics/0402083`.

[67] T. Skwarnicki, *A study of the radiative cascade transitions between the Upsilon-prime and Upsilon resonances*, PhD thesis, Institute of Nuclear Physics, Krakow, 1986, DESY-F31-86-02.

[68] W. D. Hulsbergen, *Decay chain fitting with a Kalman filter*, Nucl. Instrum. Meth. **A552** (2005) 566, `arXiv:physics/0503191`.

[69] W. Weibull, *A statistical distribution function of wide applicability*, Journal of applied mechanics (1951).

[70] J. Gratrex, M. Hopfer, and R. Zwicky, *Generalised helicity formalism, higher moments and the $B \to K_{J_K}(\to K\pi)\bar{\ell}_1\ell_2$ angular distributions*, Phys. Rev. **D93** (2016) 054008, `arXiv:1506.03970`.

[71] Belle collaboration, K. Chilikin *et al.*, *Experimental constraints on the spin and parity of the $Z(4430)^+$*, Phys. Rev. **D88** (2013) 074026, `arXiv:1306.4894`.

[72] Belle collaboration, T. V. Dong *et al.*, *Search for the decay $B^0 \to K^{*0}\tau^+\tau^-$ at the Belle experiment*, Phys. Rev. **D108** (2023) L011102, `arXiv:2110.03871`.

[73] D. M. Straub, *flavio: a Python package for flavour and precision phenomenology in the Standard Model and beyond*, `arXiv:1810.08132`.

[74] L. Anderlini *et al.*, *Muon identification for LHCb Run 3*, JINST **15** (2020) T12005, `arXiv:2008.01579`.

[75] M. Bordone, G. Isidori, S. Mächler, and A. Tinari, *Short- vs. long-distance physics in $B \to K^{(*)}\ell^+\ell^-$: a data-driven analysis*, `arXiv:2401.18007`.

[76] LHCb collaboration, R. Aaij *et al.*, *Measurements of the S-wave fraction in $B^0 \to K^+\pi^-\mu^+\mu^-$ decays and the $B^0 \to K^*(892)^0\mu^+\mu^-$ differential branching fraction*, JHEP **11** (2016) 047, Erratum ibid. **04** (2017) 142, `arXiv:1606.04731`.
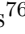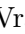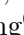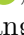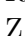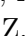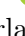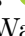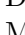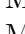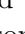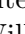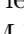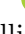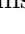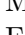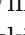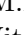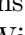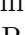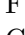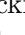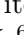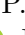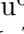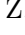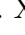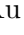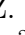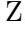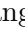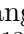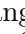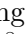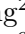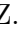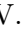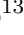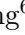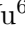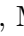
LHCb collaboration

R. Aaij[36] , A.S.W. Abdelmotteleb[55] , C. Abellan Beteta[49], F. Abudinén[55] ,

T. Ackernley[59] , A. A. Adefisoye[67] , B. Adeva[45] , M. Adinolfi[53] , P. Adlarson[79] ,

C. Agapopoulou[13] , C.A. Aidala[80] , Z. Ajaltouni[11], S. Akar[64] , K. Akiba[36] ,

P. Albicocco[26] , J. Albrecht[18] , F. Alessio[47] , M. Alexander[58] , Z. Aliouche[61] ,

P. Alvarez Cartelle[54] , R. Amalric[15] , S. Amato[3] , J.L. Amey[53] , Y. Amhis[13,47] ,

L. An[6] , L. Anderlini[25] , M. Andersson[49] , A. Andreianov[42] , P. Andreola[49] ,

M. Andreotti[24] , D. Andreou[67] , A. Anelli[29,p] , D. Ao[7] , F. Archilli[35,v] ,

M. Argenton[24] , S. Arguedas Cuendis[9] , A. Artamonov[42] , M. Artuso[67] ,

E. Aslanides[12] , R. Ataide Da Silva[48] , M. Atzeni[63] , B. Audurier[14] , D. Bacher[62] ,

I. Bachiller Perea[10] , S. Bachmann[20] , M. Bachmayer[48] , J.J. Back[55] ,

P. Baladron Rodriguez[45] , V. Balagura[14] , W. Baldini[24] , H. Bao[7] ,

J. Baptista de Souza Leite[59] , M. Barbetti[25,m] , I. R. Barbosa[68] , R.J. Barlow[61] ,

M. Barnyakov[23] , S. Barsuk[13] , W. Barter[57] , M. Bartolini[54] , J. Bartz[67] ,

J.M. Basels[16] , G. Bassi[33] , B. Batsukh[5] , A. Bay[48] , A. Beck[55] , M. Becker[18] ,

F. Bedeschi[33] , I.B. Bediaga[2] , S. Belin[45] , V. Bellee[49] , K. Belous[42] , I. Belov[27] ,

I. Belyaev[34] , G. Benane[12] , G. Bencivenni[26] , E. Ben-Haim[15] , A. Berezhnoy[42] ,

R. Bernet[49] , S. Bernet Andres[43] , A. Bertolin[31] , C. Betancourt[49] , F. Betti[57] , J.

Bex[54] , Ia. Bezshyiko[49] , J. Bhom[39] , M.S. Bieker[18] , N.V. Biesuz[24] , P. Billoir[15] ,

A. Biolchini[36] , M. Birch[60] , F.C.R. Bishop[10] , A. Bitadze[61] , A. Bizzeti , T. Blake[55] ,

F. Blanc[48] , J.E. Blank[18] , S. Blusk[67] , V. Bocharnikov[42] , J.A. Boelhauve[18] ,

O. Boente Garcia[14] , T. Boettcher[64] , A. Bohare[57] , A. Boldyrev[42] , C.S. Bolognani[76] ,

R. Bolzonella[24,l] , N. Bondar[42] , F. Borgato[31,q] , S. Borghi[61] , M. Borsato[29,p] ,

J.T. Borsuk[39] , S.A. Bouchiba[48] , T.J.V. Bowcock[59] , A. Boyer[47] , C. Bozzi[24] ,

A. Brea Rodriguez[48] , N. Breer[18] , J. Brodzicka[39] , A. Brossa Gonzalo[45] , J. Brown[59] ,

D. Brundu[30] , E. Buchanan[57] , A. Buonaura[49] , L. Buonincontri[31,q] , A.T. Burke[61] ,

C. Burr[47] , A. Butkevich[42] , J.S. Butter[54] , J. Buytaert[47] , W. Byczynski[47] ,

S. Cadeddu[30] , H. Cai[72], R. Calabrese[24,l] , S. Calderon Ramirez[9] , L. Calefice[44] ,

S. Cali[26] , M. Calvi[29,p] , M. Calvo Gomez[43] , P. Camargo Magalhaes[2,z] , J.

I. Cambon Bouzas[45] , P. Campana[26] , D.H. Campora Perez[76] ,

A.F. Campoverde Quezada[7] , S. Capelli[29] , L. Capriotti[24] , R. Caravaca-Mora[9] ,

A. Carbone[23,j] , L. Carcedo Salgado[45] , R. Cardinale[27,n] , A. Cardini[30] ,

P. Carniti[29,p] , L. Carus[20] , A. Casais Vidal[63] , R. Caspary[20] , G. Casse[59] ,

J. Castro Godinez[9] , M. Cattaneo[47] , G. Cavallero[24,47] , V. Cavallini[24,l] , S. Celani[20] ,

D. Cervenkov[62] , S. Cesare[28,o] , A.J. Chadwick[59] , I. Chahrour[80] , M. Charles[15] ,

Ph. Charpentier[47] , E. Chatzianagnostou[36] , C.A. Chavez Barajas[59] , M. Chefdeville[10] ,

C. Chen[12] , S. Chen[5] , Z. Chen[7] , A. Chernov[39] , S. Chernyshenko[51] ,

V. Chobanova[78] , S. Cholak[48] , M. Chrzaszcz[39] , A. Chubykin[42] , V. Chulikov[42] ,

P. Ciambrone[26] , X. Cid Vidal[45] , G. Ciezarek[47] , P. Cifra[47] , P.E.L. Clarke[57] ,

M. Clemencic[47] , H.V. Cliff[54] , J. Closier[47] , C. Cocha Toapaxi[20] , V. Coco[47] ,

J. Cogan[12] , E. Cogneras[11] , L. Cojocariu[41] , P. Collins[47] , T. Colombo[47] ,

A. Comerma-Montells[44] , L. Congedo[22] , A. Contu[30] , N. Cooke[58] , I. Corredoira [45] ,

A. Correia[15] , G. Corti[47] , J.J. Cottee Meldrum[53] , B. Couturier[47] , D.C. Craik[49] ,

M. Cruz Torres[2,g] , E. Curras Rivera[48] , R. Currie[57] , C.L. Da Silva[66] , S. Dadabaev[42] ,

L. Dai[69] , X. Dai[6] , E. Dall'Occo[18] , J. Dalseno[45] , C. D'Ambrosio[47] , J. Daniel[11] ,

A. Danilina[42] , P. d'Argent[22] , A. Davidson[55] , J.E. Davies[61] , A. Davis[61] ,

O. De Aguiar Francisco[61] , C. De Angelis[30,k] , F. De Benedetti[47] , J. de Boer[36] ,

K. De Bruyn[75] , S. De Capua[61] , M. De Cian[20,47] , U. De Freitas Carneiro Da Graca[2,b] ,

E. De Lucia[26] , J.M. De Miranda[2] , L. De Paula[3] , M. De Serio[22,h] , P. De Simone[26] ,

52

F. De Vellis[18] , J.A. de Vries[76] , F. Debernardis[22] , D. Decamp[10] , V. Dedu[12] ,
L. Del Buono[15] , B. Delaney[63] , H.-P. Dembinski[18] , J. Deng[8] , V. Denysenko[49] ,
O. Deschamps[11] , F. Dettori[30,k] , B. Dey[74] , P. Di Nezza[26] , I. Diachkov[42] ,
S. Didenko[42] , S. Ding[67] , L. Dittmann[20] , V. Dobishuk[51] , A. D. Docheva[58] ,
C. Dong[4] , A.M. Donohoe[21] , F. Dordei[30] , A.C. dos Reis[2] , A. D. Dowling[67] ,
W. Duan[70] , P. Duda[77] , M.W. Dudek[39] , L. Dufour[47] , V. Duk[32] , P. Durante[47] , M.
M. Duras[77] , J.M. Durham[66] , O. D. Durmus[74] , A. Dziurda[39] , A. Dzyuba[42] ,
S. Easo[56] , E. Eckstein[17] , U. Egede[1] , A. Egorychev[42] , V. Egorychev[42] ,
S. Eisenhardt[57] , E. Ejopu[61] , L. Eklund[79] , M. Elashri[64] , J. Ellbracht[18] , S. Ely[60] ,
A. Ene[41] , E. Epple[64] , J. Eschle[67] , S. Esen[20] , T. Evans[61] , F. Fabiano[30,k] ,
L.N. Falcao[2] , Y. Fan[7] , B. Fang[72] , L. Fantini[32,r,47] , M. Faria[48] , K. Farmer[57] ,
D. Fazzini[29,p] , L. Felkowski[77] , M. Feng[5,7] , M. Feo[18,47] , M. Fernandez Gomez[45] ,
A.D. Fernez[65] , F. Ferrari[23] , F. Ferreira Rodrigues[3] , M. Ferrillo[49] , M. Ferro-Luzzi[47] ,
S. Filippov[42] , R.A. Fini[22] , M. Fiorini[24,l] , K.M. Fischer[62] , D.S. Fitzgerald[80] ,
C. Fitzpatrick[61] , F. Fleuret[14] , M. Fontana[23] , L. F. Foreman[61] , R. Forty[47] ,
D. Foulds-Holt[54] , M. Franco Sevilla[65] , M. Frank[47] , E. Franzoso[24,l] , G. Frau[61] ,
C. Frei[47] , D.A. Friday[61] , J. Fu[7] , Q. Fuehring[18] , Y. Fujii[1] , T. Fulghesu[15] ,
E. Gabriel[36] , G. Galati[22] , M.D. Galati[36] , A. Gallas Torreira[45] , D. Galli[23,j] ,
S. Gambetta[57] , M. Gandelman[3] , P. Gandini[28] , B. Ganie[61] , H. Gao[7] , R. Gao[62] ,
Y. Gao[8] , Y. Gao[6] , Y. Gao[8] , M. Garau[30,k] , L.M. Garcia Martin[48] ,
P. Garcia Moreno[44] , J. García Pardiñas[47] , K. G. Garg[8] , L. Garrido[44] , C. Gaspar[47] ,
R.E. Geertsema[36] , L.L. Gerken[18] , E. Gersabeck[61] , M. Gersabeck[61] , T. Gershon[55] ,
Z. Ghorbanimoghaddam[53] , L. Giambastiani[31,q] , F. I. Giasemis[15,e] , V. Gibson[54] ,
H.K. Giemza[40] , A.L. Gilman[62] , M. Giovannetti[26] , A. Gioventù[44] ,
P. Gironella Gironell[44] , C. Giugliano[24,l] , M.A. Giza[39] , E.L. Gkougkousis[60] ,
F.C. Glaser[13,20] , V.V. Gligorov[15,47] , C. Göbel[68] , E. Golobardes[43] , D. Golubkov[42] ,
A. Golutvin[60,42,47] , A. Gomes[2,a,†] , S. Gomez Fernandez[44] , F. Goncalves Abrantes[62] ,
M. Goncerz[39] , G. Gong[4] , J. A. Gooding[18] , I.V. Gorelov[42] , C. Gotti[29] ,
J.P. Grabowski[17] , L.A. Granado Cardoso[47] , E. Graugés[44] , E. Graverini[48,t] ,
L. Grazette[55] , G. Graziani , A. T. Grecu[41] , L.M. Greeven[36] , N.A. Grieser[64] ,
L. Grillo[58] , S. Gromov[42] , C. Gu[14] , M. Guarise[24] , M. Guittiere[13] , V. Guliaeva[42] ,
P. A. Günther[20] , A.-K. Guseinov[48] , E. Gushchin[42] , Y. Guz[6,42,47] , T. Gys[47] ,
K. Habermann[17] , T. Hadavizadeh[1] , C. Hadjivasiliou[65] , G. Haefeli[48] , C. Haen[47] ,
J. Haimberger[47] , M. Hajheidari[47] , M.M. Halvorsen[47] , P.M. Hamilton[65] ,
J. Hammerich[59] , Q. Han[8] , X. Han[20] , S. Hansmann-Menzemer[20] , L. Hao[7] ,
N. Harnew[62] , M. Hartmann[13] , J. He[7,c] , M. Hecker[60] , F. Hemmer[47] ,
C. Henderson[64] , R.D.L. Henderson[1,55] , A.M. Hennequin[47] , K. Hennessy[59] ,
L. Henry[48] , J. Herd[60] , P. Herrero Gascon[20] , J. Heuel[16] , A. Hicheur[3] ,
G. Hijano Mendizabal[49] , D. Hill[48] , S.E. Hollitt[18] , J. Horswill[61] , R. Hou[8] , Y. Hou[11] ,
N. Howarth[59] , J. Hu[20] , J. Hu[70] , W. Hu[6] , X. Hu[4] , W. Huang[7] , W. Hulsbergen[36] ,
R.J. Hunter[55] , M. Hushchyn[42] , D. Hutchcroft[59] , D. Ilin[42] , P. Ilten[64] ,
A. Inglessi[42] , A. Iniukhin[42] , A. Ishteev[42] , K. Ivshin[42] , R. Jacobsson[47] , H. Jage[16] ,
S.J. Jaimes Elles[46,73] , S. Jakobsen[47] , E. Jans[36] , B.K. Jashal[46] , A. Jawahery[65,47] ,
V. Jevtic[18] , E. Jiang[65] , X. Jiang[5,7] , Y. Jiang[7] , Y. J. Jiang[6] , M. John[62] ,
D. Johnson[52] , C.R. Jones[54] , T.P. Jones[55] , S. Joshi[40] , B. Jost[47] , N. Jurik[47] ,
I. Juszczak[39] , D. Kaminaris[48] , S. Kandybei[50] , M. Kane[57] , Y. Kang[4] , C. Kar[11] ,
M. Karacson[47] , D. Karpenkov[42] , A. Kauniskangas[48] , J.W. Kautz[64] , F. Keizer[47] ,
M. Kenzie[54] , T. Ketel[36] , B. Khanji[67] , A. Kharisova[42] , S. Kholodenko[33,47] ,
G. Khreich[13] , T. Kirn[16] , V.S. Kirsebom[29,p] , O. Kitouni[63] , S. Klaver[37] ,
N. Kleijne[33,s] , K. Klimaszewski[40] , M.R. Kmiec[40] , S. Koliiev[51] , L. Kolk[18] ,

A. Konoplyannikov[42], P. Kopciewicz[38,47], P. Koppenburg[36], M. Korolev[42],
I. Kostiuk[36], O. Kot[51], S. Kotriakhova, A. Kozachuk[42], P. Kravchenko[42],
L. Kravchuk[42], M. Kreps[55], P. Krokovny[42], W. Krupa[67], W. Krzemien[40],
O.K. Kshyvanskyi[51], J. Kubat[20], S. Kubis[77], M. Kucharczyk[39], V. Kudryavtsev[42],
E. Kulikova[42], A. Kupsc[79], B. K. Kutsenko[12], D. Lacarrere[47], A. Lai[30],
A. Lampis[30], D. Lancierini[54], C. Landesa Gomez[45], J.J. Lane[1], R. Lane[53],
C. Langenbruch[20], J. Langer[18], O. Lantwin[42], T. Latham[55], F. Lazzari[33,t],
C. Lazzeroni[52], R. Le Gac[12], R. Lefèvre[11], A. Leflat[42], S. Legotin[42],
M. Lehuraux[55], E. Lemos Cid[47], O. Leroy[12], T. Lesiak[39], B. Leverington[20],
A. Li[4], H. Li[70], K. Li[8], L. Li[61], P. Li[47], P.-R. Li[71], Q. Li[5,7], S. Li[8],
T. Li[5,d], T. Li[70], Y. Li[8], Y. Li[5], Z. Lian[4], X. Liang[67], S. Libralon[46], C. Lin[7],
T. Lin[56], R. Lindner[47], V. Lisovskyi[48], R. Litvinov[30,47], F. L. Liu[1], G. Liu[70],
K. Liu[71], S. Liu[5,7], Y. Liu[57], Y. Liu[71], Y. L. Liu[60], A. Lobo Salvia[44], A. Loi[30],
J. Lomba Castro[45], T. Long[54], J.H. Lopes[3], A. Lopez Huertas[44], S. López Soliño[45],
C. Lucarelli[25,m], D. Lucchesi[31,q], M. Lucio Martinez[76], V. Lukashenko[36,51],
Y. Luo[6], A. Lupato[31], E. Luppi[24,l], K. Lynch[21], X.-R. Lyu[7], G. M. Ma[4],
R. Ma[7], S. Maccolini[18], F. Machefert[13], F. Maciuc[41], B. Mack[67], I. Mackay[62], L.
M. Mackey[67], L.R. Madhan Mohan[54], M. M. Madurai[52], A. Maevskiy[42],
D. Magdalinski[36], D. Maisuzenko[42], M.W. Majewski[38], J.J. Malczewski[39], S. Malde[62],
L. Malentacca[47], A. Malinin[42], T. Maltsev[42], G. Manca[30,k], G. Mancinelli[12],
C. Mancuso[28,13,o], R. Manera Escalero[44], D. Manuzzi[23], D. Marangotto[28,o],
J.F. Marchand[10], R. Marchevski[48], U. Marconi[23], S. Mariani[47], C. Marin Benito[44],
J. Marks[20], A.M. Marshall[53], G. Martelli[32,r], G. Martellotti[34], L. Martinazzoli[47],
M. Martinelli[29,p], D. Martinez Santos[45], F. Martinez Vidal[46], A. Massafferri[2],
R. Matev[47], A. Mathad[47], V. Matiunin[42], C. Matteuzzi[67], K.R. Mattioli[14],
A. Mauri[60], E. Maurice[14], J. Mauricio[44], P. Mayencourt[48], M. Mazurek[40],
M. McCann[60], L. Mcconnell[21], T.H. McGrath[61], N.T. McHugh[58], A. McNab[61],
R. McNulty[21], B. Meadows[64], G. Meier[18], D. Melnychuk[40], F. M. Meng[4],
M. Merk[36,76], A. Merli[48], L. Meyer Garcia[65], D. Miao[5,7], H. Miao[7],
M. Mikhasenko[17,f], D.A. Milanes[73], A. Minotti[29,p], E. Minucci[67], T. Miralles[11],
B. Mitreska[18], D.S. Mitzel[18], A. Modak[56], A. Mödden[18], R.A. Mohammed[62],
R.D. Moise[16], S. Mokhnenko[42], T. Mombächer[47], M. Monk[55,1], S. Monteil[11],
A. Morcillo Gomez[45], G. Morello[26], M.J. Morello[33,s], M.P. Morgenthaler[20],
A.B. Morris[47], A.G. Morris[12], R. Mountain[67], H. Mu[4], Z. M. Mu[6],
E. Muhammad[55], F. Muheim[57], M. Mulder[75], K. Müller[49], F. Muñoz-Rojas[9],
R. Murta[60], P. Naik[59], T. Nakada[48], R. Nandakumar[56], T. Nanut[47], I. Nasteva[3],
M. Needham[57], N. Neri[28,o], S. Neubert[17], N. Neufeld[47], P. Neustroev[42],
J. Nicolini[18,13], D. Nicotra[76], E.M. Niel[48], N. Nikitin[42], P. Nogarolli[3], P. Nogga[17],
N.S. Nolte[63], C. Normand[53], J. Novoa Fernandez[45], G. Nowak[64], C. Nunez[80], H. N.
Nur[58], A. Oblakowska-Mucha[38], V. Obraztsov[42], T. Oeser[16], S. Okamura[24,l],
A. Okhotnikov[42], O. Okhrimenko[51], R. Oldeman[30,k], F. Oliva[57], M. Olocco[18],
C.J.G. Onderwater[76], R.H. O'Neil[57], J.M. Otalora Goicochea[3], P. Owen[49],
A. Oyanguren[46], O. Ozcelik[57], A. Padee[40], K.O. Padeken[17], B. Pagare[55],
P.R. Pais[20], T. Pajero[47], A. Palano[22], M. Palutan[26], G. Panshin[42], L. Paolucci[55],
A. Papanestis[56], M. Pappagallo[22,h], L.L. Pappalardo[24,l], C. Pappenheimer[64],
C. Parkes[61], B. Passalacqua[24], G. Passaleva[25], D. Passaro[33,s], A. Pastore[22],
M. Patel[60], J. Patoc[62], C. Patrignani[23,j], A. Paul[67], C.J. Pawley[76],
A. Pellegrino[36], J. Peng[5,7], M. Pepe Altarelli[26], S. Perazzini[23], D. Pereima[42], H.
Pereira Da Costa[66], A. Pereiro Castro[45], P. Perret[11], A. Perro[47], K. Petridis[53],
A. Petrolini[27,n], J. P. Pfaller[64], H. Pham[67], L. Pica[33], M. Piccini[32],

B. Pietrzyk[10], G. Pietrzyk[13], D. Pinci[34], F. Pisani[47], M. Pizzichemi[29,p],
V. Placinta[41], M. Plo Casasus[45], F. Polci[15,47], M. Poli Lener[26], A. Poluektov[12],
N. Polukhina[42], I. Polyakov[47], E. Polycarpo[3], G.J. Pomery[53], S. Ponce[47],
D. Popov[7], S. Poslavskii[42], K. Prasanth[57], C. Prouve[45], V. Pugatch[51],
G. Punzi[33,t], S. Qasim[49], Q. Q. Qian[6], W. Qian[7], N. Qin[4], S. Qu[4],
R. Quagliani[47], R.I. Rabadan Trejo[55], J.H. Rademacker[53], M. Rama[33], M.
Ramírez García[80], V. Ramos De Oliveira[68], M. Ramos Pernas[55], M.S. Rangel[3],
F. Ratnikov[42], G. Raven[37], M. Rebollo De Miguel[46], F. Redi[28,i], J. Reich[53],
F. Reiss[61], Z. Ren[7], P.K. Resmi[62], R. Ribatti[48], G. R. Ricart[14,81],
D. Riccardi[33,s], S. Ricciardi[56], K. Richardson[63], M. Richardson-Slipper[57],
K. Rinnert[59], P. Robbe[13], G. Robertson[58], E. Rodrigues[59],
E. Rodriguez Fernandez[45], J.A. Rodriguez Lopez[73], E. Rodriguez Rodriguez[45],
A. Rogovskiy[56], D.L. Rolf[47], P. Roloff[47], V. Romanovskiy[42], M. Romero Lamas[45],
A. Romero Vidal[45], G. Romolini[24], F. Ronchetti[48], T. Rong[6], M. Rotondo[26], S. R.
Roy[20], M.S. Rudolph[67], T. Ruf[47], M. Ruiz Diaz[20], R.A. Ruiz Fernandez[45],
J. Ruiz Vidal[79,aa], A. Ryzhikov[42], J. Ryzka[38], J. J. Saavedra-Arias[9],
J.J. Saborido Silva[45], R. Sadek[14], N. Sagidova[42], D. Sahoo[74], N. Sahoo[52],
B. Saitta[30,k], M. Salomoni[29,p,47], C. Sanchez Gras[36], I. Sanderswood[46],
R. Santacesaria[34], C. Santamarina Rios[45], M. Santimaria[26,47], L. Santoro [2],
E. Santovetti[35], A. Saputi[24,47], D. Saranin[42], A. S. Sarnatskiy[75], G. Sarpis[57],
M. Sarpis[61], C. Satriano[34,u], A. Satta[35], M. Saur[6], D. Savrina[42], H. Sazak[16],
L.G. Scantlebury Smead[62], A. Scarabotto[18], S. Schael[16], S. Scherl[59], M. Schiller[58],
H. Schindler[47], M. Schmelling[19], B. Schmidt[47], S. Schmitt[16], H. Schmitz[17],
O. Schneider[48], A. Schopper[47], N. Schulte[18], S. Schulte[48], M.H. Schune[13],
R. Schwemmer[47], G. Schwering[16], B. Sciascia[26], A. Sciuccati[47], S. Sellam[45],
A. Semennikov[42], T. Senger[49], M. Senghi Soares[37], A. Sergi[27], N. Serra[49],
L. Sestini[31], A. Seuthe[18], Y. Shang[6], D.M. Shangase[80], M. Shapkin[42], R. S.
Sharma[67], I. Shchemerov[42], L. Shchutska[48], T. Shears[59], L. Shekhtman[42],
Z. Shen[6], S. Sheng[5,7], V. Shevchenko[42], B. Shi[7], Q. Shi[7], Y. Shimizu[13],
E. Shmanin[42], R. Shorkin[42], J.D. Shupperd[67], R. Silva Coutinho[67], G. Simi[31,q],
S. Simone[22,h], N. Skidmore[55], T. Skwarnicki[67], M.W. Slater[52], J.C. Smallwood[62],
E. Smith[63], K. Smith[66], M. Smith[60], A. Snoch[36], L. Soares Lavra[57],
M.D. Sokoloff[64], F.J.P. Soler[58], A. Solomin[42,53], A. Solovev[42], I. Solovyev[42],
R. Song[1], Y. Song[48], Y. Song[4], Y. S. Song[6], F.L. Souza De Almeida[67],
B. Souza De Paula[3], E. Spadaro Norella[28,o], E. Spedicato[23], J.G. Speer[18],
E. Spiridenkov[42], P. Spradlin[58], V. Sriskaran[47], F. Stagni[47], M. Stahl[47], S. Stahl[47],
S. Stanislaus[62], E.N. Stein[47], O. Steinkamp[49], O. Stenyakin[42], H. Stevens[18],
D. Strekalina[42], Y. Su[7], F. Suljik[62], J. Sun[30], L. Sun[72], Y. Sun[65], D. S.
Sundfeld Lima[2], W. Sutcliffe[49], P.N. Swallow[52], F. Swystun[54], A. Szabelski[40],
T. Szumlak[38], Y. Tan[4], M.D. Tat[62], A. Terentev[42], F. Terzuoli[33,w,47],
F. Teubert[47], E. Thomas[47], D.J.D. Thompson[52], H. Tilquin[60], V. Tisserand[11],
S. T'Jampens[10], M. Tobin[5,47], L. Tomassetti[24,l], G. Tonani[28,o,47], X. Tong[6],
D. Torres Machado[2], L. Toscano[18], D.Y. Tou[4], C. Trippl[43], G. Tuci[20],
N. Tuning[36], L.H. Uecker[20], A. Ukleja[38], D.J. Unverzagt[20], E. Ursov[42],
A. Usachov[37], A. Ustyuzhanin[42], U. Uwer[20], V. Vagnoni[23], G. Valenti[23],
N. Valls Canudas[47], H. Van Hecke[66], E. van Herwijnen[60], C.B. Van Hulse[45,y],
R. Van Laak[48], M. van Veghel[36], G. Vasquez[49], R. Vazquez Gomez[44],
P. Vazquez Regueiro[45], C. Vázquez Sierra[45], S. Vecchi[24], J.J. Velthuis[53],
M. Veltri[25,x], A. Venkateswaran[48], M. Vesterinen[55], M. Vieites Diaz[47],
X. Vilasis-Cardona[43], E. Vilella Figueras[59], A. Villa[23], P. Vincent[15], F.C. Volle[52],

D. vom Bruch[12], N. Voropaev[42], K. Vos[76], G. Vouters[10,47], C. Vrahas[57],
J. Wagner[18], J. Walsh[33], E.J. Walton[1,55], G. Wan[6], C. Wang[20], G. Wang[8],
J. Wang[6], J. Wang[5], J. Wang[4], J. Wang[72], M. Wang[28], N. W. Wang[7],
R. Wang[53], X. Wang[8], X. Wang[70], X. W. Wang[60], Y. Wang[6], Z. Wang[13],
Z. Wang[4], Z. Wang[28], J.A. Ward[55,1], M. Waterlaat[47], N.K. Watson[52],
D. Websdale[60], Y. Wei[6], J. Wendel[78], B.D.C. Westhenry[53], D.J. White[61],
M. Whitehead[58], E. Whiter[52], A.R. Wiederhold[55], D. Wiedner[18], G. Wilkinson[62],
M.K. Wilkinson[64], M. Williams[63], M.R.J. Williams[57], R. Williams[54],
F.F. Wilson[56], W. Wislicki[40], M. Witek[39], L. Witola[20], C.P. Wong[66],
G. Wormser[13], S.A. Wotton[54], H. Wu[67], J. Wu[8], Y. Wu[6], K. Wyllie[47], S. Xian[70],
Z. Xiang[5], Y. Xie[8], A. Xu[33], J. Xu[7], L. Xu[4], L. Xu[4], M. Xu[55], Z. Xu[11],
Z. Xu[7], Z. Xu[5], D. Yang[4], K. Yang[60], S. Yang[7], X. Yang[6], Y. Yang[27,n],
Z. Yang[6], Z. Yang[65], V. Yeroshenko[13], H. Yeung[61], H. Yin[8], C. Y. Yu[6],
J. Yu[69], X. Yuan[5], E. Zaffaroni[48], M. Zavertyaev[19], M. Zdybal[39], C. Zeng[5,7],
M. Zeng[4], C. Zhang[6], D. Zhang[8], J. Zhang[7], L. Zhang[4], S. Zhang[69],
S. Zhang[6], Y. Zhang[6], Y. Z. Zhang[4], Y. Zhao[20], A. Zharkova[42], A. Zhelezov[20],
S. Z. Zheng[6], X. Z. Zheng[4], Y. Zheng[7], T. Zhou[6], X. Zhou[8], Y. Zhou[7],
V. Zhovkovska[55], L. Z. Zhu[7], X. Zhu[4], X. Zhu[8], V. Zhukov[16], J. Zhuo[46],
Q. Zou[5,7], D. Zuliani[31,q], G. Zunica[48].

[1] School of Physics and Astronomy, Monash University, Melbourne, Australia
[2] Centro Brasileiro de Pesquisas Físicas (CBPF), Rio de Janeiro, Brazil
[3] Universidade Federal do Rio de Janeiro (UFRJ), Rio de Janeiro, Brazil
[4] Center for High Energy Physics, Tsinghua University, Beijing, China
[5] Institute Of High Energy Physics (IHEP), Beijing, China
[6] School of Physics State Key Laboratory of Nuclear Physics and Technology, Peking University, Beijing, China
[7] University of Chinese Academy of Sciences, Beijing, China
[8] Institute of Particle Physics, Central China Normal University, Wuhan, Hubei, China
[9] Consejo Nacional de Rectores (CONARE), San Jose, Costa Rica
[10] Université Savoie Mont Blanc, CNRS, IN2P3-LAPP, Annecy, France
[11] Université Clermont Auvergne, CNRS/IN2P3, LPC, Clermont-Ferrand, France
[12] Aix Marseille Univ, CNRS/IN2P3, CPPM, Marseille, France
[13] Université Paris-Saclay, CNRS/IN2P3, IJCLab, Orsay, France
[14] Laboratoire Leprince-Ringuet, CNRS/IN2P3, Ecole Polytechnique, Institut Polytechnique de Paris, Palaiseau, France
[15] LPNHE, Sorbonne Université, Paris Diderot Sorbonne Paris Cité, CNRS/IN2P3, Paris, France
[16] I. Physikalisches Institut, RWTH Aachen University, Aachen, Germany
[17] Universität Bonn - Helmholtz-Institut für Strahlen und Kernphysik, Bonn, Germany
[18] Fakultät Physik, Technische Universität Dortmund, Dortmund, Germany
[19] Max-Planck-Institut für Kernphysik (MPIK), Heidelberg, Germany
[20] Physikalisches Institut, Ruprecht-Karls-Universität Heidelberg, Heidelberg, Germany
[21] School of Physics, University College Dublin, Dublin, Ireland
[22] INFN Sezione di Bari, Bari, Italy
[23] INFN Sezione di Bologna, Bologna, Italy
[24] INFN Sezione di Ferrara, Ferrara, Italy
[25] INFN Sezione di Firenze, Firenze, Italy
[26] INFN Laboratori Nazionali di Frascati, Frascati, Italy
[27] INFN Sezione di Genova, Genova, Italy
[28] INFN Sezione di Milano, Milano, Italy
[29] INFN Sezione di Milano-Bicocca, Milano, Italy
[30] INFN Sezione di Cagliari, Monserrato, Italy
[31] INFN Sezione di Padova, Padova, Italy
[32] INFN Sezione di Perugia, Perugia, Italy

[33] INFN Sezione di Pisa, Pisa, Italy
[34] INFN Sezione di Roma La Sapienza, Roma, Italy
[35] INFN Sezione di Roma Tor Vergata, Roma, Italy
[36] Nikhef National Institute for Subatomic Physics, Amsterdam, Netherlands
[37] Nikhef National Institute for Subatomic Physics and VU University Amsterdam, Amsterdam, Netherlands
[38] AGH - University of Krakow, Faculty of Physics and Applied Computer Science, Kraków, Poland
[39] Henryk Niewodniczanski Institute of Nuclear Physics Polish Academy of Sciences, Kraków, Poland
[40] National Center for Nuclear Research (NCBJ), Warsaw, Poland
[41] Horia Hulubei National Institute of Physics and Nuclear Engineering, Bucharest-Magurele, Romania
[42] Affiliated with an institute covered by a cooperation agreement with CERN
[43] DS4DS, La Salle, Universitat Ramon Llull, Barcelona, Spain
[44] ICCUB, Universitat de Barcelona, Barcelona, Spain
[45] Instituto Galego de Física de Altas Enerxías (IGFAE), Universidade de Santiago de Compostela, Santiago de Compostela, Spain
[46] Instituto de Fisica Corpuscular, Centro Mixto Universidad de Valencia - CSIC, Valencia, Spain
[47] European Organization for Nuclear Research (CERN), Geneva, Switzerland
[48] Institute of Physics, Ecole Polytechnique Fédérale de Lausanne (EPFL), Lausanne, Switzerland
[49] Physik-Institut, Universität Zürich, Zürich, Switzerland
[50] NSC Kharkiv Institute of Physics and Technology (NSC KIPT), Kharkiv, Ukraine
[51] Institute for Nuclear Research of the National Academy of Sciences (KINR), Kyiv, Ukraine
[52] University of Birmingham, Birmingham, United Kingdom
[53] H.H. Wills Physics Laboratory, University of Bristol, Bristol, United Kingdom
[54] Cavendish Laboratory, University of Cambridge, Cambridge, United Kingdom
[55] Department of Physics, University of Warwick, Coventry, United Kingdom
[56] STFC Rutherford Appleton Laboratory, Didcot, United Kingdom
[57] School of Physics and Astronomy, University of Edinburgh, Edinburgh, United Kingdom
[58] School of Physics and Astronomy, University of Glasgow, Glasgow, United Kingdom
[59] Oliver Lodge Laboratory, University of Liverpool, Liverpool, United Kingdom
[60] Imperial College London, London, United Kingdom
[61] Department of Physics and Astronomy, University of Manchester, Manchester, United Kingdom
[62] Department of Physics, University of Oxford, Oxford, United Kingdom
[63] Massachusetts Institute of Technology, Cambridge, MA, United States
[64] University of Cincinnati, Cincinnati, OH, United States
[65] University of Maryland, College Park, MD, United States
[66] Los Alamos National Laboratory (LANL), Los Alamos, NM, United States
[67] Syracuse University, Syracuse, NY, United States
[68] Pontifícia Universidade Católica do Rio de Janeiro (PUC-Rio), Rio de Janeiro, Brazil, associated to [3]
[69] School of Physics and Electronics, Hunan University, Changsha City, China, associated to [8]
[70] Guangdong Provincial Key Laboratory of Nuclear Science, Guangdong-Hong Kong Joint Laboratory of Quantum Matter, Institute of Quantum Matter, South China Normal University, Guangzhou, China, associated to [4]
[71] Lanzhou University, Lanzhou, China, associated to [5]
[72] School of Physics and Technology, Wuhan University, Wuhan, China, associated to [4]
[73] Departamento de Fisica , Universidad Nacional de Colombia, Bogota, Colombia, associated to [15]
[74] Eotvos Lorand University, Budapest, Hungary, associated to [47]
[75] Van Swinderen Institute, University of Groningen, Groningen, Netherlands, associated to [36]
[76] Universiteit Maastricht, Maastricht, Netherlands, associated to [36]
[77] Tadeusz Kosciuszko Cracow University of Technology, Cracow, Poland, associated to [39]
[78] Universidade da Coruña, A Coruna, Spain, associated to [43]
[79] Department of Physics and Astronomy, Uppsala University, Uppsala, Sweden, associated to [58]
[80] University of Michigan, Ann Arbor, MI, United States, associated to [67]
[81] Departement de Physique Nucleaire (SPhN), Gif-Sur-Yvette, France

[a] Universidade de Brasília, Brasília, Brazil
[b] Centro Federal de Educacão Tecnológica Celso Suckow da Fonseca, Rio De Janeiro, Brazil
[c] Hangzhou Institute for Advanced Study, UCAS, Hangzhou, China

[d]School of Physics and Electronics, Henan University , Kaifeng, China
[e]LIP6, Sorbonne Université, Paris, France
[f]Excellence Cluster ORIGINS, Munich, Germany
[g]Universidad Nacional Autónoma de Honduras, Tegucigalpa, Honduras
[h]Università di Bari, Bari, Italy
[i]Universita degli studi di Bergamo, Bergamo, Italy
[j]Università di Bologna, Bologna, Italy
[k]Università di Cagliari, Cagliari, Italy
[l]Università di Ferrara, Ferrara, Italy
[m]Università di Firenze, Firenze, Italy
[n]Università di Genova, Genova, Italy
[o]Università degli Studi di Milano, Milano, Italy
[p]Università degli Studi di Milano-Bicocca, Milano, Italy
[q]Università di Padova, Padova, Italy
[r]Università di Perugia, Perugia, Italy
[s]Scuola Normale Superiore, Pisa, Italy
[t]Università di Pisa, Pisa, Italy
[u]Università della Basilicata, Potenza, Italy
[v]Università di Roma Tor Vergata, Roma, Italy
[w]Università di Siena, Siena, Italy
[x]Università di Urbino, Urbino, Italy
[y]Universidad de Alcalá, Alcalá de Henares , Spain
[z]Facultad de Ciencias Fisicas, Madrid, Spain
[aa]Department of Physics/Division of Particle Physics, Lund, Sweden

[†]Deceased